UNIVERSITY OF LONDON

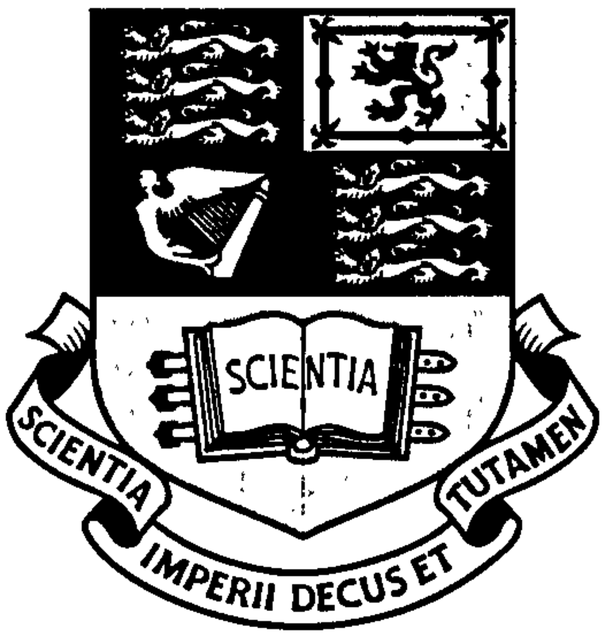

Imperial College London

Physics Department
Quantum Optics and Laser Science Group

Atomic relaxation processes near conducting and superconducting surfaces

Rachele Fermani

March 2008

Thesis submitted in partial fulfilment of the requirements for the degree of
Doctor of Philosophy of the University of London

Abstract

The aim of this thesis is to investigate the interaction of neutral atoms with conducting and superconducting surfaces. Experimental advances in the magnetic confinement of ultracold atoms have shown that they can act as a powerful tool in a wide range of phenomena such as electric and magnetic field imaging and matter wave interferometry. Coherent manipulation of atoms and ever smaller magnetic traps are essential elements in the implementation of integrated quantum devices for fundamental research, quantum information processing and precision measurements.

This thesis considers main influences on atoms placed within three different environments which are useful in achieving miniaturization and efficient control in atomic magnetic traps: carbon nanotubes, dielectric surfaces and superconducting thin films. The possibility of holding atoms near the outside of a carbon nanotubes will be addressed. In order to give a qualitative analysis of the atom-nanotube interaction, thermally induced spin-flips and the Casimir-Polder potential have been considered. The comparison between these two effects is presented in this thesis. It indicates that the Casimir-Polder force is the dominant loss mechanism and an estimation of the minimum trapping distance is given based on its effect.

Secondly, a first-principles derivation of spatial atomic-sublevel decoherence near dielectric and metallic surfaces will be presented. The rate obtained for the decay of spatial coherence has dual implications. On one hand, it can be considered as a measure of the coherence length of the fluctuations of the electromagnetic field arising from a given substrate. On the other hand, it turns out to be relevant for quantum information encoding in double well potentials. Finally, the known spin-flip transition rate will be linked to the flux noise spectrum in superconducting thin films showing the feasibility of using cold atomic clouds in the investigation of vortex dynamics.

I declare that the work contained within this thesis is my own work unless stated otherwise

Signature: Rachelle Fonnereau Date: 29/03/08

Thesis Publications

1. R. Fermani, S. Scheel and P. L. Knight, *Spatial decoherence near metallic surfaces*, Phys. Rev. A **73**, 032902 (2006).

2. S. Scheel, R. Fermani, and E. A. Hinds, *Feasibility of studying vortex noise in two-dimensional superconductors with cold atoms*, Phys.Rev.A **75**, 064901 (2007).

3. R. Fermani, S. Scheel and P. L. Knight, *Trapping cold atoms near carbon nanotubes: Thermal spin flips and Casimir-Polder potential*, Phys.Rev.A **75**, 062905 (2007).

Conference proceedings

4. S. Scheel, R. Fermani, P. K. Rekdal and E. A. Hinds, *Atomic spin relaxation and spatial decoherence near metallic and superconducting surfaces*, J. Phys.: Conf. Ser. **36** 188-193, (2006).

5. R. Fermani, S. Scheel and P. L. Knight, *Atomic Spin Flip Loss and Spatial Decoherence*, Acta Phys. Hung. B **26**, 55-62 (2006).

Acknowledgements

An enormously huge thanks must go to Stefan Scheel who has supervised me throughout this project. I am grateful to him for feeding me with exciting physics, for guiding me through the meanderings of a researcher's life and for being understanding whenever I was popping into his office seeking for help. Many thanks to Peter Knight, for bringing me to Imperial College and overseeing me during the Conquest programme which gave me the opportunity to interact with many very talented people. I would like to acknowledge all the members of the Quantum Optics group at the University of Camerino for their kind support, particularly Stefano Mancini for his constant presence and his patience in reminding me to believe in myself and in my abilities.

Many thanks to Alex, Doug, Philip, Stefan B. and Stefan S. for taking the time to read this thesis and offering their precious feedback, as well as suggesting improvements in the English.

My gratitude goes to all the people I have met at Imperial that at some stage made my life here easier and more pleasant. Thanks to Jeremy and Jae for being such close friends as soon as I landed in London. Thanks to Nick and Philip for being awesome company during all the evenings spent at the office, and to Luke for being an endless source of coffee. Thanks also to all the wild and great people I have had the pleasure to share 6M09 with, it's not the quietest office I have been in, but definitely the friendliest. Thanks to Doug and Oli who have been extremely supportive during the last month. I need to thank the two of them and Adele for

many relaxing coffee breaks and for allowing me to spy into Stefan's office.

There are also a few other people who I should thank. Jane, for her constant presence via email and for making me look forward the end of the thesis promising girlish movies and lots of photos. Alvar, for taking great care of me during last summer by listening to all the panicking at the beginning of this thesis; and making sure that I had a nice dinner at the end of a long day.

Finally, I am extremely grateful to all my family for being always supportive during these three years and understanding for my prolonged disappearances.

Table of Contents

List of Figures

Preface

The interaction between an atom and a dielectric or conducting surface is of fundamental importance in the investigation of a wide range of physical phenomena, such as in accurate measurement of inertial forces [1,2], electromagnetic field imaging [3–6], sensing near-field noise in the proximity of metallic and dielectric surfaces [7–10] and probing the Casimir-Polder force [11]. The atom is typically at a distance from the substrate, usually >1 nm, such that it does not resolve the details of the atomic structure of the surface. Atom-surface interaction is an unvoidable feature whenever an atom is held close to a macroscopic body and the precise understanding of their coupling is an essential concern.

The spontaneous decay of an excited atom is one of the most studied examples of quantum processes due to ground-state fluctuations in the electromagnetic vacuum [12]. However, the vacuum field and its statistical properties are modified by the presence of dielectric bodies and this leads to a modification of the spontaneous emission rate and of the Lamb shift. In particular, the latter is associated with the appearance of an attractive dispersion force of the van der Waals (Casimir-Polder) type due to the spatial variation of the shift [10–19]. Another fundamental issue is represented by thermal fluctuations of the magnetic field near the surface. The coupling between the spin of an atom and a thermally fluctuating field results in the surface-induced modification of the atomic spin-flip lifetime [8–10,20,21]. The present thesis contributes to the latter issue by studying atom-surface interactions for atoms magnetically confined in microscopic traps such as atom chips [22–26],

posing particular attention to trapping lifetimes and relaxation processes.

Microscopic traps for neutral atoms using nano-structures carrying currents are called atom chips in analogy with computer chips. While in conventional microchips, electrons move inside wires embedded in a solid state object, in atom chips atoms stay a few micrometers above the surface of the wires. Atom chips represent a powerful tool in the robust confinement of ultracold atoms, providing flexible trapping geometries [22–26] and efficient quantum-state manipulation [27–36]. This technology is highly attractive for the implementation of quantum information processing or the construction of a matter-wave interferometer, as it permits the accurate control over the internal and external atomic degrees of freedom. A way to obtain coherent control over atoms is to realize confining potentials and trapping structures which are comparable in size with the de Broglie wavelength of the atoms [37–44]. In atom chips, a microstructured surface is used to produce electromagnetic fields patterned on the micron and submicron scale, which would not be possible in free space. This is what makes them the ideal environment to study atom-surface interactions.

An atom held close to a dielectric or conducting body feels an attractive van der Waals interaction which can be overcome by creating a repulsive potential. However, the chip surface is at room temperature and can be regarded as a macroscopic hot object with respect to ultracold atoms. Thermal magnetic noise may still cause the atom to be lost or tunnel through the repulsive potential and get absorbed at the surface. Part of the magnetic noise has a technical origin: fluctuations in the electric currents generating the trapping fields result in a deformation of the confining potential. While technical noise can be reduced experimentally, thermal fluctuating electromagnetic fields are more difficult to control.

Low-frequency magnetic noise has recently emerged as a limiting factor in the lifetime of atoms magnetically confined in microtraps [7–10, 45–52]. Thermally-induced current fluctuations cause the electromagnetic field near the substrate to fluctuate with a broad noise spectrum which is rather flat in the low-frequency

range [48]. These fluctuating fields can be strong enough to drive spin-flip transitions in magnetically trapped atoms, which then lead to atomic losses. Longer lifetimes would be achievable by holding the atoms further away from the surface but the magnetic trapping potential would be much more shallow making atomic manipulation more difficult. As a consequence, the realization of coherent operations on the atoms often requires a compromise between the achievement of long trapping lifetimes and the trend towards miniaturization. The limitations imposed by atom-surface interactions are often defined in terms of a minimum distance of the atom from the surface or a maximum time scale for coherent operations. This is reflected in constraints for the implementation of quantum information processing (QIP) or matter-wave interferometry.

The encoding of quantum information in QIP with ultracold atoms is typically realized by performing coherent operations on quantum superpositions of the atomic states [27–36]. A robust encoding and efficient manipulation require tight confining potentials which are achievable by reducing the trap dimensions and by holding atoms in close proximity of the trap surface. However, below a certain separation the atom-surface coupling is strong enough such that the Zeeman interaction with the near-field magnetic noise affects the internal state of the atoms and the trapping potential. The encoding of quantum information into internal (hyperfine ground states) and external degrees of freedom (vibrational modes), is then subjected to errors and decoherence phenomena [28,31,32,34,36,53].

Atom interferometry is well known for its successful applications when precision sensing of inertial forces is required [54,55] and different techniques have been used to split and manipulate Bose Einstein condensates (BECs) on microtraps. The evolution of a system in a double-well potential has been widely studied from both the experimental and theoretical point of view. Relaxation phenomena represent a problem in the context of atom interferometry. The progress in trapping and manipulating neutral atoms with microtraps has led to recent experimental realizations of on-chip matter-wave interferometry but there is serious concern regarding

phase diffusion and spatial asymmetry in the potential which may originate from fluctuating electromagnetic fields on the chip surface [56–64].

As a further example of relevance of the issues addressed in this thesis, magnetic field sensing [3–6] may be considered. Conventional methods for magnetic field measurement are able to provide either high field sensitivity at low spatial resolution, via superconducting quantum interference devices [65] and atomic magnetometers [3], or high resolution at low sensitivity, via magnetic-force microscopy [66]. Cold atomic clouds represent a valid alternative to standard methods, as magnetically trapped atoms act as sensitive probes of the electromagnetic field when held close to the chip structure. Trap equilibrium positions depend on the mean fields while transitions between internal states are proportional to the local spectral density of the field fluctuations. Accurate imaging of the atomic cloud's density profile allows the achievement of high spatial resolution together with high field sensitivity.

Extensive work has been carried out in the field of atom-surface interactions. The fundamental limits for coherent manipulation of neutral atoms in atom chips have been addressed, with particular attention to the noise originating from the chip surface [45–53, 67–70]. Henkel and co-workers have developed a description of magnetostatic field noise near metallic surfaces and computed noise spectra by adopting two different approaches. The first is based on a stochastic electrodynamics approach, where dissipation in the material is associated with random charge and current fluctuations [68, 70]. The radiation created by these fluctuations is then summed up incoherently, i.e. without taking care of how they are correlated to one another, which leads to the correct scaling laws of magnetic noise spectrum for atom chip geometry [47]. A second method uses the fluctuation-dissipation theorem to calculate the radiation from a single dipole source (Green function) [67] and provides a better agreement between theoretical predictions and experimental results [45, 51].

The Green function approach has been used by Scheel and co-workers to

develop a quantization scheme for the electromagnetic field in dielectric media [71–76]. The description provided for the thermally fluctuating near-field in the presence of dispersing and absorbing bodies proved useful to obtain a first-principle derivation of the spin-flip transition rate [49, 50]. The rate is expressed in terms of a Green tensor and in principle it can be applied to a dielectric body of any shape. The investigation presented throughout this thesis has been carried out within the framework of quantum electrodynamics (QED) in absorbing dielectric media following the method presented in [49].

Three physical systems are studied in depth, each one considers the interaction of a neutral atom with a different substrate. Initially, an atom held outside a carbon nanotube is taken into consideration. Carbon nanotubes [77–81] are graphene sheets rolled up into cylinders with diameters of a few nanometers. This system is particularly interesting due to the reduced dimensions of carbon nanotubes compared to standard wires. Furthermore, the small amount of dielectric matter constituting a carbon nanotube leads to a reduction of near field noise.

Secondly, an atom in a double-well potential above a planar dielectric substrate is studied. The atom is in a spatial superposition of two positions and the evolution of its state is investigated. A spatial decoherence rate is derived paying particular attention on physical length scales. The evolution of the macroscopic superposition state is interesting for its potential applications in quantum information processing in order to achieve robust manipulation of the atomic state. This topic is also relevant in matter-wave interferometry where coherent evolution of atomic wave packets in a double well is required to obtain an interference pattern.

Finally, the possibility of detecting vortices in thin superconducting films using cold atoms is investigated. Superconducting materials exhibit very small penetration depths and a zero-resistance behaviour which is particularly interesting when considering the near-field magnetic noise. A vanishing resistance implies that thermally-induced current fluctuations are highly reduced and this is expected to boost the atomic lifetime by several orders of magnitude [50, 82, 83]. However, ab-

sorption and dissipation phenomena also take place in superconductors. Magnetic noise is present in thin superconducting films in the form of vortex motion [84–88] and cold atoms may represent a valid alternative to standard measurements of vortex dynamics.

The thesis layout is the following. Chapter 1 reviews the magnetic trapping of neutral atoms in microtraps, presents the principle loss mechanisms and focusses on magnetic field noise. In Chapter 2, the quantization of the classical phenomenological Maxwell equations is introduced. In Chapter 3, the spin-flip lifetime of an atom trapped near the outside of a metallic nanotube is compared with the tunnelling lifetime deriving from the Casimir-Polder potential. In Chapter 4, the spatial decoherence of an atom in a superposition of two distinct positions is derived for a planar surface. In Chapter 5, the feasibility of detecting vortex dynamics in a two-dimensional superconductor with cold atoms is addressed. Conclusion and outlooks are summarised at the end of this thesis. Appendix A reports the calculation of axial conductivity and dielectric permittivity for a carbon nanotube while Appendix B reviews the Green tensor for planar multilayers.

1

Magnetic trapping

Significant progress has been made in the magnetic trapping of neutral atoms [22–26], and since 1985 the creation of confining magnetic fields with a combination of dipole and quadrupole magnets is a well-known technique [89–91]. Nowadays, trapping over microstructured solid-state surfaces is commonly adopted to manipulate atoms [37–44]. Magnetic mirrors, evanescent light fields and current carrying wires, are widely used because of the flexibility they provide in the realization of different trapping geometries. The ability to modify the confining magnetic fields by adjusting currents or by changing the strength of external control fields, makes magnetic traps a versatile tool. Promising areas of on-chip applications include modeling of quantum gases and disordered systems [92, 93], magnetic field sensing [4–6], atom interferometry [56–64] and quantum information processing [27, 29–31, 33–35].

Magnetic trapping is possible because an inhomogeneous magnetic field exerts forces on atoms with a non-zero magnetic dipole moment μ. For example, an atom placed in a magnetic field $\mathbf{B}(\mathbf{r})$ experiences the potential

$$V(\mathbf{r}) = -\mu \cdot \mathbf{B}(\mathbf{r}). \tag{1.1}$$

Depending on the orientation of the magnetic dipole moment $\boldsymbol{\mu} = g_F \mu_B \mathbf{F}$ relative to the direction of the magnetic field, where μ_B is the Bohr magneton, g_F is the Landé g- factor of the atomic hyperfine state and $\mathbf{F}$ is the total spin of the atom with m_F the magnetic quantum number, there are two cases:

- if the magnetic moment points in the direction opposite to the magnetic field ($g_F m_F < 0$, $V > 0$), the atom experiences a force towards the minimum of the field, therefore is a weak-field seeker;
- if the magnetic moment points in the same direction of the magnetic field ($g_F m_F > 0$, $V < 0$), the atom is attracted towards increasing fields and is said to be a strong-field seeker.

The magnetic moment $\boldsymbol{\mu}$ precesses about the direction of the magnetic field with the Larmor frequency

$$\omega_L = g_F \mu_B B/\hbar. \tag{1.2}$$

In most cases, in the frame of reference of the moving atom, the change in direction of the magnetic field is much slower than the Larmor precession such that the magnetic moment precesses around the local direction of the magnetic field and is said to follow adiabatically the magnetic field direction. Thus on average $\boldsymbol{\mu}$ is aligned with $\mathbf{B}(\mathbf{r})$ with its projection along the field direction taking values $g_F \mu_B m_F$. The potential in Eq. (1.1) is then equal to the modulus of $\boldsymbol{\mu}$ times the field magnitude $B(\mathbf{r}) = |\mathbf{B}(\mathbf{r})|$, and it does not vary with the field direction such that Eq. (1.1) can be written as

$$V(\mathbf{r}) = -\boldsymbol{\mu} \cdot \mathbf{B}(\mathbf{r}) = -g_F \mu_B m_F B(\mathbf{r}). \tag{1.3}$$

Static magnetic field configurations can only trap weak-field seeking atoms in local magnetic field minima. Earnshaw's theorem states that a collection of point charges cannot be maintained in a stable stationary equilibrium configuration solely by the electromagnetic interaction of the charges. As a consequence, Maxwell

equations do not allow local maxima of the field potential in free space, only saddle points [94, 95]. The magnetic confinement is stable only if the adiabaticity condition is satisfied. Violation of this condition results in a large probability of non-adiabatic or Majorana transitions which change the orientation of the magnetic moment to a state that may not be confined in the trap, i.e. the atom becomes a strong-field seeker and is expelled from the trap [96–98].

This Chapter reviews the magnetic confinement of neutral atoms in microtraps. Magnetic trapping is performed by creating a line of zero magnetic field where neutral atoms can be kept which is possible by using the magnetic field due to a current-carrying wire and a bias homogeneous field, the combination of the two gives a magnetic potential where neutral atom can be trapped. This is the building block of magnetic microtrap, which is often referred to as atom chip, and can be used to construct more complex confining potentials. The tendency is to reduce trap dimensions as much as possible so as to achieve stronger trapping potentials and longer lifetimes. However, an atom in the close proximity of a 'hot' substrate experiences thermally-induced magnetic noise that imposes limitations on minimum distances from the surface and maximum lifetimes.

The Chapter is organized as follows. In Section 1.1 the basic concepts of magnetic trapping in atom chips are presented. Section 1.2 deals with the principal loss mechanisms such as heating and technical noise. Section 1.3 focuses on the atomic interaction with near field noise and the fluctuating environment produced by the materials constituting the chip.

1.1 Simple atom guides

A current-carrying wire is the atom chip 'building block', as introduced by Frisch and Segré in 1933 [99]. They suggested trapping atoms in a circular magnetic field produced by a straight current-carrying wire and a homogeneous magnetic field perpendicular to the wire. The combined field has a minimum located where the two fields have the same magnitude but opposite directions, which means that

there is a line of zero magnetic field parallel to the wire. A current I directed along the z direction produces a radial magnetic B field with modulus

$$|\mathbf{B}| = \frac{\mu_0 I}{2\pi r}, \tag{1.4}$$

at a distance r from the wire, and a constant field $\mathbf{B}_b$ perpendicular to the wire cancels out the circular magnetic field $\mathbf{B}$ at a distance y_0

$$y_0 = \frac{\mu_0 I}{2\pi B_b}. \tag{1.5}$$

The total field is now given by the sum of the two magnetic fields $\mathbf{B} + \mathbf{B}_b = \mathbf{B}_{\mathrm{TOT}}$

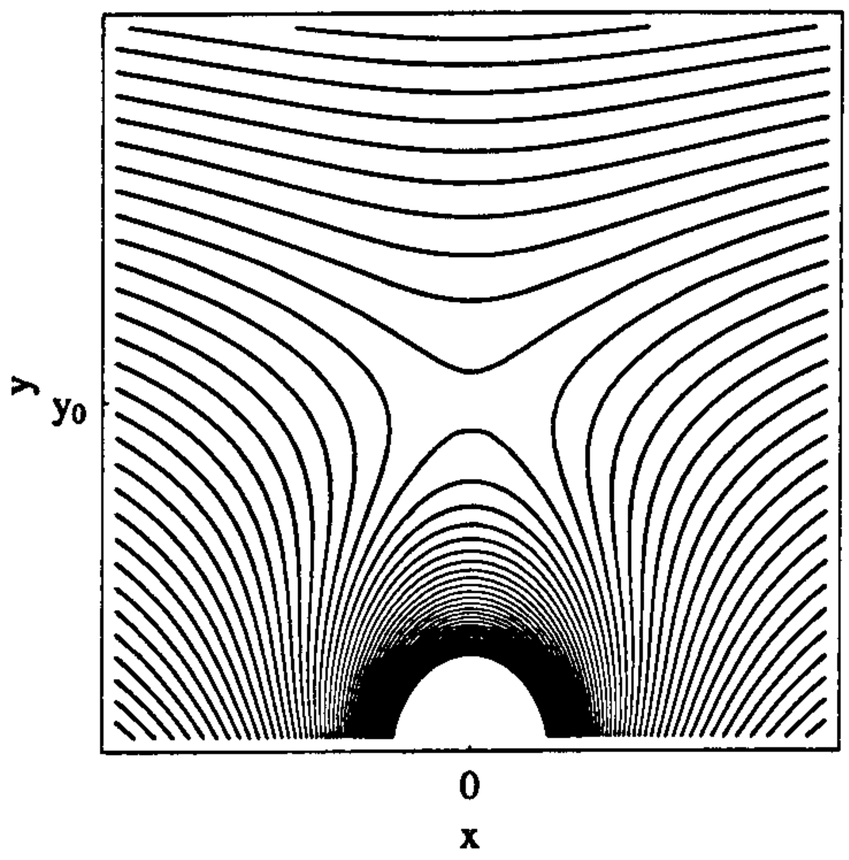

Figure 1.1: Representation of the magnetic field lines generated by current flowing in a wire extending along the z direction and an external bias field perpendicular to the wire direction.

the field lines of which are shown in Fig. 1.1. In Cartesian coordinates one can write $r^2 = x^2 + y^2$ and the y-component reads

$$|\mathbf{B}_{\mathrm{TOT}}(x=0,y)| = \frac{\mu_0 I}{2\pi}\sqrt{\frac{1}{y_0^2} + \frac{1}{y^2} - \frac{2}{y_0|y|}}. \tag{1.6}$$

A weak-field seeking atom can be confined at a distance y_0 where the magnetic field is zero, as shown in Fig. 1.2. That point is taken as the trap center, ($x = 0$, $y =$

y_0), at which the first derivative of the magnetic field intensity is independent of position

$$\partial_r |\mathbf{B}_{\mathrm{TOT}}|\Big|_{y=y_0} = -\frac{\mu_0 I}{2\pi r^2}\Big|_{y=y_0} = -\frac{\mu_0 I}{2\pi y_0^2} = -\frac{2\pi B_b^2}{\mu_0 I} \equiv -b', \tag{1.7}$$

and in Cartesian coordinates reads

$$\frac{dB_x}{dx} = -\frac{dB_y}{dy} = b'. \tag{1.8}$$

Therefore, the field near the minimum can be approximated by a linear function of its gradient

$$\mathbf{B}_{\mathrm{TOT}} = \mathbf{B} + \mathbf{B}_b = b'(x\mathbf{e}_x - y\mathbf{e}_y), \tag{1.9}$$

$$|\mathbf{B}_{\mathrm{TOT}}| \backsimeq b'(x^2 + y^2)^{1/2} = b' r_c, \tag{1.10}$$

where r_c is now the distance from the centre of the trap, such as in the case of a quadrupole trap.

An atom positioned at the centre of the trap experiences a field that is almost zero and the adiabaticity condition is violated in regions of very small magnetic field. In these regions, Majorana transitions changing the orientation of the atomic magnetic moment to non-trapped states can easily take place [96–98]. To prevent these transitions, an additional magnetic field $\mathbf{B}_0$ oriented parallel to the wire is superimposed and the y-component of the modulus of the total magnetic field becomes

$$|\mathbf{B}_{\mathrm{TOT}}(x=0,y)| = \frac{\mu_0 I}{2\pi}\sqrt{\frac{1}{y_0^2} + \frac{1}{y^2} - \frac{2}{y_0|y|} + |\mathbf{B}_0|^2}, \tag{1.11}$$

as shown in Fig. 1.2(b). The total magnetic field is then given by

$$\mathbf{B}_{\mathrm{TOT}} = \mathbf{B} + \mathbf{B}_b + \mathbf{B}_0, \tag{1.12}$$

and for sufficiently small r_c such that $b'r_c << |\mathbf{B}_0|$ the field modulus can be

approximated as

$$|\mathbf{B}_{\mathrm{TOT}}| = \left[|\mathbf{B}_0|^2 + (b'r_c)^2\right]^{1/2} \simeq |\mathbf{B}_0| + \frac{b'^2 r_c^2}{2|\mathbf{B}_0|}. \tag{1.13}$$

The substitution of Eq. (1.13) into the interaction potential of Eq. (1.3), allows

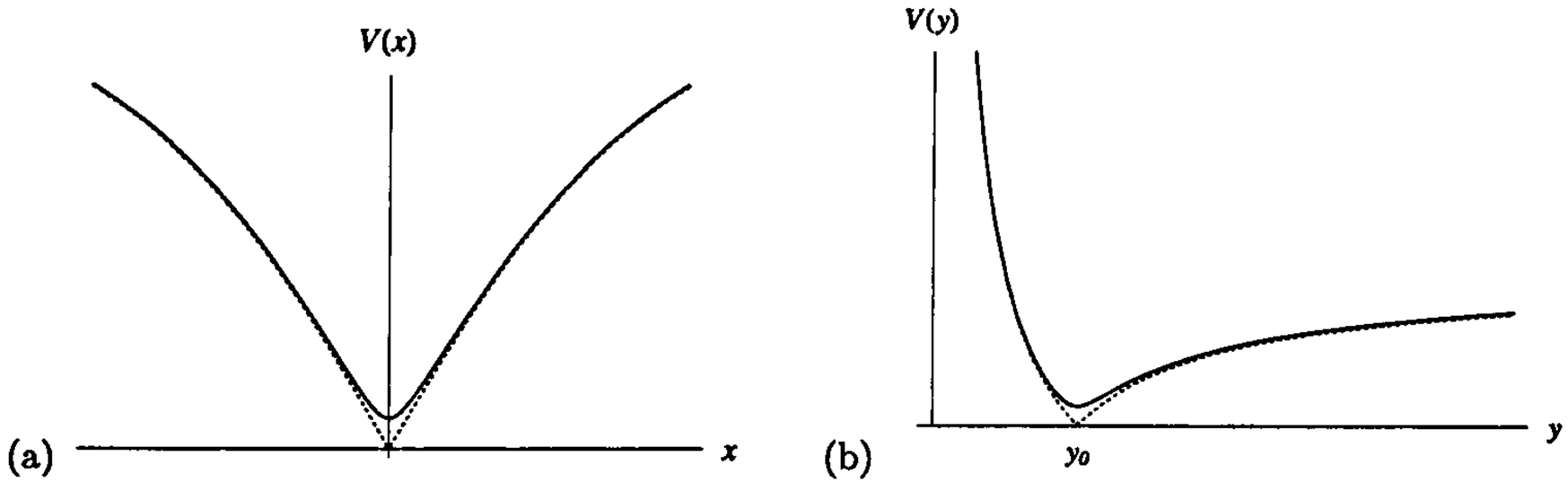

Figure 1.2: Cross section of the magnetic potential of Eq. (1.3) along the x-axis (a) and y-axis (b). The cusp at the bottom of the potential leads to non-adiabatic transitions of the trapped atoms (dashed line). A bias field along the z-direction rounds the bottom of the trap to give a harmonic potential near the axis.

Eq. (1.3) to be re-written as a harmonic potential

$$\begin{aligned} V(r) &= -g_F \mu_B m_F \left(|\mathbf{B}_0| + \frac{b'^2 r_c^2}{2|\mathbf{B}_0|}\right) \\ &= V_0 + \frac{1}{2} M \omega_r^2 r_c^2, \end{aligned} \tag{1.14}$$

where the oscillation frequency is given by

$$\omega_r = \sqrt{\frac{g_F \mu_B m_F}{M|\mathbf{B}_0|}} \frac{\mu_0 I}{2\pi y_0^2}. \tag{1.15}$$

The confining potentials produced by free-standing structures, i.e. current-carrying wires, are in general pretty shallow and deform easily due to external forces leading to a weak trapping of the atoms. Wires mounted on a surface are more robust and allow for tighter confinement of atoms in the traps. Two such examples are illustrated in Fig. 1.3 and Fig. 1.4. The quantum control over the motion of ultracold atoms that would permits a faster and more efficient creation

of BECs can be achieved with miniaturization. In fact, a full quantum control of an atom of mass m and energy E, requires the confining potential to vary on a length scale $\lambda \sim h/(mE)^{1/2}$ which is usually of the order of 1 μm and that is possible if the trapping distances are small enough, i.e. $d \leq \lambda$. The miniaturization of electric conductors on a substrate is possible by current nanofabrication technology which allows to place wires on a surface with great accuracy. Nanofabrication permits the realization of confining structures with high resolution and as a consequence the magnetic potential can be tailored to trap atoms individually. This is very important in order to localize atoms in steep traps and to reduce the distances between individual trapping sites.

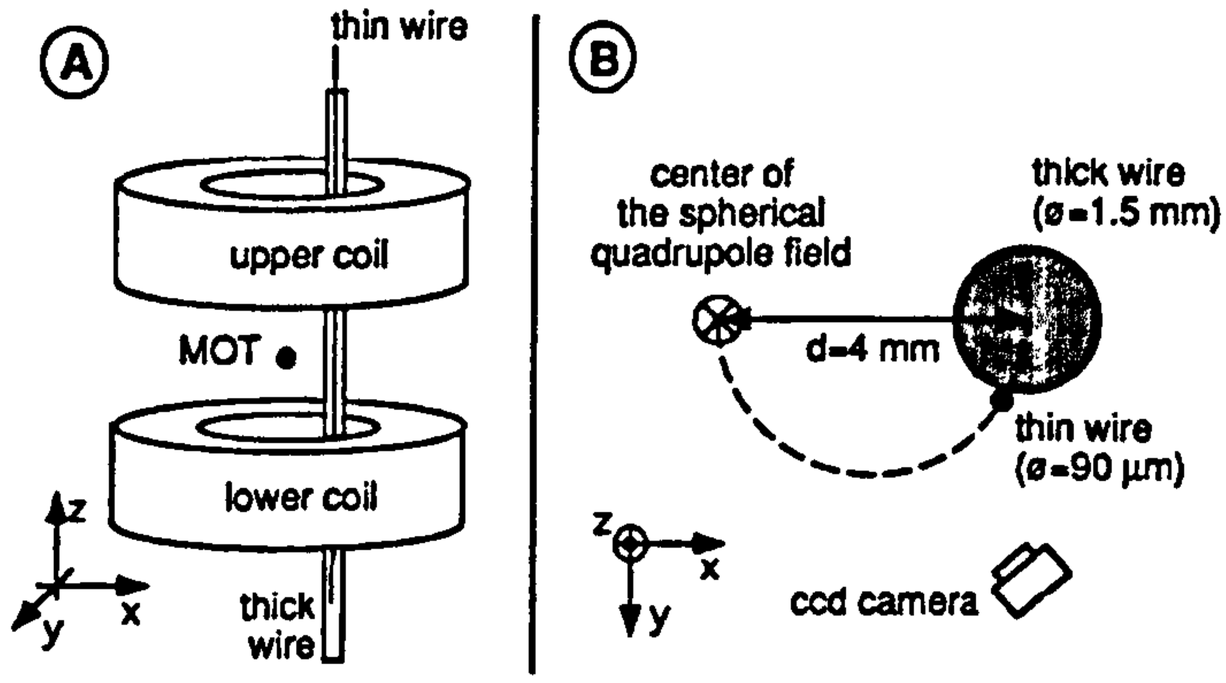

Figure 1.3: (a) Schematic representation of the trap reproduced from Ref. [41]. The trap is made of two coils, a thin wire and a thick wire. The wires are cemented together vertically and oriented parallel to the symmetry axis of the coils. (b) Schematic set up of the wires in the x-y plane and position of the center of the spherical quadrupole field.

The main goal of this thesis is to investigate relaxation processes of atoms near surfaces. For the present purpose is not necessary to go further into the details of different trapping geometries or microfabrication techniques.

1.2 Loss, heating and technical noise

In this Section the limitations of wire-based magnetic traps are discussed. The small separation between the cold atoms and the hot macroscopic environment of

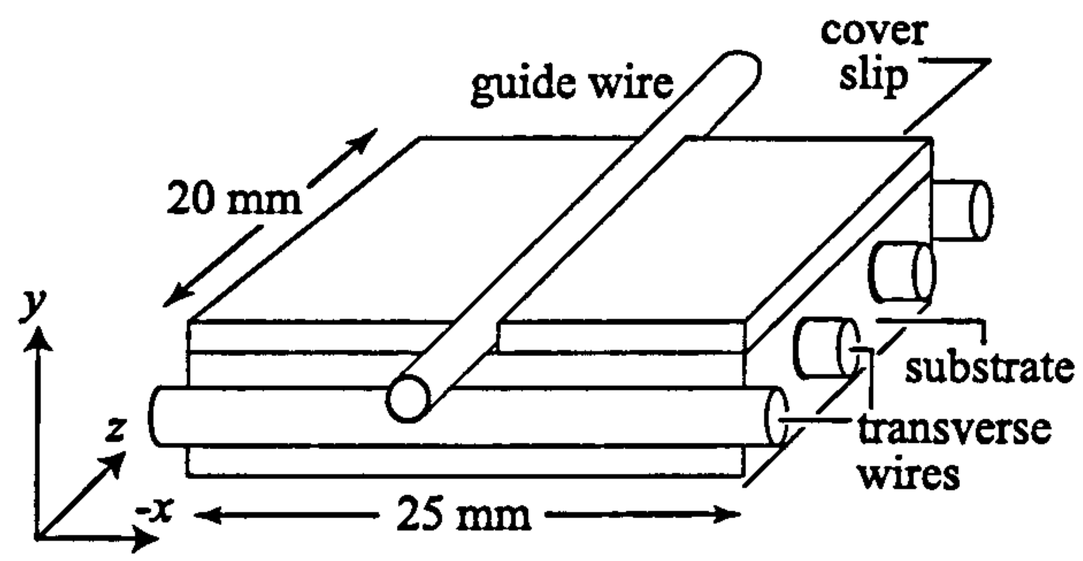

Figure 1.4: Atom chip set up reproduced from Ref. [8]. Atoms are trapped near the surface of the guide wire. The guide wire is made of copper and is glued on a glass substrate. A glass cover slip is added in order to obtain a smoother surface and to make the surface reflecting a particular frequency of the laser light which allows the formation of a magneto-optical trap by reflection.

the substrate raises the question of the smallest distance from the surface that can be reached while maintaining a strong atom confinement. The limiting phenomena that cause loss and decoherence are heating [45,46,100], background gas collisions [101,102] and magnetic field fluctuations [24]. Some of these noise sources have a technical origin and can be overcome experimentally. That is not possible for thermally-induced noise due to fluctuating magnetic fields in the substrate constituting the chip [7–10,45,46,51]. Fluctuations of the electromagnetic field will be reviewed in Section 1.3.

Loss, heating and interaction with a noisy environment of a particle bound in a harmonic trap potential is commonly described by a master equation [45]. The reduced dynamics of a system coupled to a reservoir is described by the coupling Hamiltonian

$$\hat{V}(\mathbf{r},t) = -g\,\hat{\mathbf{s}}\cdot\hat{\mathbf{F}}(\mathbf{r},t), \tag{1.16}$$

where $\hat{\mathbf{s}}$ denotes a system operator, g is a coupling constant and $\hat{\mathbf{F}}(\mathbf{r},t)$ stands for a fluctuating force. In the Markov limit, i.e. when in a coarse grained description of the system dynamics memory effects are disregarded, the relaxation dynamics

of the system density matrix $\hat{\rho}$ is expressed as

$$\begin{aligned}\dot{\hat{\rho}} &= -\frac{g^2}{\hbar^2}\sum_{ij}\frac{S_F^{ij}(\mathbf{r},\omega)}{2}\left(\hat{s}_i^{(-)}\hat{s}_j^{(+)}\hat{\rho}+\hat{\rho}\hat{s}_i^{(-)}\hat{s}_j^{(+)}-2\hat{s}_j^{(+)}\hat{\rho}\hat{s}_i^{(-)}\right)\\ &\quad -\frac{g^2}{\hbar^2}\sum_{ij}\frac{S_F^{ij}(\mathbf{r},-\omega)}{2}\left(\hat{s}_i^{(+)}\hat{s}_j^{(-)}\hat{\rho}+\hat{\rho}\hat{s}_i^{(+)}\hat{s}_j^{(-)}-2\hat{s}_j^{(-)}\hat{\rho}\hat{s}_i^{(+)}\right)\end{aligned} \tag{1.17}$$

where $\hat{\mathrm{s}}^{(\pm)}$ is the positive (negative) part of the system operator whose free evolution in Heisenberg picture is

$$\hat{\mathrm{s}}(t)=\hat{\mathrm{s}}^{(+)}e^{-i\omega t}+\hat{\mathrm{s}}^{(-)}e^{i\omega t}, \tag{1.18}$$

with $\hbar\omega$ denoting the energy difference between two adjacent system states. The spectral density of the force that appers in Eq. (1.17) is given by

$$S_F^{ij}(\mathbf{r},\omega)=\int_{-\infty}^{+\infty}d\tau\langle\hat{F}_i(\mathbf{r},t+\tau)\hat{F}_j(\mathbf{r},t)\rangle e^{i\omega\tau}. \tag{1.19}$$

In particular, the rates related to spontaneous and stimulated decay processes are proportional to $S_F^{ij}(\mathbf{r},+\omega)$ while the ones associated with excitation processes are proportional to $S_F^{ij}(\mathbf{r},-\omega)$. The force spectral density as expressed in Eq. (1.19) is the central tool used to describe transition rates for decoherence phenomena and atomic losses.

1.2.1 Atom loss mechanisms

Table 1.1 presents estimates of lifetimes corresponding to various loss mechanisms that are relevant for magnetic trapping experiments (taken from Ref. [24]). By technical noise are denoted all the mechanisms that arise from experimental manipulation and that can be kept under control experimentally such as cloud compression and fluctuations in the currents used to create the magnetic field. In the following a brief introduction is given for the most common processes leading to

atomic losses. An example of how decay rates may be derived is presented in the second part of this Section where the effects of a trap fluctuating in frequency or position are considered.

Table 1.1: Loss mechanisms for trapped atoms above curent carrying wires

Mechanism	Lifetime
heating	> 10 s
background collisions	> 10 s
technical noise (cloud compression and current fluctuations)	> 10 s
tunnelling	> 10 s
thermally-induced spin flips	$1 - 10$ s

Other noise sources are intrinsically connected to the way the atoms are trapped and the major one is represented by thermally-induced spin flips. The latter mechanism deserves more attention as it will be considered throughout this thesis, and is reviewed in Section 1.3.

- *Heating*
  Energy transfer to the atomic system, i.e. heating, causes the excitation of motional and vibrational degrees of freedom which leads to atomic loss or an ill-defined quantum state of the system. Heating arises primarily from audio-frequency technical noise in the currents and from the coupling to room-temperature surfaces, resulting in a trap fluctuating either in frequency or position [8, 45, 46, 100].

- *Background collisions*
  Collisions between background gas atoms and trapped atoms transfer enough energy to the latter so that they can escape the trap [101, 102]. For highly compressed traps and high-density atomic samples, collisions between trapped atoms occur as well. 2-body inelastic collisions cause spin exchange such that the magnetic number m_F is conserved while F itself is not [103, 104]. A weaker process resulting from 2-body inelastic collisions can also provoke

the spin relaxation such that m_F is not conserved [105, 106].

- *Cloud compression*

  Cloud compression represents a loss mechanism that in principle can be controlled experimentally. During manipulation and compression of the thermal atomic cloud, the cloud temperature may rise over the trap depth. This mechanism is often used to achieve thermalization of the atomic cloud [107].

- *Current fluctuations*

  Fluctuations in the currents used to generate the trapping potential cause radio-frequency noise that are able to induce spin flips [7, 8, 64]. This can be avoided by using 'quieter' current drivers such as superconducting wires or permanent magnets [22, 24].

- *Tunneling*

  Atoms in traps very close to the surface can tunnel out of the local minimum of the potential towards the surface. Tunnelling becomes important for states close to the top of the potential barrier, while for low-lying states the tunnelling lifetime has been estimated to be larger than 1000 s [24, 108].

Trapping losses and heating rates are generally described in terms of a master equation as introduced earlier in Sec. 1.2, and a simple harmonic-oscillator potential is often adopted to represent the trapping potential. The model presented in [100] consists of an atom in a one-dimensional harmonic-oscillator potential. Heating can be described as a transition to an higher excited state of the oscillator due to fluctuations in the spring constant or in the trap equilibrium position. For example, fluctuations $\Delta(k,t)$ in the spring constant can be modelled by the Hamiltonian

$$H(t) = \frac{p^2}{2M} + \frac{1}{2}M\omega_x^2[1 + \Delta(k,t)]x^2 \tag{1.20}$$

where M is the mass of the atom, $\omega_x^2 = k_x/M$ is the mean square trap oscillation frequency in the x direction and k_x the mean value of the corresponding spring

constant. Similarly, fluctuations in the trap equilibrium position are described by the Hamiltonian

$$H(t) = \frac{p^2}{2M} + \frac{1}{2}M\omega_x^2[x - \Delta(x,t)]^2 \tag{1.21}$$

where $\Delta(x,t)$ is the fluctuation in the location of the trap center. The corresponding Fokker-Planck equation and transition rates can be derived quantum mechanically using first-order time dependent perturbation theory. Regarding the Hamiltonian in Eq. (1.20) as a quantum-mechanical operator, a perturbation Hamiltonian $\hat{H}'(t)$ can be defined as $\hat{H}(t) = \hat{H}_0 + \hat{H}'(t)$ with

$$\hat{H}'(t) = \frac{1}{2}\Delta(k,t)M\omega_x^2 x^2. \tag{1.22}$$

The average transition rate from an atomic state $|i\rangle$ to a state $|f\rangle$ in a time interval T is given as

$$R_{i\to f} = \frac{1}{T}\left|\frac{-i}{\hbar}\int_0^T dt'\hat{H}'_{if}(t')e^{i\omega_{if}t'}\right|^2. \tag{1.23}$$

The average transition rate for fluctuations $\Delta(k,t)$ in the spring constant can be written as

$$R_{i\to f} = \left(\frac{M\omega_x^2}{2\hbar}\right)^2\int_0^T d\tau e^{i\omega_{if}\tau}\langle\Delta(k,0)\Delta(k,\tau)\rangle|\langle f|x^2|i\rangle|^2, \tag{1.24}$$

where the correlation function of the fluctuations is defined as

$$\langle\Delta(k,0)\Delta(k,\tau)\rangle \equiv \frac{1}{T}\int_0^T dt\Delta(k,t)\Delta(k,t+\tau). \tag{1.25}$$

The averaging time T is short compared to the time scale over which level populations vary, but still large enough when compared to the correlation time of the fluctuations such that the integration range over τ in Eq. (1.24) and over t in Eq. (1.25) can be extended formally to ∞, hence there is no explicit time dependence in the correlation function of the fluctuations. The power spectrum of

the fluctuations either in the spring constant $\Delta(k,t)$ or in the trap equilibrium position $\Delta(x,t)$, is then defined as

$$S(\omega) = \frac{2}{\pi}\int_0^\infty d\tau \cos\omega\tau\langle\Delta(0)\Delta(\tau)\rangle, \tag{1.26}$$

where $\Delta(t)$ denotes one of the two fluctuations mentioned above.

In particular, for a one-dimensional trap with atoms of energy $E = E_x$, fluctuations in the spring constant cause transitions between states $n \rightarrow n \pm 2$ with energy changes $\Delta E_x = \pm 2\hbar\omega_x$ and heating rate

$$\Gamma_{i\rightarrow i+2} = \frac{\pi\omega_x^2}{4}S_\omega(2\omega_x). \tag{1.27}$$

Similarly, position noise may induce transitions between states $n \rightarrow n \pm 1$ with energy changes $\Delta E_x = \pm\hbar\omega_x$ and corresponding rate

$$\Gamma_{i\rightarrow i+1} = \frac{M\omega_x^3}{4\hbar}S_x(\omega_x). \tag{1.28}$$

1.3 Near-field noise

In the context of atom chips, thermal magnetic noise has emerged as the crucial limitation to the atomic lifetime [7–10, 45, 46, 51]. The coupling of the atomic magnetic moment to fluctuating magnetic fields causes spin-flip transitions between hyperfine states of the atom [49]. Thermally-induced spin flip transitions are the focus of this Section. It is worth mentioning that magnetic fluctuations are also relevant in other contexts such as magnetic resonance-force microscopy [66] or when a high sensitivity is required from superconducting quantum interference devices (SQUID) [65].

Thermally induced spin flip transitions

Let $|i\rangle$ and $|f\rangle$ denote the atomic hyperfine states whose degeneracy is lifted by a magnetic field B, their Zeeman splitting is

$$\hbar\omega_{if} = g_F \mu_B |B| \tag{1.29}$$

where ω_{if} is the Larmor frequency. A subset of the atomic hyperfine sublevels experiences an attractive potential towards regions of low magnetic field. However, fluctuating magnetic fields couple spin states and thus cause the atom to evolve into untrapped states with a different m_F. Neutral alkali atoms can be efficiently manipulated by laser light and in particular rubidium atoms have become the preferred atomic species for research in quantum information processing, quantum optics and atomic physics. Throughout this thesis, ^{87}Rb atoms are considered and according to typical experimental realizations, the state $|F, m_F\rangle = |2, 2\rangle$ is considered as the initial state $|i\rangle$ where the atoms are trapped. In Fig. 1.5 the Zeeman splitting of the $|F = 2\rangle$ hyperfine ground state is depicted. In a sufficiently tight trap, atoms in the state $|F, m_F\rangle = |2, 1\rangle$ are also trapped but transitions to lower magnetic sublevels cause the atoms to be expelled from the trap.

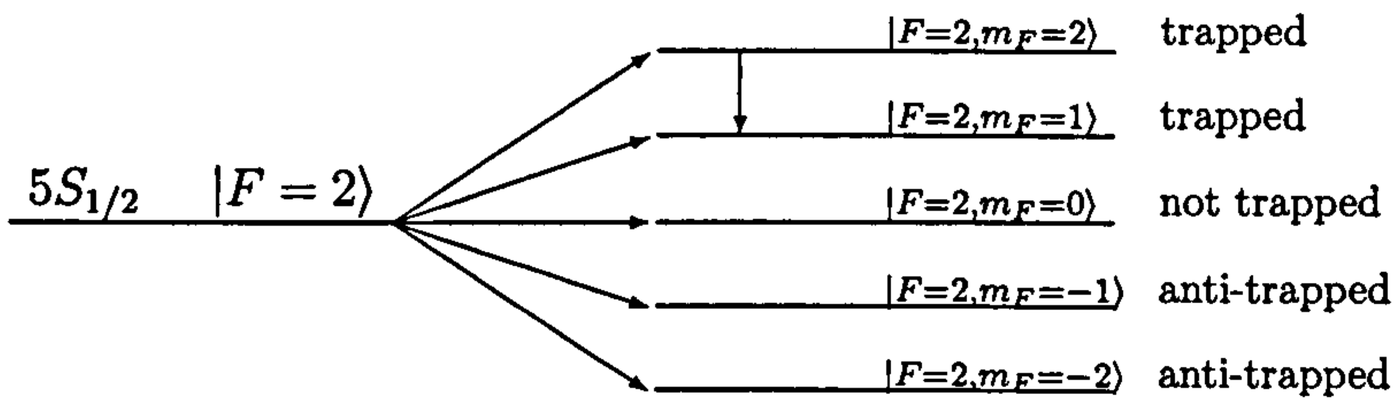

Figure 1.5: Zeeman splitting of the $|F = 2\rangle$ hyperfine ground state of ^{87}Rb. The spin-flip transition considered throughout this thesis is shown by the arrow.

The rate for spin-flip transitions is given by Fermi's golden rule that can be

expressed in terms of the magnetic field noise spectrum $S_B(\omega)$ as [48,69]

$$\Gamma^{B}_{i\longrightarrow f}(\mathrm{r}) = \frac{1}{\hbar^2}\sum_{\alpha,\beta=y,z}\langle i|\hat{\mu}_\alpha|f\rangle\langle f|\hat{\mu}_\beta|i\rangle S_B^{\alpha\beta}(\mathrm{r},\omega_{fi}) \tag{1.30}$$

where $\hat{\mu}_\alpha$ and $\hat{\mu}_\beta$ are the Cartesian components of the magnetic moment operator. The quantization axis is chosen to be parallel to the offset field B_0 directed along the wire direction (usually denoted as the z direction). The magnetic moment associated with the transition $|i\rangle \rightarrow |f\rangle$ is $\hat{\boldsymbol{\mu}} = \boldsymbol{\mu}|i\rangle\langle f| + \mathrm{h.c.}$ and the magnetic moment vector is given by

$$\boldsymbol{\mu} = \langle i|\mu_B\left(g_S\hat{\mathbf{S}} + g_L\hat{\mathbf{L}} - g_I\frac{m_e}{m_p}\hat{\mathbf{I}}\right)|f\rangle, \tag{1.31}$$

where μ_B is the Bohr magneton, $\hat{\mathbf{S}}$ is the electronic spin operator, $\hat{\mathbf{L}}$ is the orbital angular momentum operator, $\hat{\mathbf{I}}$ is the nuclear spin operator and $g_S(\sim 2)$, g_L and g_I are the corresponding g factors. An alkali-metal atom in its ground state has an angular momentum $L = 0$. Furthermore, the nuclear magnetic moment can be neglected because of the ratio of the electron mass m_e to the mass of the proton m_p. The magnetic moment vector is then proportional to the electronic spin operator

$$\boldsymbol{\mu} \simeq \langle i|\mu_B g_S\hat{\mathbf{S}}|f\rangle. \tag{1.32}$$

The spin matrix elements for the transition from one hyperfine state to another can be evaluated via Clebsch-Gordon coefficients $|F, m_F\rangle = \sum_{m_S m_I} C^{m_S m_I}_{F m_F}|m_S, m_I\rangle$. For the ^{87}Rb ground state transition $|2,2\rangle \rightarrow |2,1\rangle$ as represented in Fig. 1.5, the nonzero matrix elements are $|\langle i|\hat{S}_{x,y}|f\rangle| = 1/4$.

Noise spectrum

The spectral density of the fluctuating magnetic field at the atom's position $\mathbf{r}$ and transition frequency ω_{if} can be expressed according to Eq. (1.19) as

$$S_B^{\alpha\beta}(\mathbf{r},\omega_{if}) = \int_{-\infty}^{\infty} d\tau \langle B_\alpha(\mathbf{r},t+\tau)B_\beta(\mathbf{r},t)\rangle e^{i\omega_{if}\tau}, \tag{1.33}$$

which, in free space, is given by the thermal blackbody radiation spectrum

$$S_B^{\alpha\beta}(\mathrm{r},\omega) = \frac{\mu_0\hbar\omega^3}{3\pi c^3}(n_{\mathrm{th}}+1)\delta_{\alpha\beta}, \tag{1.34}$$

where

$$n_{\mathrm{th}} = 1/(e^{\hbar\omega/k_BT}-1) \tag{1.35}$$

is the mean number of thermal photons per mode at frequency ω. At zero temperature, the resulting spin-flip lifetime is

$$\tau_0 = \frac{1}{\Gamma^B_{i\to f}} = \frac{3\pi\hbar c^3}{\mu_0\omega^3\sum_\alpha \mu_B^2 g_F^2 |\langle f|\hat{S}_\alpha|i\rangle|^2}. \tag{1.36}$$

The presence of a surface enters in the free space calculations as a modification of the magnetic field spectrum $S_B^{\alpha\beta}(\mathrm{r},\omega)$. In the following, only the near field noise is taken into consideration given the close proximity of the atoms to the substrate. A calculation of the magnetic noise spectrum above a metal surface was done by Varpula and Poutanen [68] along the lines of the stochastic approach introduced by Rytov *et al.* [70]. The key idea is to consider a conductor as a dissipative medium with random fluctuations of charge and current. The noise current for each unit of volume can be calculated via Nyquist's theorem and the single spectral density contributions are incoherently summed to give the total magnetic field noise, which correspond to assume that the oscillations from each unit are not correlated to the ones coming from others units. In the context of microtraps, this approach was

adopted by Henkel in one of his works on coherent transport of matter waves [47].

An alternative approach using the fluctuation-dissipation theorem for the magnetic field itself was put forward by Agarwal [67]. A close investigation of the results obtained with the incoherent averaging used in [47,68] shows that the spin-flip loss rates have the correct order of magnitude, but differ by some numerical factor when compared to the results predicted by the fluctuation-dissipation theorem approach. The latter has been used by several authors to describe and calculate magnetic noise in small and noisy traps [45, 49–51]. In this method, the calculation is done for each dipole source. For example, if $\mathbf{F}(\mathbf{r},\omega)$ is the force field at a position $\mathbf{r}$ due to a classical disturbance localized at $\mathbf{r}_0$ (for example the electric field of an oscillating dipole located at $\mathbf{r}_0$), the average linear response to this field in thermal equilibrium conditions is proportional to the system variable $\mathbf{s}$ in terms of a Green tensor such that

$$\langle F_i(\mathbf{r},t;\mathbf{r}_0)\rangle = e^{-i\omega t}\sum_j G_{ij}(\mathbf{r},\mathbf{r}_0;\omega)s_j. \tag{1.37}$$

The fluctuation-dissipation theorem states that the correlation function of the fluctuating force, in this case the electric field, has to be proportional to the imaginary part of the response function, hence

$$S_F^{ij}(\mathbf{r}_1,\mathbf{r}_2;\omega) \propto 2\hbar(n_{\text{th}}+1)\text{Im}G_{ij}(\mathbf{r}_1,\mathbf{r}_2;\omega). \tag{1.38}$$

The total electromagnetic field is the sum of the field in vacuum plus the field reflected from the surface. The modification of the thermal radiation in the near field is contained in the Green tensor together with all the information on the dielectric matter.

The same conceptual framework is used in Ref. [49] where a first-principle derivation of the spin-flip transition rate is presented. The calculations are based on the quantization of an electromagnetic field in the presence of a dispersing and absorbing dielectric body as explained in Chapter 2. The idea is to add a

noise polarization to the macroscopic matter polarization in order to satisfy the fluctuation-dissipation theorem. The fluctuating part of the polarization accounts for the loss in the medium and plays an important role in the determination of the electric field. In particular, in Ref. [49] a general expression for the spontaneous and thermal spin-flip rates of an atom coupled to the magnetic field has been derived as

$$\Gamma^B_{i\to f} = \mu_0 \frac{2(\mu_B g_S)^2}{\hbar} \langle f|\hat{S}_q|i\rangle\langle i|\hat{S}_p|f\rangle (n_{\rm th}+1) {\rm Im}\left[\overrightarrow{\boldsymbol{\nabla}} \times \mathbf{G}(\mathbf{r},\mathbf{r},\omega_{if}) \times \overleftarrow{\boldsymbol{\nabla}}\right]_{qp}, \quad (1.39)$$

which exhibits a structure similar to Fermi's golden rule Eq. (1.30).

Lifetime dependence on length scales

The relevant length scales for the system of an atom above a planar substrate are given by the thickness of the substrate h, the atom-surface distance d and the skin depth δ [45, 47, 49–51, 67], as illustrated in Fig. (1.6). For certain regimes it is

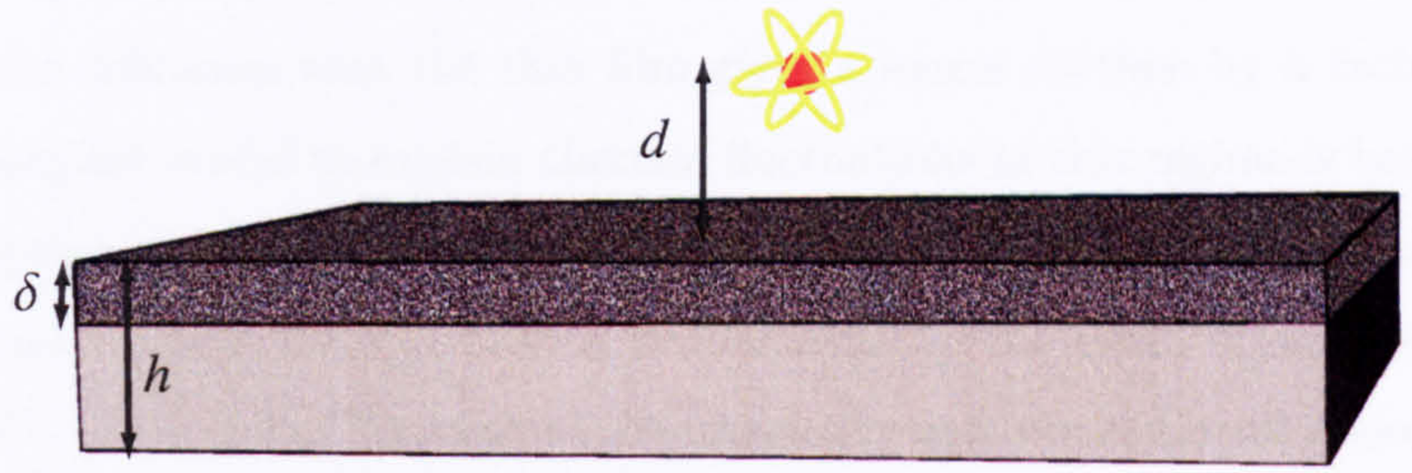

Figure 1.6: Schematic representation of the system geometry. The atom is located in vacuum at a distance d from a plain metallic layer of thickness h and skin depth δ.

possible to obtain analytical results for the spin-flip lifetime $\tau = 1/\Gamma^B$ as function

of those parameters as presented by Scheel *et al.* [50]

$$\tau \approx \left(\frac{8}{3}\right)^2 \frac{\tau_0}{n_{\rm th}+1}\left(\frac{\omega}{c}\right)^2 \begin{cases} \dfrac{d^4}{3\delta} & \delta \ll d, h, \\ \dfrac{\delta^2 d}{2} & \delta, h \gg d, \\ \dfrac{\delta^2 d^2}{2h} & \delta \gg d \gg h. \end{cases} \tag{1.40}$$

The trapping lifetime of an atom as a function of the skin depth has been discussed in detail in [50] and is found to be longer above a thin metal layer than above a bulk metal. In particular, the lifetime has a minimum for thin films at $\delta_{min} \sim \sqrt{hd}$, while for thick slabs the minimum is at $\delta_{min} \sim d$. Atom-surface distances of the order of the skin depth should then be avoided, however, for experimental realizations using metals such as copper or gold the typical atom-surface distances are roughly in this range [8, 10].

A thin metal film provides significantly longer lifetimes, (third line in Eq. (1.40)), with respect to a bulk material, (second line in Eq. (1.40)). In both cases $\tau \propto \delta^2$, with the difference that the thin film gives a longer lifetime by a factor of d/h.

The simplest model to explain thermal fluctuations in this regime is based on the assumption of local thermodynamic equilibrium. According to Henkel [51], the thermal-current noise spectrum is proportional to the mean occupation number $(e^{\hbar\omega/k_BT}-1)^{-1} \sim k_BT/\hbar\omega$ and to the imaginary part of the (local) dielectric function $\mathrm{Im}[\epsilon(\mathbf{r},\omega)]$. The latter is due to the phenomenon of absorption of excess field energy by the matter and will be explained in more detail in next Chapter. Only thermal currents in the skin layer, of thickness

$$\delta^2 = \frac{c^2}{\omega^2 \mathrm{Im}[\epsilon]} = \frac{2}{\mu_0 \sigma \omega}, \tag{1.41}$$

(with σ the substrate conductivity) contribute to the magnetic noise while the ones occurring in the rest of the substrate are damped before reaching the vicinity of the surface. The magnetic noise spectrum in the magnetostatic approximation

(valid at small distances $d \ll \delta$), is independent of frequency. The power laws are [47,51,52]

$$\text{half space}: \qquad S_B \sim \frac{1}{d}, \tag{1.42}$$

$$\text{thickness } h: \qquad S_B \sim \frac{h}{d^2}, \tag{1.43}$$

which are in agreement with the last two lines of Eq. (1.40).

For skin depths δ much smaller than the atom-surface distance d, the two cases of thick and thin slabs present the same behaviour. The radiating layer, i.e. the noise source, has the thickness of the order of δ, and the atomic lifetime scales as δ^{-1}, as described by the first line in Eq. (1.40). This power law can be understood by considering that the thermal-current noise spectrum is proportional to $\mathrm{Im}[\epsilon(\mathbf{r},\omega)]$. The incoherent summation of the contribution due to each dipole gives

$$\Gamma^B \propto \int_V d\mathbf{r}\, \mathrm{Im}[\epsilon(\mathbf{r},\omega)]\, e^{-\mathrm{r}/\delta} \propto \int_V d\mathrm{r}\, \frac{1}{\delta^2}\, e^{-\mathrm{r}/\delta}, \tag{1.44}$$

where $\mathbf{r}$ is the distance between every single radiating dipole from the source point, and the integral is performed over all the skin layer volume V. Scaling the length parameter $\mathbf{r}$ in Eq. (1.44) with δ gives a factor δ^3 such that $\Gamma^B = \tau^{-1} \propto \delta$. In the regime of $d \gg \delta$, the noise spectrum follows the power law $S_B \sim 1/d^4$ [45], which together with the δ^{-1} dependence explains the first line of Eq. (1.40).

As a consequence, the magnetic noise levels can be significantly reduced by decreasing the amount of absorbing material or adopting materials with virtually no resistivity. Both approaches are addressed in this thesis by considering a carbon nanotube as a current carrying wire in Chapter 3 and investigating the interaction of an atom with a thin superconducting film in Chapter 5.

1.3.1 Decoherence

The coupling of the atom to near-field magnetic noise can ultimately lead to the destruction of quantum superpositions or interferences [24, 109].

The theoretical framework used to describe decoherence usually adopts the density matrix formalism for the trapped atoms. The diagonal elements of the density matrix represent the occupation probabilities while the off-diagonal elements, or coherences, describe the quantum features of the system. The decay of those elements is referred to as decoherence. Magnetic-field fluctuations affect coherences and cause both the randomization of the relative phase in internal superposition states, i.e. phase noise, and the fluctuation of the center of mass motion, i.e. longitudinal decoherence.

Phase noise manifests itself in a shift of the Larmor frequency due to fluctuations in the magnetic field. As a consequence, the relative phase between spin states varies in a random way. The off-diagonal matrix elements of the atom's density matrix are proportional to $\langle \exp(i\Delta\varphi) \rangle$ where $\Delta\varphi$ is the phase shift accumulated during an interaction time t. Given two spin states $|m_F\rangle$ and $|m'_F\rangle$ and denoting by $\Delta B(t)$ the magnetic field noise, the corresponding frequency shift is [24]

$$\dot{\varphi}(t) = \frac{g\mu_B(m_F - m'_F)\Delta B(t)}{\hbar}, \tag{1.45}$$

which means that the spectrum $S_{\dot{\varphi}}(\omega)$ of the frequency fluctuations is proportional to the magnetic-field fluctuations. Near-field noise can perturb the coherence between different hyperfine states by inducing random transitions. In particular, spurious Raman transitions represent a source of decoherence whenever two hyperfine states are chosen as qubits to perform quantum gates [28, 31, 34, 36].

Coherence lifetimes of internal spin states have been measured by Treutelin *et al.* [32]. They realized a coherent superposition of the two hyperfine ground states $|F = 1, m_F = -1\rangle \equiv |0\rangle$ and $|F = 2, m_F = 1\rangle \equiv |1\rangle$ of ^{87}Rb. By means of Raman spectroscopy, the atomic cloud coherence-lifetime was measured for different atom-

surface distances d and was found to decrease from 11 s for $d < 20\,\mu$m, to 1.6 s for $d = 5\,\mu$m, which is in agreement with Eq. (1.40). They did not take measurements for smaller distances as the magnetic field fluctuations significantly limited the trapping lifetime.

Whenever the magnetic noise is not spatially homogeneous, scattering processes occur that leave the atoms in the magnetic trap but perturb their center of mass motion [24,47,48,53]. For example, fluctuations can induce decoherence by driving transitions between the motional states of the trapped atoms, (i.e. vibrational decoherence), and between transverse trap states, (i.e. longitudinal decoherence). Both phenomena can be described by assuming that the transverse motion is frozen out such that the motion along the guide axis z can be safely considered quasi-free. The quasi-free wavefunction for a trapped spin state $|s\rangle$ is perturbed by the magnetic potential

$$V(\mathbf{r},t) = \langle s|\mu_{\parallel}|s\rangle \Delta B_{\parallel}(\mathbf{r},t), \tag{1.46}$$

where $B_{\parallel}$ refers to the magnetic field component parallel to the wire. The evolution of the atomic density matrix in the position representation describes the decoherence in terms of a rate $\Gamma_{\rm dec}(l)$ as a function of the spatial separation $l = z - z'$. In particular, a spatial decoherence rate has been derived in Ref. [47] in the context of matter-wave transport in waveguides. In Chapter 4 of this thesis, similar results are obtained by a first principle derivation of spatial atomic-sublevel decoherence near dielectric and metallic surfaces and an analytical study for small separations is presented.

1.3.2 The Casimir–Polder interaction

The structure of the vacuum electromagnetic field is strongly modified in the vicinity of a dielectric surface. In particular, at a distance d from the surface the spatial distribution and spectral density of the electromagnetic field are substantially altered for frequencies below c/d. In the presence of macroscopic bodies, an atom experiences a nonvanishing force due to electromagnetic field fluctuations which

induce virtual electronic transitions and energy shifts known as Lamb shifts. An attractive force originates from the gradients of the spatially varying Lamb shifts.

The first discussion of this effect dates back to 1948 and to the work of Casimir and Polder [13]. Several theoretical approaches have been subsequently developed [12, 14, 16, 17]. The range of the van der Waals interaction is limited by distances of the order of $\lambda/2\pi$, where λ is the wavelength of the dominant virtual dipole transitions of the atom. For alkali-metal atoms, λ is the wavelength of the D_1 and D_2 transitions. In the short distance regime $d \ll \lambda/2\pi$, the potential is described by a power law $U_{vdW} \propto 1/d^3$, while for distances $d \gg \lambda/2\pi$ the potential becomes weaker. It approaches the power law $U_{CP} \propto 1/d^4$ for large distances. The very first measurement of the Casimir-Polder force has been reported by Hinds *et al.* in [15] and more precise estimations have been presented later on by Harber *et al.* in [11].

In the context of microtraps, the effect of the Casimir-Polder potential is to lower the trap depth which causes the loss of atoms towards the chip surface. Lifetime measurements at different heights have been performed by Lin *et al.* [10], which indicate that dispersion forces have a short decay length and compete with the confining potential such that the trap disappears at finite distances d from the surface.

The approximation of the Casimir-Polder potential as a step potential suggests the occurrence of quantum reflection. Interpolating the two asymptotic behaviours above, the Casimir-Polder potential for an atom at a distance d from a solid surface can be approximated by [18]

$$U_{CP} = -\frac{C_4}{(r + 3\lambda/2\pi^2)r^3}. \tag{1.47}$$

Classically, an atom incident on such a potential will be accelerated toward the surface and would experience either inelastic scattering or absorption. A quantum mechanical treatment of an atom-surface collision reveals that the atom is reflected from the purely attractive surface potential, if the potential energy changes

abruptly on a length scale comparable with the atom wavelength. Quantum reflection of ultracold atoms from the attractive potential of a solid surface has been studied by Pasquini *et al.* [18, 19], who observed reflection probabilities of up to 60 % at low incident velocities (0.5-2.5 mm/s), and showed that the Casimir-Polder potential can be shaped by structuring the surface.

2

QED in dielectric matter

In recent years, there has been considerable interest in the properties of radiation fields in the presence of absorbing dielectric matter. The polarization of the medium alters dramatically the ground-state fluctuations of the electromagnetic fields compared to free space. In particular, a medium with dielectric properties modifies an electromagnetic field imposed on it. The responses of some media may be described in terms of induced dipole moments or induced current density. Those responses affect the statistical properties of the electromagnetic field, typical consequences being the Casimir effect [10–15] and the modification of spontaneous emission rate of excited atoms [20,21]. Moreover, as seen in the previous Chapter, the behaviour of atoms magnetically trapped near a dielectric body is strongly altered by the coupling with fluctuating fields taking place inside the material. In order to deal explicitly with the statistical and quantum properties of fields in dielectric media, the quantization of those fields is required.

The quantum theory of radiation in the presence of dielectric bodies has been widely studied and the quantization of the electromagnetic field in dielectric media with assumed real and frequency-independent permittivity has been proposed in various schemes [110–112]. Dispersive dielectrics have been considered as well, however, a dielectric that shows dispersion must be lossy and its permittivity,

which is a complex function of frequency, has to satisfy the Kramers-Kronig relations [113, 114]. They state that the real part of the permittivity (responsible for dispersion) and the imaginary part (responsible for absorption) are connected with one another. The existence of the imaginary part of the permittivity does not allow the usual mode expansion of the electromagnetic field. An expansion of the field in terms of damped (nonorthogonal) waves would not be complete, at least in frequency ranges where the absorption cannot be neglected.

An increasing number of investigations have been dedicated to a novel formulation of quantum electrodynamics in dielectric media with complex permittivity [71–75, 115–122]. A quantum-mechanically consistent approach presented initially by Huttner and Barnett [115] relies on the microscopic Hopfield model of a bulk dielectric [123]. The dielectric is described as a polarization field and a continuum of reservoir fields accounting for absorption, and the radiation-matter Hamiltonian is diagonalized performing a Fano-type diagonalization [124,125]. The resulting vector potential is expressed in terms of the Green tensor of the classical scattering problem and frequency-dependent bosonic field operators are introduced. The electromagnetic field operators are then expressed in terms of those fundamental bosonic field operators via the Green tensor.

This Chapter focuses on how the classical phenomenological Maxwell equations of the electromagnetic field in the presence of dielectric matter can be transferred to quantum theory. In Section 2.1, the basic properties of Maxwell equations are summarized and a polarization noise accounting for absorption in dielectrics is introduced. In Sec. 2.2, the quantization is performed by replacing the dynamical field variables with bosonic field operators.

2.1 Basic equations

The propagation of radiation in a dispersive and lossy linear dielectric that is free of external sources is frequently described by the phenomenological Maxwell

equations [126–128]

$$\nabla \cdot \mathbf{D}(\mathbf{r},t) = 0, \tag{2.1}$$

$$\nabla \times \mathbf{H}(\mathbf{r},t) - \dot{\mathbf{D}}(\mathbf{r},t) = 0, \tag{2.2}$$

$$\nabla \times \mathbf{E}(\mathbf{r},t) + \dot{\mathbf{B}}(\mathbf{r},t) = 0, \tag{2.3}$$

$$\nabla \cdot \mathbf{B}(\mathbf{r},t) = 0, \tag{2.4}$$

where $\mathbf{E}$ and $\mathbf{B}$ denote the electric field and magnetic induction. The electric displacement $\mathbf{D}$ and the magnetic field $\mathbf{H}$ are the corresponding derived fields which, for a dielectric responding linearly to the electric field, are defined according to

$$\mathbf{D}(\mathbf{r},t) = \varepsilon_0 \left[\mathbf{E}(\mathbf{r},t) + \int_0^\infty d\tau\, \chi(\mathbf{r},\tau)\, \mathbf{E}(\mathbf{r},t-\tau) \right], \tag{2.5}$$

where $\chi(\mathbf{r},t)$ is the dielectric susceptibility, and for non-magnetic matter it may be assumed that

$$\mathbf{H}(\mathbf{r},t) = \frac{1}{\mu_0}\mathbf{B}(\mathbf{r},t). \tag{2.6}$$

The electric field and the magnetic induction can be expressed in terms of the vector potential $\mathbf{A}$ as

$$\mathbf{E}(\mathbf{r},t) = -\dot{\mathbf{A}}(\mathbf{r},t), \tag{2.7}$$

$$\mathbf{B}(\mathbf{r},t) = \nabla \times \mathbf{A}(\mathbf{r},t), \tag{2.8}$$

and the Maxwell equations are satisfied when

$$\nabla^2 \mathbf{A}(\mathbf{r},t) - \frac{1}{c^2}\left[\ddot{\mathbf{A}}(\mathbf{r},t) + \int_0^\infty d\tau\, \chi(\mathbf{r},\tau)\, \ddot{\mathbf{A}}(\mathbf{r},t-\tau) \right] = 0. \tag{2.9}$$

To discuss dispersion it will be necessary to make a Fourier decomposition of $\mathbf{E}(\mathbf{r},t)$ and $\mathbf{D}(\mathbf{r},t)$ [and $\mathbf{B}(\mathbf{r},t)$ and $\mathbf{H}(\mathbf{r},t)$], and $\mathbf{A}(\mathbf{r},t)$ as

$$\mathbf{A}(\mathbf{r},t) = \int_{-\infty}^{\infty} d\omega \underline{\mathbf{A}}(\mathbf{r},\omega)e^{-i\omega t}, \tag{2.10}$$

such that Eq. (2.5) becomes

$$\underline{\mathbf{D}}(\mathbf{r},\omega) = \varepsilon_0\varepsilon(\mathbf{r},\omega)\underline{\mathbf{E}}(\mathbf{r},\omega), \tag{2.11}$$

where the underlined quantities represent the respective Fourier components. The permittivity $\varepsilon(\mathbf{r},\omega)$ is defined as

$$\varepsilon(\mathbf{r},\omega) = 1 + \int_{0}^{\infty} d\tau e^{i\omega t}\chi(\mathbf{r},\tau), \tag{2.12}$$

and because the susceptibility $\chi(\mathbf{r},\tau)$ is a real function yielding a real polarization field, the permittivity is in general a complex function of frequency, $\varepsilon(\mathbf{r},\omega) = \varepsilon_R(\mathbf{r},\omega)+i\varepsilon_I(\mathbf{r},\omega)$. Its real and imaginary parts, which are respectively responsible for dispersion and absorption, are uniquely related to one another via the Kramers-Kronig relations [113, 114]

$$\varepsilon_R(\mathbf{r},\omega) - 1 = \frac{\mathcal{P}}{\pi}\int d\omega' \frac{\varepsilon_I(\mathbf{r},\omega')}{\omega' - \omega}, \tag{2.13}$$

$$\varepsilon_I(\mathbf{r},\omega) = -\frac{\mathcal{P}}{\pi}\int d\omega' \frac{\varepsilon_R(\mathbf{r},\omega') - 1}{\omega' - \omega}, \tag{2.14}$$

where $\mathcal{P}$ denotes the principal value. Furthermore, $\varepsilon(\mathbf{r},\omega)$ as a function of complex ω satisfies the relation

$$\varepsilon(\mathbf{r},-\omega^*) = \varepsilon^*(\mathbf{r},\omega), \tag{2.15}$$

and is holomorphic in the upper complex half-plane without zeros.

The wave equation (2.9) is satisfied when

$$\nabla^2 \underline{\mathbf{A}}(\mathbf{r},\omega) + \frac{\omega^2}{c^2}\varepsilon(\mathbf{r},\omega)\underline{\mathbf{A}}(\mathbf{r},\omega) = 0. \tag{2.16}$$

In quantum theory, Eq. (2.9) and Eq. (2.16) are not valid as operator equations for $\hat{\mathbf{A}}(\mathbf{r},t)$ and $\underline{\hat{\mathbf{A}}}(\mathbf{r},\omega)$, otherwise $\hat{\mathbf{A}}(\mathbf{r},t)$ and $\underline{\hat{\mathbf{A}}}(\mathbf{r},\omega)$ would be spatially damped and the equal-time canonical commutation relation, i.e. of the field $\left[\hat{\mathbf{A}}_i(\mathbf{r},t), \hat{\mathbf{E}}_j(\mathbf{r}',t)\right] = -\frac{i\hbar}{\varepsilon_0}\delta_{ij}^{\perp}(\mathbf{r}-\mathbf{r}')$, would not be preserved, and you can see that $\hat{\mathbf{E}}(\mathbf{r},t)$ is the canonical conjugate of $\hat{\mathbf{A}}(\mathbf{r},t)$. From the quantum theory of damped systems, it is well known that the transfer of classical evolution equations to quantum operator equations requires the introduction of additional noise operator sources into the equations. The noise that is unavoidably associated with absorption can be though of as arising from a noise current $\mathbf{J}_N$ such that

$$\nabla^2 \underline{\mathbf{A}}(\mathbf{r},\omega) + \frac{\omega^2}{c^2}\varepsilon(\mathbf{r},\omega)\underline{\mathbf{A}}(\mathbf{r},\omega) = \underline{\mathbf{J}}_N(\mathbf{r},\omega). \tag{2.17}$$

An equivalent way of including absorption is by introducing a macroscopic polarization noise term $\mathbf{P}_N$ in the relation between the electric displacement $\mathbf{D}$ and the electric field $\mathbf{E}$ as

$$\underline{\mathbf{D}}(\mathbf{r},\omega) = \varepsilon_0\varepsilon(\mathbf{r},\omega)\underline{\mathbf{E}}(\mathbf{r},\omega) + \underline{\mathbf{P}}_N(\mathbf{r},\omega), \tag{2.18}$$

such that

$$\underline{\mathbf{J}}_N(\mathbf{r},\omega) = -i\omega\underline{\mathbf{P}}_N(\mathbf{r},\omega), \tag{2.19}$$

In general, the dependence of $\mathbf{P}(\mathbf{r})$ on the electric field is rather complicated and highly non-linear. Here, the attention is restricted to the first term in the perturbative expansion of $\mathbf{P}(\mathbf{E})$ and therefore to media that respond linearly and locally to the electric field such as

$$\underline{\mathbf{P}}(\mathbf{r},\omega) = \varepsilon_0[\varepsilon(\mathbf{r},\omega) - 1]\underline{\mathbf{E}}(\mathbf{r},\omega) + \underline{\mathbf{P}}_N(\mathbf{r},\omega). \tag{2.20}$$

The Maxwell equations (2.1-2.4) in the frequency domain and in presence of a medium now read

$$\begin{aligned}
\varepsilon_0 \nabla \cdot \varepsilon(\mathbf{r},\omega)\underline{\mathbf{E}}(\mathbf{r},\omega) &= \underline{\rho}_N(\mathbf{r},\omega), && (2.21)\\
\nabla \times \underline{\mathbf{B}}(\mathbf{r},\omega) + i\frac{\omega}{c^2}\varepsilon(\mathbf{r},\omega)\underline{\mathbf{E}}(\mathbf{r},\omega) &= \mu_0 \underline{\mathbf{J}}_N(\mathbf{r},\omega), && (2.22)\\
\nabla \times \underline{\mathbf{E}}(\mathbf{r},\omega) - i\omega\underline{\mathbf{B}}(\mathbf{r},\omega) &= 0, && (2.23)\\
\nabla \cdot \underline{\mathbf{B}}(\mathbf{r},\omega) &= 0, && (2.24)
\end{aligned}$$

where $\rho_N(\mathbf{r},\omega)$ is the noise charge density, defined as

$$\underline{\rho}_N(\mathbf{r},\omega) = -\nabla \cdot \underline{\mathbf{P}}_N(\mathbf{r},\omega), \tag{2.25}$$

which obeys the continuity equation

$$\nabla \cdot \underline{\mathbf{J}}_N(\mathbf{r},\omega) = i\omega\underline{\rho}_N(\mathbf{r},\omega). \tag{2.26}$$

The Maxwell equations (2.22) and (2.23) imply that $\underline{\mathbf{E}}(\mathbf{r},\omega)$ satisfies the partial differential equation

$$\nabla \times \nabla \times \underline{\mathbf{E}}(\mathbf{r},\omega) - \frac{\omega^2}{c^2}\varepsilon(\mathbf{r},\omega)\underline{\mathbf{E}}(\mathbf{r},\omega) = i\omega\mu_0\underline{\mathbf{J}}_N(\mathbf{r},\omega), \tag{2.27}$$

which is solvable in terms of the dyadic Green function $\boldsymbol{G}(\mathbf{r},\mathbf{r}',\omega)$ as

$$\underline{\mathbf{E}}(\mathbf{r},\omega) = i\omega\mu_0 \int d^3\mathbf{r}' \boldsymbol{G}(\mathbf{r},\mathbf{r}',\omega)\cdot\underline{\mathbf{J}}_N(\mathbf{r}',\omega). \tag{2.28}$$

The Green tensor has to be determined from the Helmholtz equation

$$\nabla \times \nabla \times \boldsymbol{G}(\mathbf{r},\mathbf{r}',\omega) - \frac{\omega^2}{c^2}\varepsilon(\mathbf{r},\omega)\boldsymbol{G}(\mathbf{r},\mathbf{r}',\omega) = \delta(\mathbf{r}-\mathbf{r}') \tag{2.29}$$

together with the boundary conditions at infinity. In Cartesian coordinates, Eq. (2.29)

reads

$$\left[\partial_i^r \partial_k^r - \delta_{ik}\frac{\omega^2}{c^2}\varepsilon(\mathbf{r},\omega)\right] G_{kj}(\mathbf{r},\mathbf{r}',\omega) = \delta_{ij}\delta(\mathbf{r}-\mathbf{r}') \tag{2.30}$$

($\partial_i^r = \partial/\partial x_i$), where repeated vector indices are summed. An important consequence of the differential equation (2.30) is the integral relation [75]

$$\int d^3\mathbf{s}\frac{\omega^2}{c^2}\varepsilon_I(\mathbf{s},\omega)\boldsymbol{G}(\mathbf{r},\mathbf{s},\omega)\cdot\boldsymbol{G}^*(\mathbf{r}',\mathbf{s},\omega) = \mathrm{Im}[\boldsymbol{G}(\mathbf{r},\mathbf{r}',\omega)]. \tag{2.31}$$

The Green tensor has the following properties [76]

$$G_{ij}^*(\mathbf{r},\mathbf{r}',\omega) = G_{ij}(\mathbf{r},\mathbf{r}',-\omega^*), \tag{2.32}$$

$$G_{ij}(\mathbf{r}',\mathbf{r},\omega) = G_{ji}(\mathbf{r},\mathbf{r}',\omega). \tag{2.33}$$

Eq. (2.32) is a direct consequence of the relation (2.15) for the permittivity. More details about these properties and their proofs are given in [76].

2.2 Field quantization

The Maxwell equations (2.21)-(2.24) can be transferred to quantum theory by regarding the electromagnetic field and the noise polarization field as operators. As shown in Eq. (2.25) and Eq. (2.19), the source terms $\hat{\underline{\rho}}_N(\mathbf{r},\omega)$ and $\hat{\underline{\mathbf{J}}}_N(\mathbf{r},\omega)$ are closely related to the noise associated with the losses in the medium, which themselves are described by the imaginary part of the permittivity. The current density $\hat{\underline{\mathbf{J}}}_N(\mathbf{r},\omega)$ can be related to a bosonic vector field $\hat{\mathbf{f}}(\mathbf{r},\omega)$ as shown in [73,116], as

$$\hat{\underline{\mathbf{J}}}_N(\mathbf{r},\omega) = \omega\sqrt{\frac{\hbar\varepsilon_0}{\pi}\varepsilon_I(\mathbf{r},\omega)}\hat{\mathbf{f}}(\mathbf{r},\omega) \tag{2.34}$$

where $\hat{\mathbf{f}}(\mathbf{r},\omega)$ and $\hat{\mathbf{f}}^\dagger(\mathbf{r},\omega)$ represent the collective excitations of the electromagnetic field, in terms of medium polarization and the absorbing dielectric medium. They

satisfy the commutation relations

$$\left[\hat{f}_k(\mathbf{r},\omega), \hat{f}^{\dagger}_{k'}(\mathbf{r}',\omega')\right] = \delta_{kk'}\delta(\mathbf{r}-\mathbf{r}')\delta(\omega-\omega'), \tag{2.35}$$

$$\left[\hat{f}_k(\mathbf{r},\omega), \hat{f}_{k'}(\mathbf{r}',\omega')\right] = 0. \tag{2.36}$$

and the Hamiltonian of the composed system reads

$$\hat{H} = \int d^3\mathbf{r} \int_0^{\infty} d\omega\, \hbar\omega \hat{\mathbf{f}}^{\dagger}(\mathbf{r},\omega)\cdot\hat{\mathbf{f}}(\mathbf{r},\omega). \tag{2.37}$$

Combining Eq. (2.19) and Eq. (2.34), it is now possible to write the noise polarization as

$$\underline{\hat{\mathbf{P}}}_N(\mathbf{r},\omega) = i\sqrt{\frac{\hbar\epsilon_0}{\pi}\epsilon_I(\mathbf{r},\omega)}\,\hat{\mathbf{f}}(\mathbf{r},\omega). \tag{2.38}$$

In order to understand the physical meaning of $\hat{\mathbf{f}}(\mathbf{r},\omega)$, it is worth to develop the quantization scheme for the electromagnetic field in dispersive and absorptive linear dielectrics developed by Huttner and Barnett [115]. Their scheme is based on the Hopfield microscopic model for a bulk dielectric [123] where the matter is represented by a harmonic polarization field due to a collection of N harmonic oscillator fields. The polarization field is coupled to a continuum of harmonic oscillators representing a reservoir. The phenomenon of absorption is explained as a flow of energy from the medium to the reservoir. The coupled radiation-matter Hamiltonian is bilinear, such as $\hat{H}_{\text{int}} \propto \hat{\mathbf{p}}\cdot\hat{\mathbf{A}}$ ($\hat{\mathbf{p}}$ is the momentum of a charged particle, and $\hat{\mathbf{A}}$ the vector potential). After a Bogoliubov transformation, the vector potential $\hat{\mathbf{A}}$ can be expressed in terms of the basic field variables $\hat{\mathbf{f}}(\mathbf{r},\omega)$ and $\hat{\mathbf{f}}^{\dagger}(\mathbf{r},\omega)$, regarded as the annihilation and creation operators for the eigenmodes of the system, also known as polaritons. The Hamiltonian $\hat{H}_{\text{int}}$ can be diagonalized by performing a Fano-type diagonalization [115] and it assumes the form shown in Eq. (2.37).

The classical electromagnetic fields $\underline{\mathbf{E}}(\mathbf{r},\omega)$ and $\underline{\mathbf{B}}(\mathbf{r},\omega)$, will now be regarded

as operators and the combination of Eq. (2.19), Eq. (2.28) and Eq. (2.38) leads to

$$\underline{\hat{\mathbf{E}}}(\mathbf{r},\omega) = i\sqrt{\frac{\hbar}{\pi\varepsilon_0}}\frac{\omega^2}{c^2}\int d^3\mathbf{r}'\sqrt{\varepsilon_I(\mathbf{r}',\omega)}\boldsymbol{G}(\mathbf{r},\mathbf{r}',\omega)\cdot\hat{\mathbf{f}}(\mathbf{r}',\omega), \tag{2.39}$$

$$\underline{\hat{\mathbf{B}}}(\mathbf{r},\omega) = (i\omega)^{-1}\boldsymbol{\nabla}\times\underline{\hat{\mathbf{E}}}(\mathbf{r},\omega). \tag{2.40}$$

Integration over ω then yields the electromagnetic field operators in the Schrödinger picture

$$\hat{\mathbf{E}}(\mathbf{r}) = \int_0^\infty d\omega\underline{\hat{\mathbf{E}}}(\mathbf{r},\omega) + H.c., \tag{2.41}$$

$$\hat{\mathbf{B}}(\mathbf{r}) = \int_0^\infty d\omega\underline{\hat{\mathbf{B}}}(\mathbf{r},\omega) + H.c.. \tag{2.42}$$

This quantization scheme satisfies the basic requirements of quantum theory, in the form of equal-time commutation relations, and statistical physics, in terms of the fluctuation-dissipation theorem. It has been shown in [76] that the electric and magnetic field respect the correct commutation relations

$$\left[\hat{E}_k(\mathbf{r}),\hat{E}_l(\mathbf{r}')\right] = \left[\hat{B}_k(\mathbf{r}),\hat{B}_l(\mathbf{r}')\right] = 0, \tag{2.43}$$

$$\left[\varepsilon_0\hat{E}_k(\mathbf{r}),\hat{B}_l(\mathbf{r}')\right] = -i\hbar\epsilon_{klm}\partial^r_m\delta(\mathbf{r}-\mathbf{r}'). \tag{2.44}$$

A way to see that the fluctuation-dissipation theorem [126] is satisfied, is to consider the vacuum expectation values of the correlation function of $\underline{\hat{\mathbf{E}}}(\mathbf{r},\omega)$ and $\underline{\hat{\mathbf{B}}}(\mathbf{r},\omega)$ at zero temperature

$$\langle\underline{\hat{\mathbf{E}}}_k(\mathbf{r},\omega)\underline{\hat{\mathbf{E}}}^\dagger_l(\mathbf{r}',\omega')\rangle = \frac{\hbar\omega^2\mu_0}{\pi}\mathrm{Im}\left[\boldsymbol{G}(\mathbf{r},\mathbf{r}',\omega)\right]_{kl}\delta(\omega-\omega'), \tag{2.45}$$

$$\langle\underline{\hat{\mathbf{B}}}_k(\mathbf{r},\omega)\underline{\hat{\mathbf{B}}}^\dagger_l(\mathbf{r}',\omega')\rangle = \frac{\hbar\mu_0}{\pi}\mathrm{Im}\left[\overrightarrow{\boldsymbol{\nabla}}\times\boldsymbol{G}(\mathbf{r},\mathbf{r}',\omega)\times\overleftarrow{\boldsymbol{\nabla}}\right]_{kl}\delta(\omega-\omega'). \tag{2.46}$$

The above equations illustrate that the fluctuations of the electric field are determined by the imaginary part of the Green tensor, while the fluctuations of the magnetic field are determined by the imaginary part of the curl of the Green tensor taken with respect to both position arguments $\mathbf{r}$ and $\mathbf{r}'$. Both relations are consis-

tent with the fluctuation-dissipation theorem, as the Green tensor (or the curl of the Green tensor) plays the role of the response function of the electric (magnetic) field to an external perturbation. Moreover, if the system of the electromagnetic field and absorbing matter is in thermal equilibrium at some temperature T, the correlation function of the dynamical variables reads

$$\langle \hat{\mathbf{f}}(\mathbf{r},\omega)\hat{\mathbf{f}}^{\dagger}(\mathbf{r}',\omega')\rangle = (\bar{n}_{\mathrm{th}}+1)\delta(\mathbf{r}-\mathbf{r}')\delta(\omega-\omega')\boldsymbol{U}, \tag{2.47}$$

with $\boldsymbol{U}$ the unit dyad and $\bar{n}_{\mathrm{th}}$ the mean thermal photon number given in Eq. (1.35), such that the expectation value of the magnetic field fluctuation can be written as

$$\langle \hat{\underline{\mathbf{B}}}(\mathbf{r},\omega)\hat{\underline{\mathbf{B}}}^{\dagger}(\mathbf{r}',\omega')\rangle = \frac{\hbar\mu_0}{\pi}\mathrm{Im}\left[\overrightarrow{\boldsymbol{\nabla}}\times\boldsymbol{G}(\mathbf{r},\mathbf{r}',\omega)\times\overleftarrow{\boldsymbol{\nabla}}\right](\bar{n}_{\mathrm{th}}+1)\delta(\omega-\omega'). \tag{2.48}$$

Finally, it is worth pointing out the limitations of the quantization scheme presented in this Chapter. The form of the polarization, Eq. (2.38), is valid only for strictly locally responding materials. This is equivalent to the assumption that the elementary dipoles linked to the polarization are essentially fixed in space. Certainly, for metals this is not true as charge carriers can move around freely for considerable distances. However, the locality assumption can be upheld in situations in which the mean free path length of the conduction electrons is much shorter than all the other length scales in the system under consideration. While this is certainly true for ordinary metals at room temperature and geometric length scales of several micrometers, corrections due to spatially nonlocal response (the anomalous skin effect) are expected for metals or superconductors at very low temperatures as considered in [50,51].

3

Trapping an atom near a carbon nanotube

The creation of microscopic traps and guides for neutral atoms close to surfaces is possible using nanofabricated structures. Long trapping lifetimes and robust confinement are the key requirement when neutral atoms need to be prepared and manipulated efficiently. Both objectives are achievable by reducing the dimensions of the atomic traps as much as possible and by choosing materials with low magnetic field noise.

The trapping magnetic field may be tailored to achieve ever shorter atom-surface distances. However, an atom located in close proximity to an absorbing dielectric body undergoes thermally-induced spin-flip transitions that result in the atomic loss [8–10]. The origin of these transitions lies in fluctuating electromagnetic fields which can be attributed to resistive noise in the substrate [7–10, 45, 46, 49, 51]. In addition, these fluctuations interact with the atom and induce virtual electronic transitions that lead to an attractive force — the Casimir–Polder force [10–17]. The potential generating this force adds to the magnetic confining potential, thereby lowering the trap depth and causing the trap to become unstable at small distances. The reduction of magnetic fluctuations is possible either by using materials with less resistive noise or by using a smaller amount of dielectric matter to trap the atoms [50]. This Chapter address the latter case by

putting forward the idea of adopting carbon nanotubes (CNs) as current carrying wires.

Carbon nanotubes are graphene sheets rolled up into cylinders with diameters of the order of a few nanometers (see, for example Ref. [77]). The extensive work carried out on CN has revealed their intriguing properties [78, 79] and their possible utility in the miniaturization of many different devices such as electronic, mechanical, and scanning probe devices [80]. Given their electrical properties and their reduced dimensions, CNs seem to represent rather attractive structures for the design of miniaturized magnetic traps [81]. Since disorder is generally weak in carbon nanotubes, the current density distribution is spatially homogeneous, which is less likely to induce inhomogeneities in the potential surface of the trap. Moreover, they consist of a very small amount of dielectric matter which means that unwanted dispersion forces, such as the Casimir–Polder force, are minimized.

This Chapter is organized as follows. In Section 3.1 the basic concepts about carbon nanotubes and their conducting properties are introduced. In Section 3.2 the spin-flip lifetime for an atom near the outside of a metallic nanotube is calculated and compared to the limiting effect of the Casimir–Polder potential.

3.1 Carbon nanotubes

Carbon nanotubes are a one-atom thick two-dimansional structures that can be thought of as a hexagonal network of carbon atoms rolled up to make an extremely thin (seamless) cylinder, as schematically represented in Fig. 3.1. Each end of the cylinder is capped with half of a fullerene molecule which implies that the diameter of a nanotube can be as small as the fullerene molecule itself.

Interest from the research community first focused on electronic properties of carbon nanotubes. Those properties are due to the quantum confinement of electrons normal to the nanotube axis. In the radial direction the electrons are confined by the monolayer of the graphene sheet and they can only propagate along the nanotube axis.

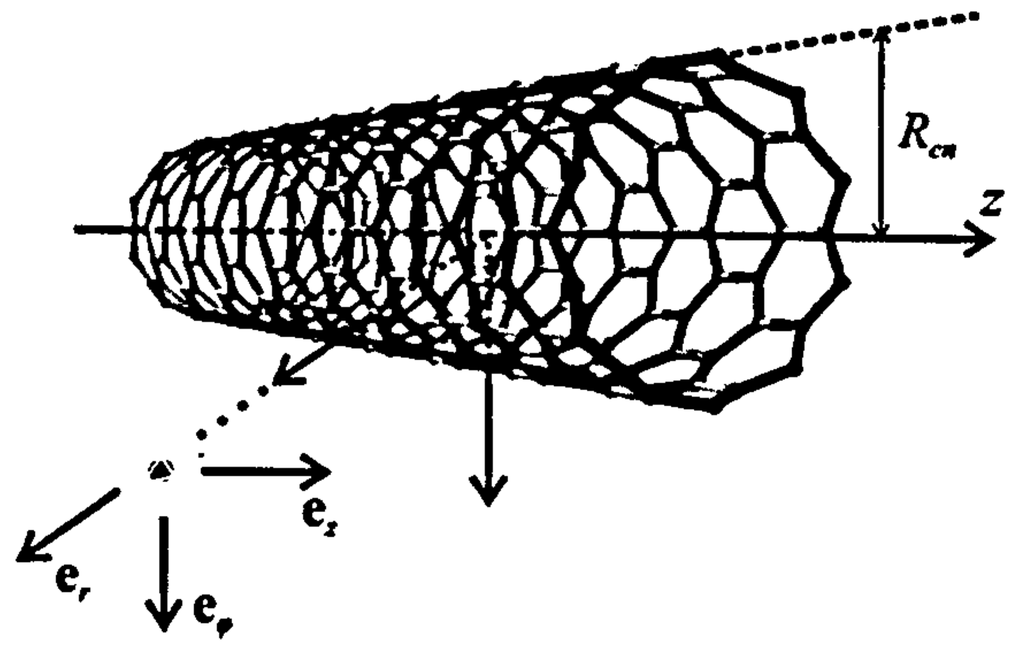

Figure 3.1: Schematic of the carbon nanotube geometry, taken from Ref. [129].

All carbon nanotubes derive their conduction and valence bands from those of a graphene sheet. A CN can be metallic or semiconducting with its electrical properties determined by the way the graphene sheet is rolled. Nanotubes rolled in different ways, or with a different chirality, exhibit different electronic band structures. A lattice vector between two hexagons is usually defined as $\mathbf{R}_{a,b} = a\mathbf{x} + b\mathbf{y}$ where a and b are integer numbers and $\mathbf{x}$ and $\mathbf{y}$ are the unit vectors of the two-dimensional graphene lattice as shown in Fig. 3.2. The vector $\mathbf{R}_{a,b}$ defines a periodic condition by connecting two graphene points that one identifies in order to create a nanotube. Depending on a and b, carbon nanotubes are either semiconducting or metallic and in the following the tubule index (a, b) is adopted. In particular, a CN exhibits metallic properties when $2a + b = 3n$, where n is again an integer [130–133]. An (a, b) carbon nanotube has one-dimensional electronic band [130]

$$E_{\pm}(N,p) = \pm t_0 \sqrt{1 + 4\cos\left(\frac{2\pi N}{a} - \frac{a+2b}{2a}p\ell\right)\cos\frac{p\ell}{2} + 4\cos^2\frac{p\ell}{2}} \qquad (3.1)$$

where $\ell = 2.13$ Å is $\frac{3}{2}$ times the interatomic distance, $t_0 = 4.32 \times 10^{-19}$ J is the tunnelling energy of the electrons along the lattice sites, $N = 0, 1, \ldots, a-1$, and $-\pi/\ell \leq p \leq \pi/\ell$ where p is the wave number of the first Brillouin zone. The plus and minus subscripts stand for the conduction and valence band, respectively.

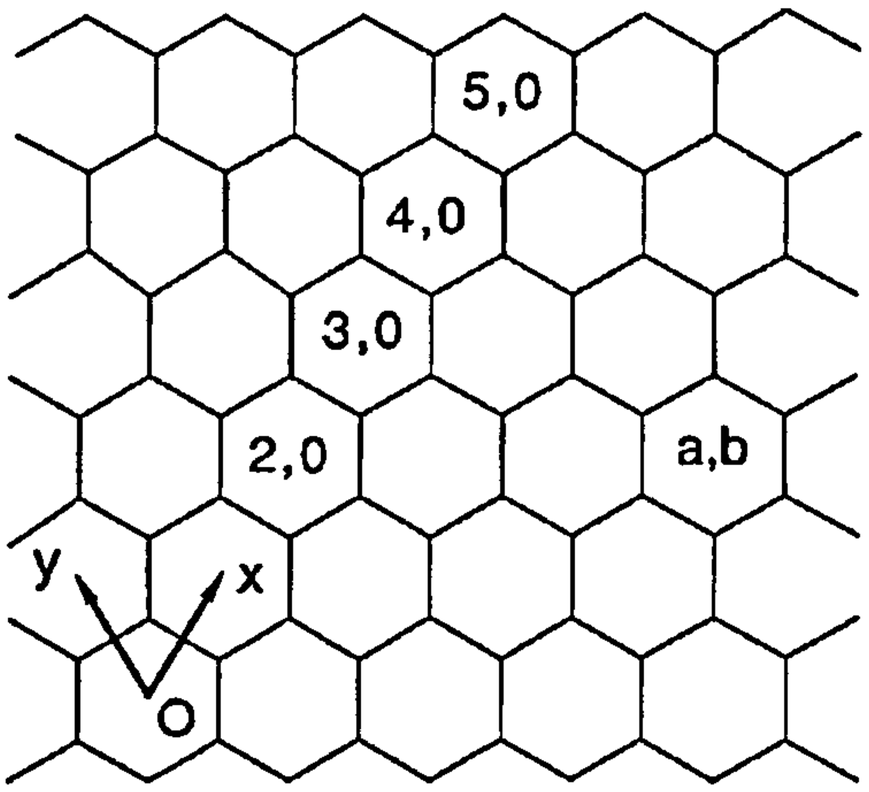

Figure 3.2: Parametrization of nanotubes, taken from Ref. [130]. Vectors **x** and **y** stand for the unit vectors of graphene lattice. The integer numbers a and b refers to the way the nanotube is rolled up. A nanotube (a, b) is formed by rolling the graphene sheet such that the hexagon O is overlapped with the hexagon (a, b).

In order to address the interaction between an atom and the vacuum electromagnetic field in the vicinity of a carbon nanotube, the electrodynamical properties of a CN need to be considered [129]. The electromagnetic response of a single CN can be modeled through effective boundary conditions by replacing the real nanotube with an infinitely thin cylindrical surface [134]. Optical processes such as absorption and diffraction are well described by the dielectric function $\varepsilon(\omega)$. For a linear dielectric medium, the relation between $\sigma(\omega)$ and $\varepsilon(\omega)$ is given by [127,135]

$$\frac{\varepsilon(\omega)}{\varepsilon_0} - 1 = i\frac{\sigma(\omega)}{\omega\varepsilon_0}, \tag{3.2}$$

where $\varepsilon_r(\omega) = \varepsilon(\omega)/\varepsilon_0$ is the (complex) relative dielectric permittivity. Because of the cylindrical structure of CNs, the polarization of the electromagnetic field is parallel to the nanotube axis [130, 136–139]. The azimuthal current can be neglected and the axial conductivity per unit length can be expressed as [129,130]

$$\sigma_{zz}(\mathbf{R},\omega) = -\frac{i\omega\varepsilon_0}{S}\frac{\varepsilon_r(\mathbf{R},\omega)-1}{\rho_T} \tag{3.3}$$

where $\mathbf{R} = (\mathrm{R_{CN}}, \phi, Z)$ is the radius vector of an arbitrary point on the CN surface, S is the cross-sectional area of a single nanotube, ρ_T is the tubule density and $\varepsilon_r \equiv \varepsilon_r^{zz}$ is the axial component of the permittivity tensor. The relative dielectric permittivity is then given by [130]

$$\varepsilon_r(\omega) = \varepsilon_r^d(\omega) + \varepsilon_r^b(\omega), \tag{3.4}$$

where $\varepsilon_r^d(\omega)$ is the dynamic conductivity due to the free carrier and represents the main contribution to the conductivity. For high frequency regimes, transitions between the conduction and the valence bands take place and an additional contribution $\varepsilon_r^b(\omega)$ needs to be considered. A detailed calculation of the permittivity is presented in Appendix A.

Unit conversion

For the sake of completeness, it is worth pointing out here that almost the totality of the work cited in this Section and in Appendix A adopts Gaussian units. The transition from Gaussian units to SI units is straightforward, but attention is required when calculating the axial conductivity. The axial conductivity (per unit length) in Gaussian units reads [129, 130]

$$\sigma_{zz}(\mathbf{R}, \omega) = -i\omega \frac{\varepsilon_r(\mathbf{R}, \omega) - 1}{4\pi S \rho_T}. \tag{3.5}$$

To obtain the conductivity per unit length in SI units, as plotted in Fig. A.1, it is then sufficient to multiply Eq. (3.5) by a factor $1/(4\pi\varepsilon_0) = 10^{-7}c^2$. Analogous attention needs to be taken when obtaining effective boundary conditions for CNs.

3.1.1 Green tensor of a single wall carbon nanotube

This Section shows how to obtain the dyadic Green tensor for a single-wall CN together with the corresponding boundary conditions for the electromagnetic field on its surface. For a single-wall nanotube, the carbon layer can be approximated

by a layer with zero thickness. The Green tensor will then be discontinuous in its first spatial derivative across the carbon layer.

Due to the cylindrical symmetry, the problem can be described adopting the cylindrical basis $\{\mathbf{e}_r, \mathbf{e}_\varphi, \mathbf{e}_z\}$ with the CN directed along $\mathbf{e}_z$. The method of scattering superposition is used (see, e.g. [140,141]). For an atom located at $\mathbf{r}'$ outside the CN, the Green tensor can be written as

$$\boldsymbol{G}(\mathbf{r},\mathbf{r}',\omega) = \begin{cases} \boldsymbol{G}_0(\mathbf{r},\mathbf{r}',\omega) + \boldsymbol{G}_R^{(S)}(\mathbf{r},\mathbf{r}',\omega), & r > R_{CN}, \\ \boldsymbol{G}_T^{(S)}(\mathbf{r},\mathbf{r}',\omega), & r < R_{CN}, \end{cases} \tag{3.6}$$

where $\boldsymbol{G}_0(\mathbf{r},\mathbf{r}',\omega)$ is the unbounded Green tensor representing the contribution of direct waves from a source at $\mathbf{r}'$ to the point $\mathbf{r}$. The two scattering contributions $\boldsymbol{G}_R^{(S)}(\mathbf{r},\mathbf{r}',\omega)$ and $\boldsymbol{G}_T^{(S)}(\mathbf{r},\mathbf{r}',\omega)$ describe the reflection and transmission of waves from/through the cylindrical surface. In order to satisfy the homogeneous Helmholtz equation and the radiation condition at infinity, the vacuum term and the two scattering terms are written as [141]

$$\begin{aligned} \boldsymbol{G}_0(\mathbf{r},\mathbf{r}',\omega) &= -\frac{\hat{\mathbf{r}}\hat{\mathbf{r}}\delta(\mathbf{r}-\mathbf{r}')}{k^2} + \frac{i}{8\pi}\int_{-\infty}^{\infty} dh \sum_{n=0}^{\infty} \frac{2-\delta_{n0}}{\eta^2} \\ &\times \begin{cases} \mathbf{M}_{\substack{e\\o}n}^{(1)}(h)\mathbf{M}'_{\substack{e\\o}n}(-h) + \mathbf{N}_{\substack{e\\o}n}^{(1)}(h)\mathbf{N}'_{\substack{e\\o}n}(-h) & r > r', \\ \mathbf{M}_{\substack{e\\o}n}(h)\mathbf{M}_{\substack{e\\o}n}^{\prime(1)}(-h) + \mathbf{N}_{\substack{e\\o}n}(h)\mathbf{N}_{\substack{e\\o}n}^{\prime(1)}(-h) & r < r', \end{cases} \end{aligned} \tag{3.7}$$

$$\begin{aligned} \boldsymbol{G}_R^{(S)}(\mathbf{r},\mathbf{r}',\omega) &= \frac{i}{8\pi}\int_{-\infty}^{\infty} dh \sum_{n=0}^{\infty} \frac{2-\delta_{n0}}{\eta^2} \\ &\times \left\{ \left[C_{1H}\mathbf{M}_{\substack{e\\o}n}^{(1)}(h) + C_{2H}\mathbf{N}_{\substack{o\\e}n}^{(1)}(h) \right] \mathbf{M}_{\substack{e\\o}n}^{\prime(1)}(-h) \right. \\ &\left. + \left[C_{1V}\mathbf{N}_{\substack{e\\o}n}^{(1)}(h) + C_{2V}\mathbf{M}_{\substack{o\\e}n}^{(1)}(h) \right] \mathbf{N}_{\substack{e\\o}n}^{\prime(1)}(-h) \right\}, \end{aligned} \tag{3.8}$$

$$
\begin{aligned}
\boldsymbol{G}_T^{(S)}(\mathbf{r},\mathbf{r}',\omega) &= \frac{i}{8\pi}\int_{-\infty}^{\infty} dh \sum_{n=0}^{\infty} \frac{2-\delta_{n0}}{\eta^2} \\
&\times \Big\{ \left[\mathcal{C}_{3H}\mathbf{M}_{\substack{e\\o}n}(h) + \mathcal{C}_{4H}\mathbf{N}_{\substack{o\\e}n}(h)\right] \mathbf{M}'^{(1)}_{\substack{e\\o}n}(-h) \\
&\quad + \left[\mathcal{C}_{3V}\mathbf{N}_{\substack{e\\o}n}(h) + \mathcal{C}_{4V}\mathbf{M}_{\substack{o\\e}n}(h)\right] \mathbf{N}'^{(1)}_{\substack{e\\o}n}(-h) \Big\} ,
\end{aligned} \tag{3.9}
$$

where $k = \omega/c$ and $\eta^2 = k^2 - h^2$. To enhance readability, the tensor product symbol $\otimes$ has been omitted between the even (e) and the odd (o) cylindrical vector wave functions which are defined as

$$
\mathbf{M}_{\substack{e\\o}n}(h) = \boldsymbol{\nabla} \times \left[Z_n(\eta r) \begin{pmatrix} \cos \\ \sin \end{pmatrix} n\phi \, e^{ihz} \mathbf{e}_z \right], \tag{3.10}
$$

$$
\mathbf{N}_{\substack{e\\o}n}(h) = \frac{1}{k}\boldsymbol{\nabla} \times \boldsymbol{\nabla} \times \left[Z_n(\eta r) \begin{pmatrix} \cos \\ \sin \end{pmatrix} n\phi \, e^{ihz} \mathbf{e}_z \right] . \tag{3.11}
$$

The symbol $Z_n(x)$ has to be replaced either by the Bessel function $J_n(x)$ or, if the superscript (1) appears on the respective vector wave function, by the (outgoing) Hankel function of the first kind $H_n^{(1)}(x)$. The primes in Eqs. (3.7)-(3.9) indicate the cylindrical coordinates (r', ϕ', z'). The coefficients $\mathcal{C}_{mP}$ ($m = 1$, 2, 3 and 4, and $P = H$, V) need to be determined from the boundary conditions for the electric and magnetic field components on the CN surface.

In order to fulfill the boundary conditions, the density of the electric surface current is assumed to be evenly distributed throughout the nanotube surface such that it can be considered as a continous current sheet. Ohm's law on the nanotube surface may be written as

$$
\mathbf{J}(\mathbf{r}) = \boldsymbol{\sigma}(\mathbf{r}) \cdot \mathbf{E}(\mathbf{r}), \tag{3.12}
$$

where $\boldsymbol{\sigma}(\mathbf{r})$ is the (diagonal) conductivity tensor whose only non-zero element is $\sigma_{zz}(\mathbf{R}, \omega)$. As no magnetic current density is excited on the surface, the electric field satisfies the boundary condition

$$
\mathbf{e}_r \times \left[\mathbf{E}(\mathbf{r},\omega)\big|_{r=R_{\mathrm{CN}}^+} - \mathbf{E}(\mathbf{r},\omega)\big|_{r=R_{\mathrm{CN}}^-} \right] = 0, \tag{3.13}
$$

while the electric surface current density creates a discontinuity in the tangential component of the magnetic field

$$\mathbf{e}_r \times \left[\mathbf{H}(\mathbf{r},\omega)\big|_{r=R_{\mathrm{CN}}^+} - \mathbf{H}(\mathbf{r},\omega)\big|_{r=R_{\mathrm{CN}}^-}\right] = \mathbf{J}(\mathbf{r},\omega)|_{r=R_{\mathrm{CN}}}. \tag{3.14}$$

Equations (3.13)-(3.14) translate into the respective boundary conditions for the Green tensor

$$\mathbf{e}_r \times \left[\boldsymbol{G}(\mathbf{r},\mathbf{r}',\omega)\big|_{r=R_{\mathrm{CN}}^+} - \boldsymbol{G}(\mathbf{r},\mathbf{r}',\omega)\big|_{r=R_{\mathrm{CN}}^-}\right] = 0, \tag{3.15}$$

$$\begin{aligned}\mathbf{e}_r \times \boldsymbol{\nabla} \times &\left[\boldsymbol{G}(\mathbf{r},\mathbf{r}',\omega)\big|_{r=R_{\mathrm{CN}}^+} - \boldsymbol{G}(\mathbf{r},\mathbf{r}',\omega)\big|_{r=R_{\mathrm{CN}}^-}\right] \\ &= i\omega\mu_0\boldsymbol{\sigma}(\mathbf{r})\cdot\boldsymbol{G}(\mathbf{r},\mathbf{r}',\omega)\big|_{r=R_{\mathrm{CN}}}.\end{aligned} \tag{3.16}$$

Substituting the decomposition (3.6), together with Eqs. (3.7)-(3.9), into the boundary conditions (3.15) and (3.16) leads to 16 linear equations grouped in two sets that enable the determination of the coefficients C_{mP}. Note that the presence of the symbols $\pm$ and $\mp$ is due to an opposite sign when the even and odd wave functions of Eqs. (3.10)-(3.11) are derived in order to satisfy the boundary conditions. The coefficients C_{mH} can be obtained from

$$-\frac{\eta^2}{k}H_n(\eta r)\mathcal{C}_{2H}+\frac{\eta^2}{k}J_n(\eta r)\mathcal{C}_{4H} = 0, \quad (3.17)$$

$$\begin{aligned}-\partial_r H_n(\eta r)\mathcal{C}_{1H} \pm \frac{ihn}{kr}H_n(\eta r)\mathcal{C}_{2H}\\ +\partial_r J_n(\eta r)\mathcal{C}_{3H} \mp \frac{ihn}{kr}J_n(\eta r)\mathcal{C}_{4H} &= \partial_r J_n(\eta r), \quad (3.18)\end{aligned}$$

$$-\eta^2 H_n(\eta r)\mathcal{C}_{1H}+\eta^2 J_n(\eta r)\mathcal{C}_{3H} = \eta^2 J_n(\eta r), \quad (3.19)$$

$$\begin{aligned}\mp\frac{ihn}{r}H_n(\eta r)\mathcal{C}_{1H}-k\partial_r H_n(\eta r)\mathcal{C}_{2H}\pm\frac{ihn}{r}J_n(\eta r)\mathcal{C}_{3H}\\ +\left(k\partial_r J_n(\eta r)-i\omega\mu_0\sigma_{zz}\frac{\eta^2}{k}J_n(\eta r)\right)\mathcal{C}_{4H} &= \pm\frac{ihn}{r}J_n(\eta r), \quad (3.20)\end{aligned}$$

while the coefficients $\mathcal{C}_{mV}$ can be obtained from

$$-\frac{\eta^2}{k}H_n(\eta r)\mathcal{C}_{1V}+\frac{\eta^2}{k}J_n(\eta r)\mathcal{C}_{3V} = \frac{\eta^2}{k}J_n(\eta r), \quad (3.21)$$

$$\begin{aligned}\mp\frac{ihn}{kr}H_n(\eta r)\mathcal{C}_{1V}-\partial_r H_n(\eta r)\mathcal{C}_{2V}\\ \pm\frac{ihn}{kr}J_n(\eta r)\mathcal{C}_{3V}+\partial_r J_n(\eta r)\mathcal{C}_{4V} &= \pm\frac{ihn}{kr}J_n(\eta r), \quad (3.22)\end{aligned}$$

$$-\eta^2 H_n(\eta r)\mathcal{C}_{2V}+\eta^2 J_n(\eta r)\mathcal{C}_{4V} = 0, \quad (3.23)$$

$$\begin{aligned}-k\partial_r H_n(\eta r)\mathcal{C}_{1V}\pm\frac{ihn}{r}H_n(\eta r)\mathcal{C}_{2V}\\ +\left(k\partial_r J_n(\eta r)-i\omega\mu_0\sigma_{zz}\frac{\eta^2}{k}J_n(\eta r)\right)\mathcal{C}_{3V}\\ \mp\frac{ihn}{r}J_n(\eta r)\mathcal{C}_{4V} &= k\partial_r J_n(\eta r). \quad (3.24)\end{aligned}$$

The appearance of the axial conductivity $\sigma_{zz}(\mathbf{R},\omega)$ in the boundary conditions

(3.20) and (3.24) reflect the jump condition (3.16) of the derivative of the Green tensor at the boundary layer.

The Green function needs to be computed in the region where the atom is located and only $C_{(1,2)P}$ has to be determined. On using various properties of the Bessel functions such as the Wronskian between the Bessel function $J_n(x)$ and the Hankel function $H_n^{(1)}(x)$,

$$J_n(x)H_n^{(1)\prime}(x) - J_n'(x)H_n^{(1)}(x) = \frac{2}{\pi x}, \tag{3.25}$$

the only non-zero coefficient is obtained as

$$C_{1V} = -\frac{\pi\mu_0\omega R_{\mathrm{CN}}\sigma_{zz}\eta^2 J_n^2(\eta R_{\mathrm{CN}})}{2k^2 + \pi\mu_0\omega R_{\mathrm{CN}}\sigma_{zz}\eta^2 J_n(\eta R_{\mathrm{CN}})H_n(\eta R_{\mathrm{CN}})}. \tag{3.26}$$

Finally, the Green tensor for an atom located at position $\mathbf{r}'$ outside the CN can be expressed as

$$\boldsymbol{G}(\mathbf{r},\mathbf{r}',\omega) = \boldsymbol{G}_0(\mathbf{r},\mathbf{r}',\omega) + \frac{i}{8\pi}\int_{-\infty}^{\infty} dh \sum_{n=0}^{\infty} \frac{2-\delta_{n0}}{\eta^2} C_{1V}\mathbf{N}_{\substack{e\\o}n}^{(1)}(h)\mathbf{N}_{\substack{e\\o}n}^{\prime(1)}(-h)\,. \tag{3.27}$$

Equation (3.27), together with Eq. (3.7), is the expression for the Green tensor used throughout this thesis for a single-wall carbon nanotube.

3.2 Trapping lifetimes

Due to the very small amount of matter constituting a carbon nanotube (compared to a dielectric bulk material), the noise originating from fluctuating electromagnetic fields near the surface is expected to decrease significantly. Nevertheless, thermal spin flips and the Casimir–Polder force cannot be neglected and their effects need to be both taken into account. The interplay of these two phenomena is analysed in this Section.

The calculations presented here are valid for a single-wall metallic carbon nan-

otube acting as a current carrying wire. In particular, the current sent through a (9,0) carbon nanotube is assumed to be $I = 20\,\mu$A, which seems to be the largest current that can be sustained before saturation effects become important [142]. The axial conductivity $\sigma_{zz}(\omega)$ and the resulting dielectric permittivity $\varepsilon(\omega)$ of a $(9,0)$ carbon nanotube are calculated in Appendix A. At a frequency $f_0 = 70$ kHz, chosen to correspond to an offset field $B_o = 10^{-5}\,\mathrm{T} = 100\,\mathrm{mG}$, the estimated values of axial conductivity and dielectric permittivity are $\sigma_{zz}(\omega_0) = 1.19 \cdot 10^9 + i\,11.5\ (\Omega\mathrm{m})^{-1}$ and $\varepsilon(\omega_0) \simeq 3 \cdot 10^{14}\,i$.

3.2.1 Spin-flip lifetime

The interaction of an atom with the carbon nanotube can be described within the framework of quantum electrodynamics in dispersing and absorbing bodies [76], as introduced in Chapter 2. This is a macroscopic theory whose central quantities are linear susceptibilities and macroscopic polarizabilities. Carbon nanotubes are probably at the limit to what can be described with in this framework. In addition, the use of macroscopic Green functions assumes that one can place boundary conditions on smooth surfaces and the application of QED in dielectric matter is correct if a CN may be considered as a mesoscopic object [129]. If an atom is placed far enough from the surface, say at distances that are several multiples of the bond lengths, the CN is seen as a homogeneous object by the probe atom so that the detailed structure from the surface cannot be resolved and QED in dielectrics can safely be used. This also assumes that the CN contains no impurities and shows no pitch alterations.

The lifetime of an atom due to spin-flip transitions is given by the inverse of the spin-flip rate [49]

$$\Gamma = \frac{2(\mu_B g_S)^2}{c^2 \varepsilon_0 \hbar} \langle f|\hat{S}_q|i\rangle \langle i|\hat{S}_k|f\rangle \mathrm{Im}\left[\overrightarrow{\nabla} \times \boldsymbol{G}(\mathbf{r},\mathbf{r},\omega_0) \times \overleftarrow{\nabla}\right]_{qk}, \tag{3.28}$$

where μ_B is the Bohr magneton, $\hat{S}_k$ is the kth vector component of the electronic

spin operator, and $g_S \approx 2$ the electron's g factor. Spin flips occur between the initial state $|i\rangle = |2,2\rangle$ and the final state $|f\rangle = |2,1\rangle$. The position $\mathbf{r}$ of the atom is taken to be at the centre of the trap which, in the harmonic approximation, is the average position of the atom and also the minimum of the trap.

The spin-flip rate in Eq. (3.28) is given in terms of the dyadic Green tensor $\boldsymbol{G}(\mathbf{r},\mathbf{r},\omega)$ which contains the physical and geometrical information about the nanotube. If the CN is in thermal equilibrium with the environment at a temperature T, the total spin-flip rate is given by $\Gamma_{\rm tot} = \Gamma(\bar{n}_{\rm th}+1)$ where $\bar{n}_{\rm th}$ is the mean thermal occupation number given in Eq. (1.35). In Fig. 3.3 the spin-flip lifetime $\tau_{SF} = 1/\Gamma_{\rm tot}$ is plotted as a function of the trapping distance y_0 for a temperature $T = 380$ K, corresponding to a thermal excitation energy of $k_B T = 5.2\,10^{-21}$ J ($\simeq 33$ meV). At the transition frequency $f_0 = \omega_0/2\pi = 70$ kHz, the thermally-induced spin flips dominate the spontaneous spin flips because $\hbar\omega_0 = 4.8\,10^{-29}$ J ($\simeq 0.3$ neV) $\ll k_B T$.

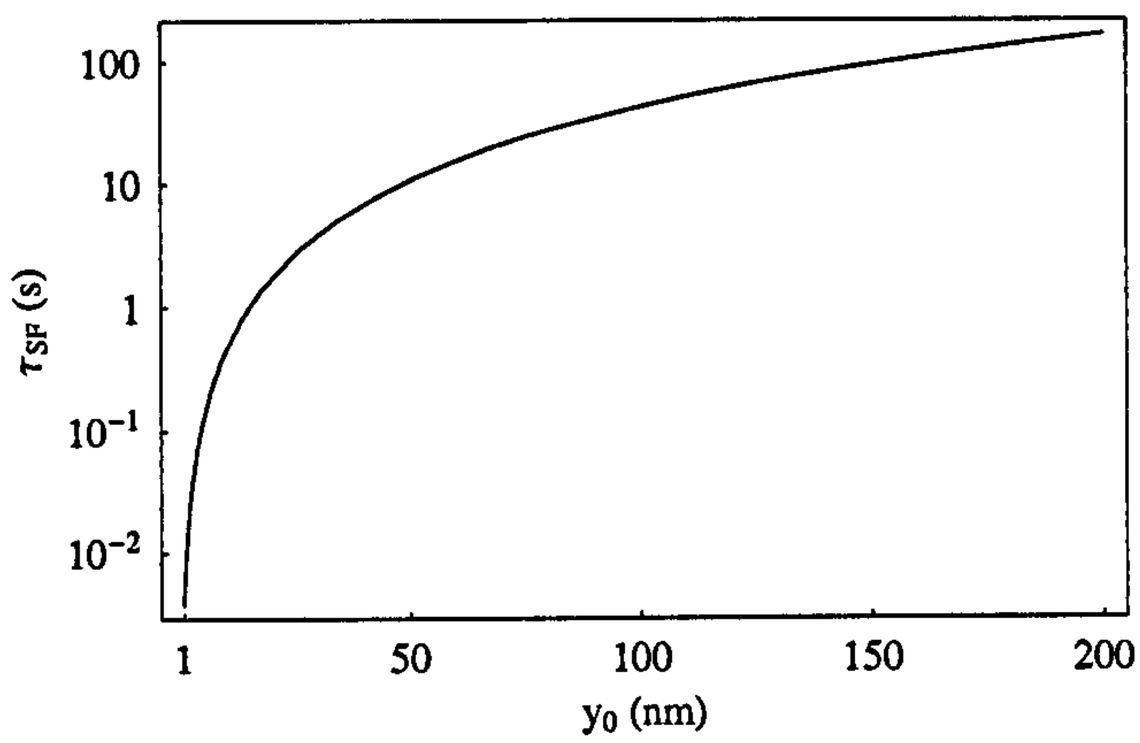

Figure 3.3: Spin-flip lifetime of a rubidium atom near a $(9,0)$ carbon nanotube with radius $R_{CN} = 3.52$ Å. The trapping distance y_0 is varied between 1 and 200 nm. The other parameters are: $f_0 = 70$ kHz and $T = 380$ K.

The lifetime increases with the atom-surface distance y_0 and is in agreement with the behaviour encountered in [49] for a solid wire. According to Fig. 3.3, at atom-surface distances above 20 nm, a lifetime of the order of a few seconds is

achievable. The spin-flip lifetime can reach one minute for distances approaching 120 nm and exceeds more than 100 s for trapping distances larger than 160 nm. These results suggest that an atom can be held very close to a metallic CN for sufficiently long times, which is in line with the expectations on spin-flip occurrence and the atom-loss rate estimations presented in [81].

3.2.2 The Casimir–Polder potential

The presence of macroscopic dielectric bodies changes drastically the structure of the vacuum electromagnetic field. One consequence is that an atom in its ground state placed sufficiently close to a dielectric body experiences a non-vanishing, in general attractive, dispersion force, the Casimir–Polder (CP) force [10–17]. Since the CP potential is added to the (repulsive) trapping potential, atoms can tunnel through the potential barrier and get stuck at the nanotube surface. The lifetime calculated in Sec. 3.2.1 provides information about the distance at which an atom can be held before thermally-driven spin flips occur in a given time, but the Casimir–Polder force may play an even bigger role for small enough distances.

The Casimir–Polder potential can be derived in lowest-order perturbation theory within the framework of QED in dielectric media [16]. For an atom in an energy eigenstate $|l\rangle$, the CP potential is given by the body-induced — i.e. dependent on the quantity of material— (and position-dependent) shift of the eigenvalue ΔE_l. The CP potential can be expressed as [14, 16]

$$U(\mathbf{r}) = \frac{\hbar\mu_0}{2\pi}\int_0^\infty du\, u^2\alpha(iu)\mathrm{Tr}[\boldsymbol{G}^{(S)}(\mathbf{r},\mathbf{r},iu)], \tag{3.29}$$

where $iu = \omega$ and $\alpha(\omega)$ is the atomic polarizability in lowest-order perturbation theory. In particular, for an atom in a spherically symmetric ground state as in the case considered here, one finds that

$$\alpha(\omega) = \lim_{\xi\to 0}\frac{2}{3\hbar}\sum_k \frac{\omega_{kl}}{\omega_{kl}^2-\omega^2-i\omega\xi}|\mathbf{d}_{lk}|^2 \tag{3.30}$$

with $\mathbf{d}_{lk} = \langle l|\hat{\mathbf{d}}|k\rangle$ representing the matrix dipole elements relative to the transition from the atomic initial state $|l\rangle$ to the allowed states $|k\rangle$ with frequency $\omega_{kl} \equiv (E_k - E_l)/\hbar$. The expression of the CP potential in Eq. (3.29) is given in terms of the scattering part $\boldsymbol{G}^{(S)}(\mathbf{r}, \mathbf{r}, iu)$ of the Green tensor and the frequency integral is performed along the imaginary axis. The Casimir–Polder potential has to be compared with the magnetic trapping potential in order to establish the impact of its effect.

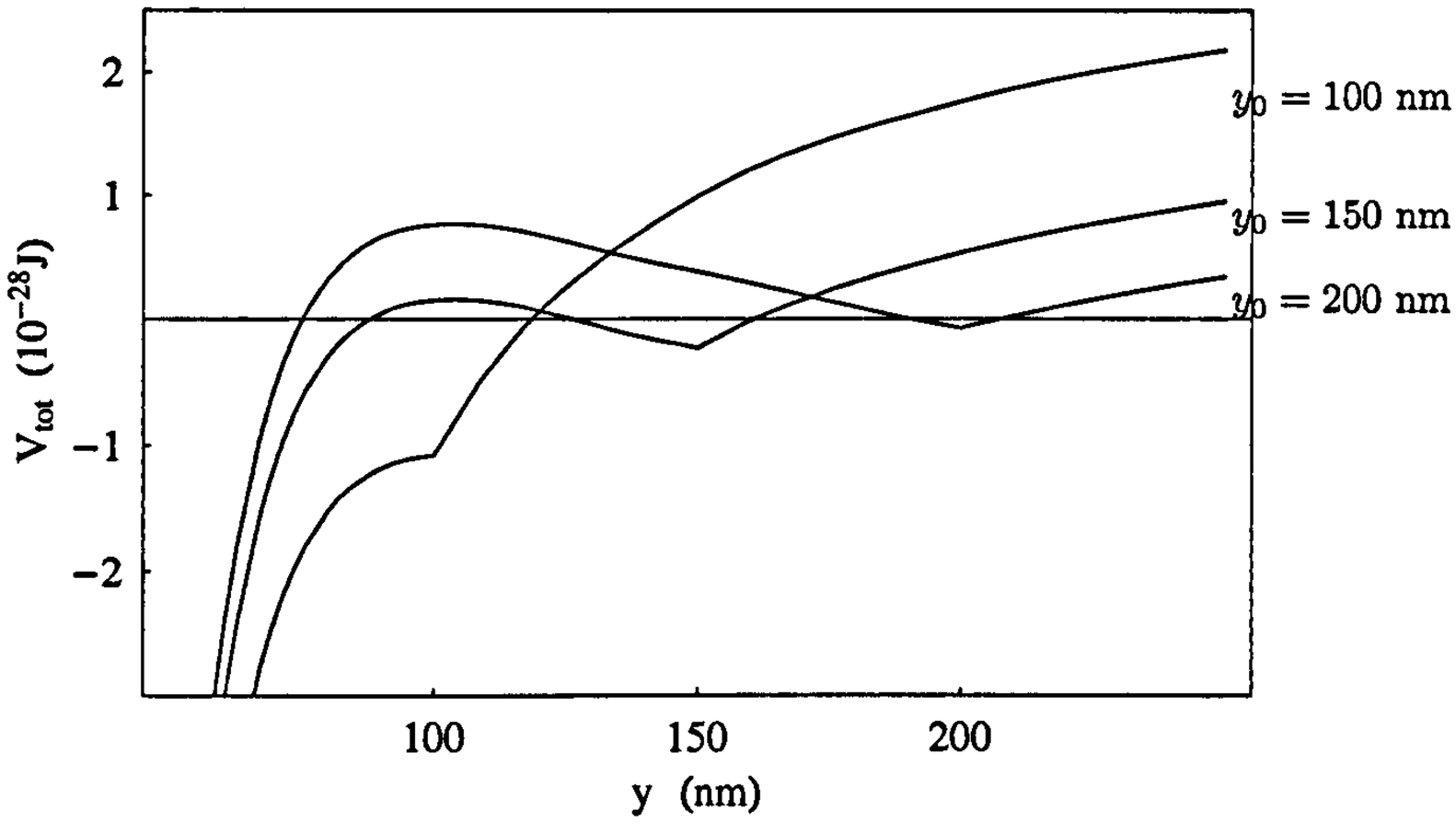

Figure 3.4: Plot of the potential V_{tot} given by the sum of the Casimir–Polder potential of Eq. (3.29) and the magnetic trapping potential of Eq. (1.3). The three lines corresponds to three trapping distances $y_0 = 100$ nm, 150 nm, and 200 nm, with a $20\,\mu$A current and a spin-flip transition frequency of $f_0 = 70$ kHz.

The total potential V_{tot} given by the sum of the two potentials of Eq. (1.3) and Eq. (3.29) is plotted in Fig. 3.4 for three different trapping distances $y_0 =$ 100 nm, 150 nm, and 200 nm, considering again a $20\,\mu$A current flowing through the CN. Among all the possible transitions $|l\rangle \rightarrow |k\rangle$, the only one taken into consideration is the lowest electronic transition $\mathrm{D_2}\,(5^2\mathrm{S}_{1/2} \rightarrow 5^2\mathrm{P}_{3/2})$ with frequency $\omega_2 \simeq 2\pi$ 384 THz and dipole moment $|\mathbf{d_2}| = 4.227\,ea_0$ [a_0: Bohr radius]. In contrast to the spin-flip lifetime, temperature effects are negligible because $\hbar c/\lambda = 4\,10^{-20}$ J ($\simeq$ 0.2 eV) $\gg k_B T$ which means that the resonant contri-

butions [143] are suppressed. The transition D_1 ($5^2S_{1/2} \rightarrow 5^2P_{1/2}$) with frequency $\omega_1 \simeq 2\pi$ 377 THz and dipole moment $|\mathbf{d}_1| = 2.992\, ea_0$ has not been included in the calculations presented here. Its contribution to the atomic polarizability is smaller than the one from the D_2 transition although not exactly negligible. The order of magnitude of the two contributions is the same which means that the atomic polarizability would have the same order of magnitude as well and this does not affect too much the comparison between the Casimir-Polder potential and the magnetic trapping potential. Thus the results obtained here can be safely regarded as good estimates.

As it is evident from Fig. 3.4, V_{tot} forms a potential barrier whose height and width vary with the trapping distance y_0. As previously mentioned, the addition of the offset field $\mathbf{B}_o$ changes the bottom of the potential well from a linear to a harmonic trap which is, however, not visible on the scale of the figure. When y_0 decreases, the potential barrier becomes more and more shallow, until for atom-surface distances smaller than the critical value of $y_0 \simeq 100$ nm, the barrier effectively disappears and the minimum becomes a saddle point. For trapping distances larger than that, the total potential shows a pronounced minimum. For example, for $y_0 = 150$ nm the trap oscillation frequency is estimated here to be $\omega_r \simeq 0.7$ kHz, and the width and the height of the potential barrier are 68.6 nm and $3.8 \cdot 10^{-29}$ J, respectively.

The WKB approximation allows the estimation of the transmission coefficient T through a barrier of variable potential $V(x)$ as

$$T \simeq e^{-2\gamma}, \quad \gamma = \frac{1}{\hbar} \int_0^a dx \sqrt{2m[V(x) - E]} \tag{3.31}$$

where $V(x)$ in this case is V_{tot}, given by the sum of the Casimir-Polder potential and the trapping magnetic potential, a is the width of the potential barrier and E the energy of the trapped atom depending on the trapping distance y_0. The corresponding tunnelling lifetime is then $\tau_{CP} = 2\pi/(T\omega_r(y_0))$. The result is shown

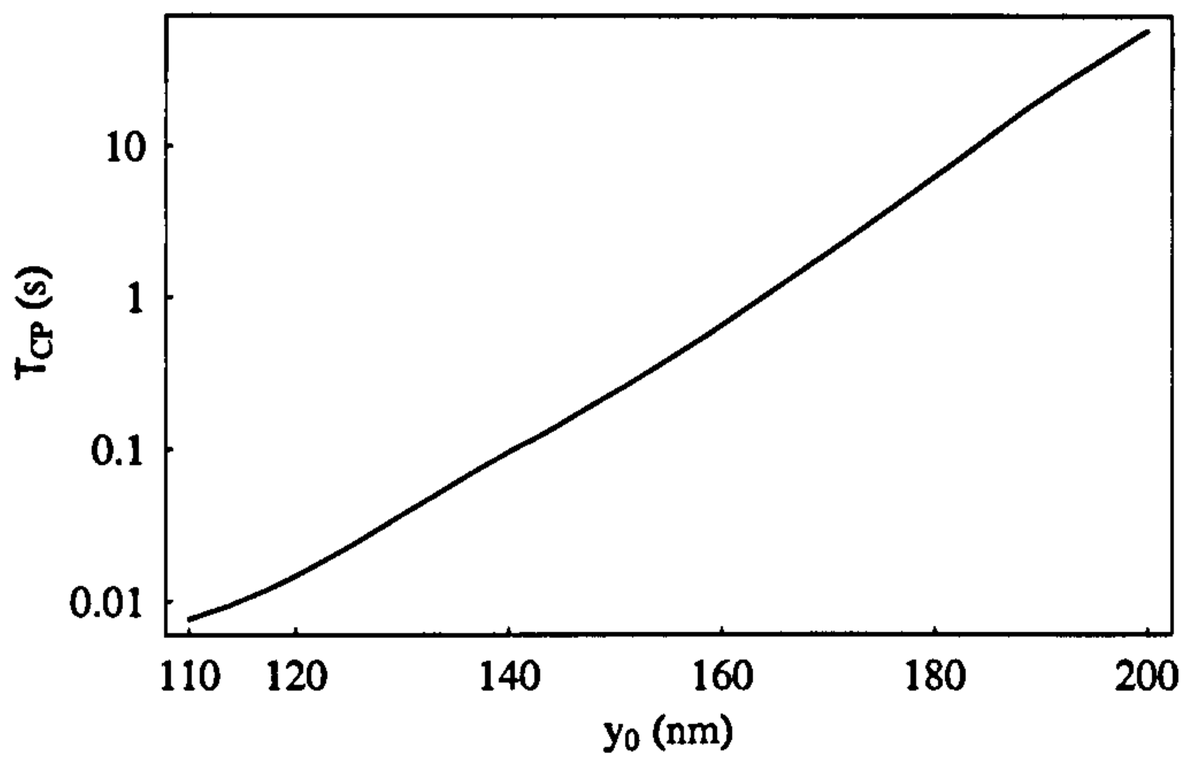

Figure 3.5: Tunneling lifetime τ_{CP} as a function of the trapping distance y_0.

in Fig. 3.5 for a ground-state atom trapped at varying distances y_0. From the comparison of Fig. 3.3 and Fig. 3.5, it is clear that the effect of the CP force cannot be neglected. For small enough atom-nanotube distances (and indeed for all distances shown in the figures) the tunnelling lifetime is several orders of magnitude smaller than the spin-flip lifetime. For example, at a trapping distance $y_0 = 150$ nm τ_{SF} and τ_{CP} are estimated to be 94.4 s and 0.2 s, respectively and a tunnelling lifetime of a few seconds is achievable for trapping distances equal or bigger than 170 nm where the spin flip occurrence is no longer a limiting factor.

3.2.3 Bound states

Atoms magnetically confined near a wire are often trapped in metastable states and indeed atoms in the trap suggested here occupy resonance states and have no true bound states, see for example [97,144,145]. However, for large enough values of the offset field the decay rate becomes so small that the resonances can be regarded as stable. For example, for a bias field of 0.3 G, the expected resonance lifetime exceeds two hours as pointed out in [145].

This may raise the question of whether there are any bound states below the trapping distance y_0. Those states would be located close to the carbon nanotube

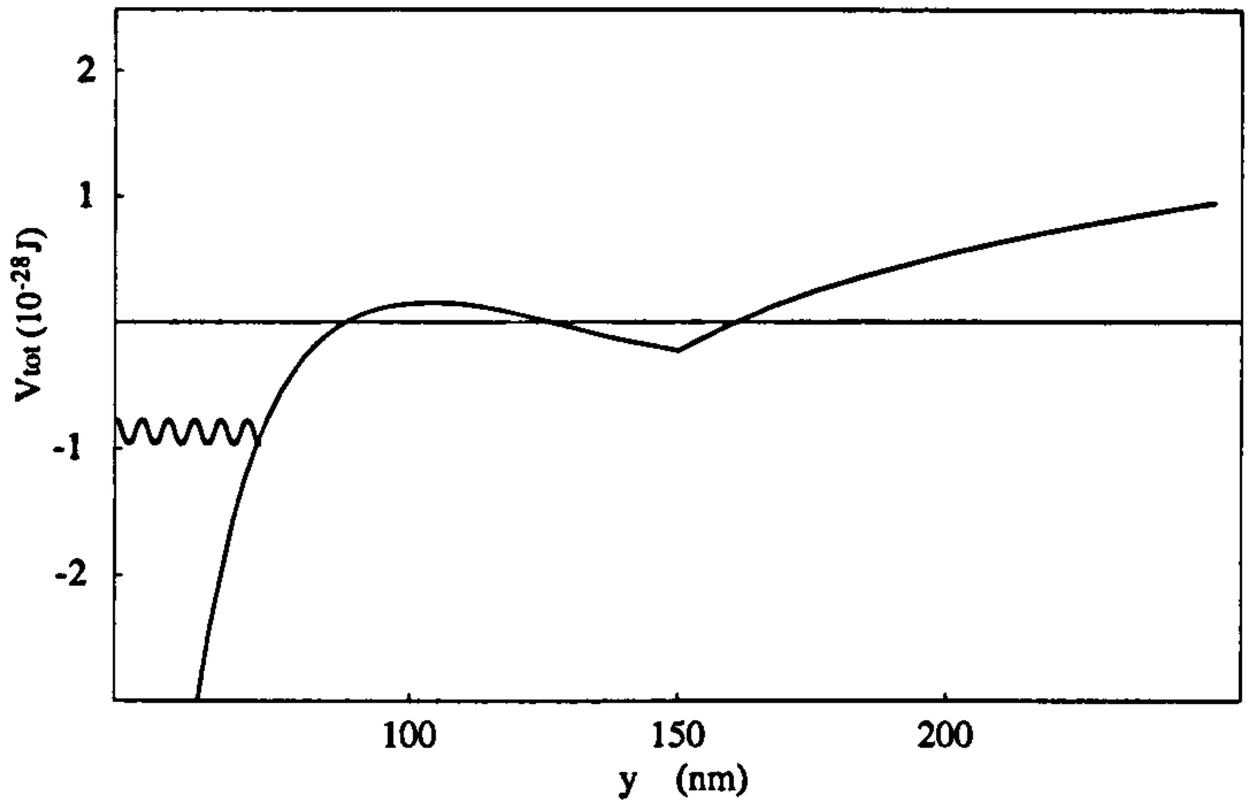

Figure 3.6: Schematic representation of the confining potential for a distance $y_0 = 150\,\mu$m from the nanotube surface The wavy line represents a bound state, note that the position is totally arbitrary.

surface such that they would see a delta potential $\delta(0)$ for the surface and the Casimir-Polder potential V_{CP}, as schematically illustrated in Fig. 3.6. If such a state exists, it must have an energy lower that the trapping energy at y_0. For simplicity, it is assumed that the atom experiences only the Casimir-Polder potential as the magnetic trapping potential is several orders of magnitude smaller for the distances considered. The energy of the first bound state can be found by solving a radial Schrödinger equation for the cylindrical Casimir-Polder potential

$$\left[-\frac{1}{r}\frac{\partial}{\partial r}\left(r\frac{\partial}{\partial r}\right) - \frac{1}{r^2}\frac{\partial^2}{\partial \phi^2} + \frac{2m}{\hbar^2}(V_{CP}(r) - E)\right]\psi(r,\phi) = 0. \tag{3.32}$$

The atom's wavefunction can be separated in an azimuthal and a radial part because of the cylindrical symmetries of the potential V_{CP}

$$\psi(r,\phi) = u_l(r)e^{il\phi}, \tag{3.33}$$

such that Eq. (3.32) becomes one-dimensional and can be rewritten as

$$\left[\frac{1}{r}\frac{\partial}{\partial r}\left(r\frac{\partial}{\partial r}\right) - \frac{l^2}{r^2} + \frac{2m}{\hbar^2}\left(\frac{C_3}{r^3} + E\right)\right] u_l(r) = 0. \tag{3.34}$$

In order to solve Eq. (3.34), it may be useful to express the Casimir-Polder

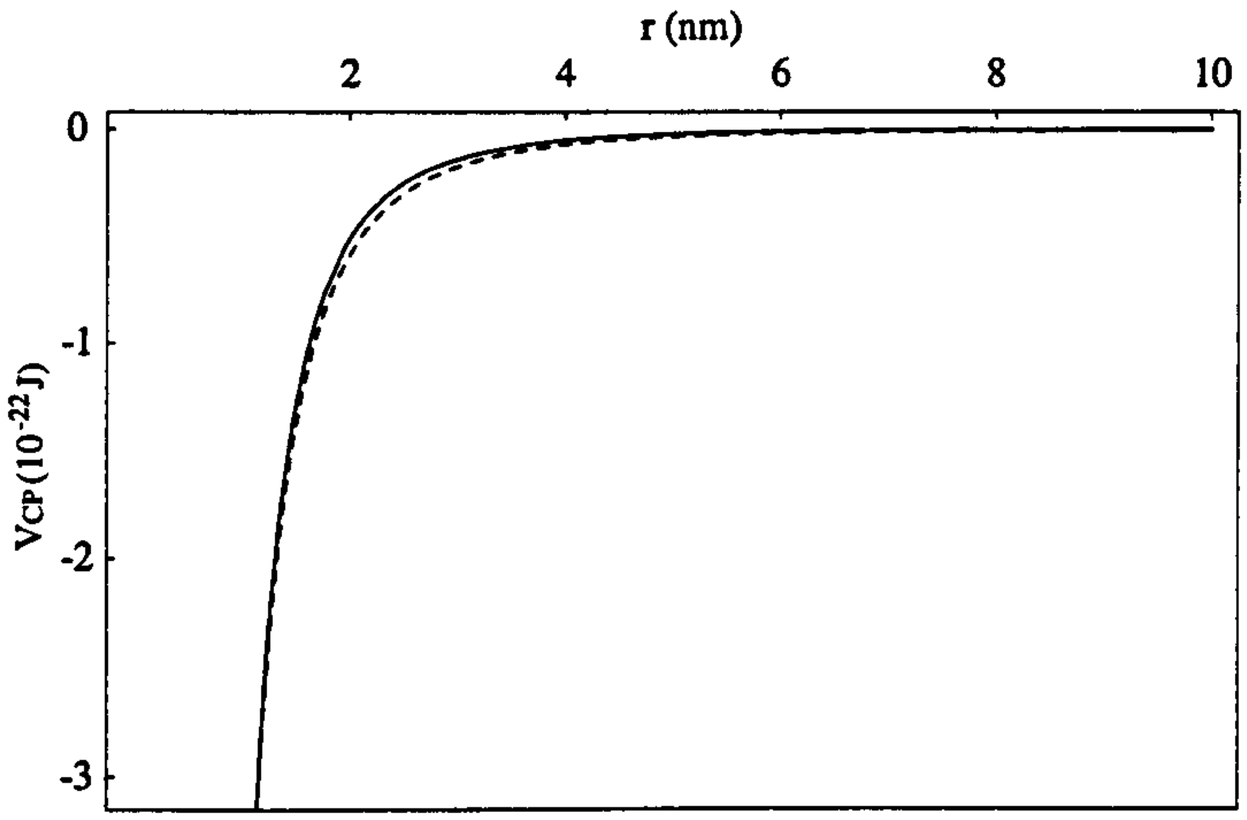

Figure 3.7: Casimir-Polder potential (solid line), and numerical interpolation (dotted line) according to a power law $-C_3/r^3$ with $C_3 = 4.6\,10^{-49}$ J m^{-3}.

potential as a function of the distance r

$$V_{CP}(r) = -\alpha r^{-s} \quad (\alpha > 0). \tag{3.35}$$

In agreement with the results presented in [146], the best power law given by numerical interpolation for the distance dependence is found to be r^{-3} as showed in Fig. 3.7

$$V_{CP}(r) = -\frac{C_3}{r^3}, \tag{3.36}$$

with $C_3 = 4.6\,10^{-49}$ J m^{-3}.

The solution to the differential equation (3.34) is likely to be a combination of Hankel functions (spherical Bessel functions) but no analytical solution exists. Before looking for numerical solutions, it is worth attempting an estimation of

the energy of the first bound state. Among all the attractive potentials with r^{-s} dependence, the ones with $s = 2$ lie on the border between atomic radial motions that can be stabilized by angular momentum ($s < 2$) [147] and those where the stabilization is not possible, in principle ($s > 2$) [148]. This behaviour can be understood by considering a wave function that is finite in some small region of radius r_0 around the origin. If the uncertainty in the position of a particle in this wave packet is of the order of r_0, the uncertainty in its momentum is then $\simeq \hbar/r_0$ which corresponds to an average energy $\hbar^2/mr_0^2$. An atom experiencing the Casimir-Polder potential has a mean potential energy of $\simeq C_3/r_0^3$. One can assume that the atom has an initial potential energy equal to 0, and that it gains kinetic energy $\hbar^2/mr_0^2$ as it rolls down the potential losing part of its potential energy C_3/r_0^3. A stable radial motion would have

$$\frac{\hbar^2}{mr_0^2} - \frac{C_3}{r_0^3} \approx 0, \tag{3.37}$$

which, for the value of C_3 obtained here numerically, corresponds to a wavepacket spread of the order of 600 nm. This wavelength is too big to allow for an atom to be in a bound state. Hence, no bound states exist apart from those confined by the local minimum of the magnetic trap.

3.3 Summary

In summary, a novel way of miniaturizing atomic magnetic traps has been addressed by considering carbon nanotubes. Their small diameter and the small amount of matter they are made of allow the magnetic confinement of atoms in the close proximity of the surface. The major loss mechanisms, such as thermally induce spin flips and the tunnelling through the Casimir-Polder barrier, have been investigated.

Very promising spin-flip lifetimes have been obtained for distances of the order of a few radiuses of the carbon nanotube. However, the alterations of the trapping

potential due to the Casimir-Polder interaction are much more severe than the limitations due to the thermally-induced spin flips. It appears that the minimal feasible trapping distance is larger than 100 nm. The main reason for this limitation is the fact that single-wall carbon nanotubes cannot sustain high enough currents because of saturation effects, leading to shallower magnetic traps. It may be beneficial to consider multi-wall carbon nanotubes as an increased number of layers allows higher current densities and so tighter trapping potentials.

The effect of the temperature has been considered for the two interactions. The magnetic transition frequency is typically in the kHz-MHz range which means that the mean thermal occupation number at room temperature is very large. On the other hand, optical frequencies are relevant in the Casimir-Polder interaction such that the mean thermal photon number is almost zero.

Finally, atoms confined according to the trap presented here occupy resonance states and have no true bound states. However, the expected resonance lifetimes are rather long for large enough values of the offset field. The possibility of having bound states at distances closer to the surface, i.e. between the surface and the Casimir-Polder potential, has been taken into consideration. Estimations of the energy of the first bound state have been given by approximating the Casimir-Polder potential with a power law $1/r^3$. They show that the wavelength associated to such a state would be too big, hence, suggesting that no bound state exists between the carbon nanotube surface and the Casimir-Polder potential.

4

Spatial decoherence near metallic surfaces

Decoherence occurs when a quantum system interacts with its environment such that the quantum superpositions of the system are destroyed and macroscopic classical features emerge. The preparation, manipulation and measurement of the quantum state of a physical system requires robust quantum control over the system itself and the loss of coherence due to its interaction with the environment is often a matter of concern. For example, control over the coherent evolution of atomic wave packets is a key tool and a strong requirement in the context of atom interferometry [56–64] and quantum information processing [30, 31, 33]. Both of these rely on the coherent dynamics of macroscopic superposition states created by the tunnelling in macroscopic and mesoscopic systems [53, 149–151].

In this Chapter, the evolution of a macroscopic quantum coherence in a noisy environment is explored by considering an atom in a double-well potential, or more generally in an optical lattice structure [152]. The study of the latter has received much attention over recent years for its potential application in quantum information processing [31, 33]. The separation of the lattice sites is of the order of optical wavelengths (half of the wavelength of the laser adopted to create the lattice), which may be considered a macroscopic distance when compared to atomic dimensions. The delocalized states resulting from tunnelling over those distances

are susceptible to decoherence due to the interaction with the noisy environment. In particular, magnetically trapped atoms experience a fluctuating electromagnetic field arising from the surface [7–10, 45, 46, 48, 49, 51] which causes an incoherent evolution in each site of a double-well potential. Here, the decoherence properties of an atomic spatial superposition state are derived within the framework of the quantum electrodynamic theory for the electromagnetic field in dielectric media introduced in Chapter 2.

This Chapter is organized as follows. In Section 4.1, the density matrix of the atom is obtained in the presence of a fluctuating magnetic field and an expression for spatial decoherence is derived. Section 4.2 focusses on a particular substrate geometry, a planar multilayered structure.

4.1 Spatial decoherence rate

An atom is placed in one of two adjacent sites of a double well potential or of an optical lattice, as shown in Fig. 4.1. Denoting by $|1,0\rangle$ and $|0,1\rangle$ the two sites of

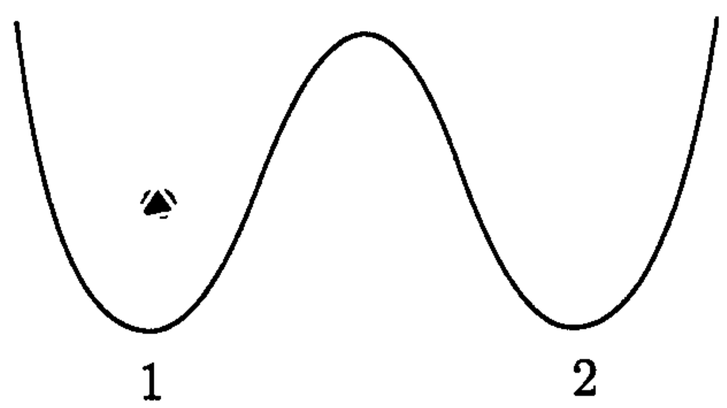

Figure 4.1: Schematic representation of a double well potential with an atom placed in one of the two sites.

the double well, the atomic density matrix at an arbitrary time t_0 may be written in the position basis as

$$\rho_A(t_0) = \begin{pmatrix} 1 & 0 \\ 0 & 0 \end{pmatrix}. \tag{4.1}$$

By denoting the creation operators of the atom at the lattice site i with $\hat{a}_i^\dagger$ and the occupation number operator with $\hat{n}_i$, the evolution of the system can be described by the Hamiltonian [153, 154]

$$\hat{H} = \sum_i \epsilon_i \hat{n}_i - J \sum_{i \neq j} \hat{a}_i^\dagger \hat{a}_j + \frac{U}{2} \sum_i \hat{n}_i (\hat{n}_i - 1), \tag{4.2}$$

where ϵ_i is the energy for each site, J represents the hopping matrix element between the two sites and U is the on-site energy. The temporal evolution of the density matrix is given by

$$\rho_A(t) = \hat{U} \rho(t_0) \hat{U}^\dagger, \tag{4.3}$$

where $\hat{U}(t)$ is the temporal evolution operator $\hat{U}(t) = e^{-i\hat{H}t/\hbar}$, if $\epsilon_1 = \epsilon_2 = \epsilon$ then the evolution is periodic in time with a period $\pi\hbar/J$. The tunneling interaction of

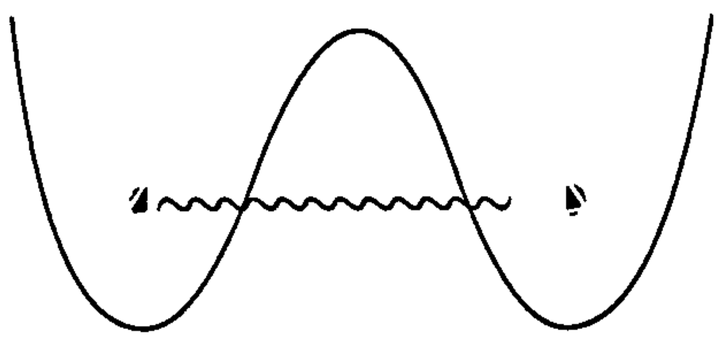

Figure 4.2: Schematic representation of a double well potential with an atom in a spatial superposition of the two sites.

Eq. (4.2) allows the atom's wave function to coherently spread over the neighboring site as depicted in Fig. 4.2, so eventually its state can be written in the occupation-number basis as

$$|\psi(t=0)\rangle_A = \frac{1}{\sqrt{2}} \left(|1,0\rangle + |0,1\rangle \right). \tag{4.4}$$

For the sake of simplicity, it is assumed that the equal superposition has been established at time t=0 and that no tunneling occurs at later times. This means that the tunneling interaction is thought to be frozen over a time period longer than the decoherence time. The fluctuating environment arising from the materials

constituting the chip acts on the spatial superposition leading to an incoherent evolution at each site. Although the atom is still trapped, spin-flip transitions can take place at different times in each well and cause the spatial superposition state to collapse to a mixed state with the atom in either one of the two sites.

In the experiment reported in [8], ^{87}Rb atoms are initially pumped into the low-field seeking hyperfine state $|F, m_F\rangle = |2, 2\rangle$ and for sufficiently tight magnetic traps, atoms in the $|F, m_F\rangle = |2, 1\rangle$ state are also trapped. Spin flips to even lower magnetic sublevels cause the atoms to be expelled from the trap. In such case, spatial decoherence is no more a matter of interest. Hence, it is sufficient to treat the atomic system in a two-level approximation described by the following atomic Hamiltonian

$$\hat{H}_A = \frac{1}{2}\hbar\omega_A(|i\rangle\langle i| - |f\rangle\langle f|), \tag{4.5}$$

where $|i\rangle$ and $|f\rangle$ are the initial and final states associated with the spin-flip transition and ω_A the transition frequency. The Hamiltonian describing the combined system of electromagnetic field and absorbing matter has been obtained in Chapter 2 and can be written in terms of the bosonic field operators $\hat{\mathbf{f}}(\mathbf{r}, \omega)$ and $\hat{\mathbf{f}}^\dagger(\mathbf{r}, \omega)$ as in Eq. (2.37).

The interaction of an atom, located at position $\mathbf{r}_a$, with a magnetic field $\hat{\mathbf{B}}(\mathbf{r})$ is described by the Zeeman interaction Hamiltonian

$$\hat{H}_Z = -\hat{\boldsymbol{\mu}} \cdot \hat{\mathbf{B}}(\mathbf{r}_a), \tag{4.6}$$

where $\hat{\mathbf{B}}(\mathbf{r}_a)$ is given by Eq. (2.40), together with Eq. (2.39) and Eqs. (2.41)-(2.42). The magnetic moment operator in Eq. (4.6) associated with the transition $|i\rangle \rightarrow |f\rangle$ can be written as $\hat{\boldsymbol{\mu}} = \boldsymbol{\mu}|i\rangle\langle f| + \text{h.c.}$ and the magnetic moment vector has been already given in Eqs. (1.31)-(1.32) as

$$\boldsymbol{\mu} = g_S\mu_B\langle i|\hat{\mathbf{S}}|f\rangle. \tag{4.7}$$

Inserting Eq. (2.40) into Eq. (4.6) and adopting the rotating-wave approximation

gives the following Zeeman interaction Hamiltonian

$$\begin{aligned}\hat{H}_Z &= -\mu_B g_S \left[\langle f|\hat{S}_q|i\rangle \hat{\xi}^\dagger \hat{B}_q(\mathbf{r}_a) + \text{h.c.}\right] \\ &= -\mu_B g_S \left[\langle f|\hat{S}_q|i\rangle \int_0^\infty d\omega \frac{\omega}{c^2}\sqrt{\frac{\hbar}{\varepsilon_0 \pi}}\,\epsilon_{qpj}\,\partial_p \right. \\ &\qquad \left. \times \int d^3\mathbf{s}\sqrt{\varepsilon_I(\mathbf{s},\omega)}G_{ji}(\mathbf{r}_a,\mathbf{s},\omega)\hat{f}_i(\mathbf{s},\omega)\hat{\xi}^+ + \text{H.c.}\right], \qquad (4.8)\end{aligned}$$

where $\hat{\xi} = |f\rangle\langle i|$ denotes the atomic spin lowering operator which obeys the commutation relation $[\hat{\xi}_z, \hat{\xi}^{(\pm)}] = \pm\hat{\xi}^{(\pm)}$, with $\hat{\xi}_z \equiv \frac{1}{2}(|i\rangle\langle i| - |f\rangle\langle f|)$.

The state of the atom needs to be rewritten in a way that contains information over both the spatial and internal degrees of freedom. The number basis state, indicating either the first or the second site, it will be denoted in the following by a subindex $|1,0\rangle = |()_1\rangle$ and $|0,1\rangle = |()_2\rangle$, where () represents the internal atomic state. The initial total state of the atom is then

$$|\psi_A\rangle = \frac{1}{\sqrt{2}}\left(|i_1\rangle + |i_2\rangle\right). \qquad (4.9)$$

The system composed of the two-level atom and the fluctuating magnetic field, initially in the vacuum state $|0\rangle$, reads

$$|\psi_{AF}\rangle = \frac{1}{\sqrt{2}}\left(|i_1\rangle + |i_2\rangle\right)\otimes|0\rangle = \frac{1}{\sqrt{2}}\left(|i_1,0\rangle + |i_2,0\rangle\right). \qquad (4.10)$$

The Hamiltonian describing the evolution of the combined system is given by the sum of the field Hamiltonian $\hat{H}_F$ of Eq. (2.37), the free atomic Hamiltonian $\hat{H}_A$ of Eq. (4.5) and the Zeeman Hamiltonian $\hat{H}_Z$ introduced in Eq. (4.8). The system wave function of Eq. (4.10) at time t is an arbitrary superposition of all the possible

spatial and internal atomic states and can be described as

$$\begin{aligned}|\psi_{AF}(t)\rangle &= C_{i_1}(t)e^{-i\omega_A t/2}|i_1,0\rangle + C_{i_2}(t)e^{-i\omega_A t/2}|i_2,0\rangle \\ &\quad + \int d^3\mathbf{r}\int_0^\infty d\omega\, C_{f_1,m}(\mathbf{r},\omega,t)e^{-i(\omega-\omega_A/2)t}|f_1,1_m(\mathbf{r},\omega)\rangle \\ &\quad + \int d^3\mathbf{r}\int_0^\infty d\omega\, C_{f_2,m}(\mathbf{r},\omega,t)e^{-i(\omega-\omega_A/2)t}|f_2,1_m(\mathbf{r},\omega)\rangle, \quad (4.11)\end{aligned}$$

where $|0\rangle$ and $|1_m(\mathbf{r},\omega)\rangle$ denote the vacuum and single-excitation states of the electromagnetic field, respectively. The Schrödinger equation yields ($a = 1, 2$)

$$\begin{aligned}\dot{C}_{i_a}(t) &= \frac{i\mu_B g_S}{c^2\sqrt{\pi\hbar\varepsilon_0}}\langle f|\hat{S}_q|i\rangle\int d^3\mathbf{r}\int_0^\infty d\omega\,\omega\, e^{-i(\omega-\omega_A)t} \\ &\quad \times\sqrt{\varepsilon_I(\mathbf{r},\omega)}\epsilon_{qpj}\partial_p\, G_{jm}(\mathbf{r}_a,\mathbf{r},\omega)\, C_{f_a,m}(\mathbf{r},\omega,t), \quad (4.12)\end{aligned}$$

$$\begin{aligned}\dot{C}_{f_a,m}(\mathbf{r},\omega,t) &= \frac{i\mu_B g_S}{c^2\sqrt{\pi\varepsilon_0\hbar}}\langle i|\hat{S}_q|f\rangle\omega e^{i(\omega-\omega_A)t} \\ &\quad \times\sqrt{\varepsilon_I(\mathbf{r},\omega)}\epsilon_{qpj}\partial_p G^*_{jm}(\mathbf{r}_a,\mathbf{r},\omega)C_{i_a}(t). \quad (4.13)\end{aligned}$$

By making use of the relation of Eq. (2.31) for the Green function, the result of the formal integration of $C_{f_a,m}(\mathbf{r},\omega,t)$ is inserted into $\dot{C}_{i_a}(t)$ with the initial condition $C_{f_a,m}(\mathbf{r},\omega,0) = 0$, and Eq. (4.12) reads

$$\dot{C}_{i_a}(t) = \int_0^t dt'\, K_a(t-t')C_{i_a}(t'), \quad (4.14)$$

where the integral kernel is given by

$$\begin{aligned}K_a(t-t') &= -\frac{(\mu_B g_s)^2}{c^2\pi\varepsilon_0\hbar}\,\langle f|\hat{S}_q|i\rangle\,\langle i|\hat{S}_k|f\rangle \\ &\quad \times\int_0^\infty d\omega\, e^{-i(\omega-\omega_A)(t-t')}\mathrm{Im}\left[\overrightarrow{\boldsymbol{\nabla}}\times\boldsymbol{G}(\mathbf{r}_a,\mathbf{r}_a,\omega)\times\overleftarrow{\boldsymbol{\nabla}}\right]_{qk}. \quad (4.15)\end{aligned}$$

Both sides of Eq. (4.14) are integrated over t,

$$C_{i_a}(T) - C_{i_a}(0) = \int_0^T dt \int_0^t dt' K_a(t-t') C_{i_a}(t') \tag{4.16}$$

$$= \int_0^T dt' \left(\int_{t'}^T dt K_a(t-t') \right) C_{i_a}(t')$$

$$= \int_0^T dt' \, \bar{K}_a(T-t') C_{i_a}(t'), \tag{4.17}$$

with the integrated kernel given by

$$\int_{t' \to 0}^{T \to (T-t')} dt \, K_a(t-t') = \bar{K}_a(T-t'). \tag{4.18}$$

If T is now replaced by t, the integrated kernel of Eq. (4.18) assumes the form

$$\bar{K}_a(t-t') = \frac{(\mu_B g_S)^2}{c^2 \pi \epsilon_0 \hbar} \langle f|\hat{S}_q|i\rangle \langle i|\hat{S}_k|f\rangle \times \int_0^\infty d\omega \, \frac{e^{-i(\omega-\omega_A)(t-t')} - 1}{i(\omega-\omega_A)} \mathrm{Im} \left[\overrightarrow{\nabla} \times \boldsymbol{G}(\mathbf{r}_a, \mathbf{r}_a, \omega) \times \overleftarrow{\nabla} \right]_{qk}, \tag{4.19}$$

and with the initial condition $C_{i_a}(0) = 1$, Eq. (4.17) can be rewritten as

$$C_{i_a}(t) = 1 + \int_0^t dt' \, \bar{K}_a(t-t') C_{i_a}(t'). \tag{4.20}$$

Markov approximation

The integral equation (4.17) is a well-known Volterra integral equation of the second kind. Although an algorithm to solve such an equation can be found numerically, this study adopts an approach similar to the Weisskopf-Wigner decay theory [155]. It is then worth revisiting Eq. (4.15) and write $K_a(t-t')$ in the

simplified form

$$K_a(t-t') = \int d\Delta e^{-i\Delta(t-t')} W_\omega^2, \tag{4.21}$$

where $\Delta = \omega - \omega_A$. Note that in Eq. (4.14), the value of $C_{i_a}(t)$ depends on the values of $C_{i_a}(t')$ at all earlier times. If the kernel is sharply peaked at $t = t'$ then only values of t' close to t contribute significantly to the integral in Eq. (4.17). In particular, when W_ω^2 is broad with slowly varying coupling, the kernel being the Fourier transform of W_ω^2 is sharply peaked around $t = t'$. In the Markov approximation, i.e. when in a coarse-grained description of the atomic motion, memory effects are disregarded, $C_{i_a}(t')$ can be replaced by $C_{i_a}(t)$ and taken out of the integral in Eq. (4.14)

$$\dot{C}_{i_a}(t) = C_{i_a}(t) \int_0^t dt'\, K_a(t-t') = C_{i_a}(t) \int_0^t d\tau\, K_a(\tau). \tag{4.22}$$

The Markov approximation is adopted under the assumption that $K_a(\tau)$ is sharply peaked at $\tau = 0$, which makes the integral in Eq. (4.22) independent of its upper limit $\tau = t$. The integral can be solved by letting the upper limit tend to infinity. In doing so, the integral over τ must converge and therefore a convergence factor $e^{-\eta\tau}$ is inserted, performing the limit $\eta \longrightarrow 0^+$ after the integration has been performed. The integral in Eq. (4.22) can be written as

$$\begin{aligned} &\lim_{\eta\to 0^+} \int_0^\infty d\tau \left(\int d\Delta\, e^{-i\Delta\tau - \eta\tau}\, W_\omega^2 \right) \\ &\quad = \lim_{\eta\to 0^+} -i \int d\Delta\, \frac{W_\omega^2}{\Delta - i\eta} \\ &\quad = \pi W_{\omega_A}^2 - i\mathcal{P} \int d\Delta\, \frac{W_\omega^2}{\Delta}. \end{aligned} \tag{4.23}$$

The last line has been obtained by separating the real and imaginary parts of the integrand and recognising that, for $\Delta = \omega - \omega_A$, the imaginary part is a principal part integral, while the real part contains a Lorentzian function that tends to a delta function $\delta(\omega - \omega_A)$ for $\eta \longrightarrow 0^+$. This is equivalent to using the following

replacement in the evaluation of the integral of Eq. (4.19)

$$\frac{\left(e^{-i(\omega-\omega_A)(t-t')}-1\right)}{i(\omega-\omega_A)} \rightarrow -\pi\delta(\omega-\omega_A)+i\mathcal{P}\frac{1}{\omega-\omega_A}. \tag{4.24}$$

Equation (4.19) can be rewritten in the condensed form

$$\bar{K}_a(t-t') = -\frac{1}{2}\Gamma_a + i\delta\omega_a. \tag{4.25}$$

by defining the following coefficients

$$\Gamma_a = 2\frac{(\mu_B g_S)^2}{c^2\varepsilon_0\hbar}\langle f|\hat{S}_q|i\rangle\langle i|\hat{S}_k|f\rangle \mathrm{Im}\left[\overrightarrow{\boldsymbol{\nabla}}\times \boldsymbol{G}(\mathbf{r}_a,\mathbf{r}_a,\omega_A)\times\overleftarrow{\boldsymbol{\nabla}}\right]_{qk}, \tag{4.26}$$

and

$$\delta\omega_a = \frac{(\mu_B g_S)^2}{c^2\pi\varepsilon_0\hbar}\langle f|\hat{S}_q|i\rangle\langle i|\hat{S}_k|f\rangle\mathcal{P}\int_0^\infty d\omega \frac{\mathrm{Im}\left[\overrightarrow{\boldsymbol{\nabla}}\times \boldsymbol{G}(\mathbf{r}_a,\mathbf{r}_a,\omega_A)\times\overleftarrow{\boldsymbol{\nabla}}\right]_{qk}}{\omega-\omega_A}. \tag{4.27}$$

By substituting into Eq. (4.20) the kernel function expression of Eq. (4.25), the time evolution of the coefficients $C_{i_a}(t)$ is finally obtained as

$$C_{i_a}(t) = \exp\left[\left(-\frac{1}{2}\Gamma_a + i\delta\omega_a\right)t\right]. \tag{4.28}$$

The coefficients Γ_a and $\delta\omega_a$ defined in Eqs. (4.26) and (4.27) represent the spin-flip rate and the line shift, respectively, and have been derived in a similar fashion in [49, 156]. In what follows, it is assumed that the line shift $\delta\omega_a$ caused by the interaction with the quantized electromagnetic field is negligible. This can be seen as follows. The Green tensor appearing in Eq. (4.27) is the same tensor playing the role of a response function for the electric and magnetic field and it satisfies the Kramers-Kronig relations for a complex-valued function $g(\omega) = \mathrm{Re}[g(\omega)] + i\mathrm{Im}[g(\omega)]$

[113,114], such as

$$\mathrm{Re}[g(\omega)] = \frac{1}{\pi}\mathcal{P}\int_{-\infty}^{\infty} d\omega' \frac{\mathrm{Im}[g(\omega)]}{\omega' - \omega}, \tag{4.29}$$

$$\mathrm{Im}[g(\omega)] = -\frac{1}{\pi}\mathcal{P}\int_{-\infty}^{\infty} d\omega' \frac{\mathrm{Re}[g(\omega)]}{\omega' - \omega}. \tag{4.30}$$

The lower limit of the integral in Eq. (4.27) can be extended to $-\infty$ with little error as the integrand is peaked around ω_A. Hence, Eq. (4.27) is proportional to the real part of the Green function and it can be rewritten as

$$\delta\omega_a = \frac{(\mu_B g_S)^2}{c^2\varepsilon_0\hbar}\langle f|\hat{S}_q|i\rangle\langle i|\hat{S}_k|f\rangle \,\mathrm{Re}\left[\overrightarrow{\nabla}\times \boldsymbol{G}(\mathbf{r}_a,\mathbf{r}_a,\omega_A)\times\overleftarrow{\nabla}\right]_{qk}. \tag{4.31}$$

The line shift is of the same order of magnitude as the spin-flip rate. For typical experimental realizations [8–10, 24, 45, 48–51], this will be in the sub-Hz range. This means that $\delta\omega_a$ can be neglected as it is extremely small when compared to the spin-flip transition frequency ω_A.

Substituting Eq. (4.28) into Eq. (4.13), the formal solution of Eq. (4.13) is obtained as

$$\begin{aligned} C_{f_a,m}(\mathbf{r},\omega,t) &= \frac{i\mu_B g_S}{c^2\sqrt{\pi\varepsilon_0\hbar}}\langle i|\hat{S}_q|f\rangle\omega\sqrt{\varepsilon_I(\mathbf{r},\omega)}\epsilon_{qpj}\partial_p \\ &\quad\times G^*_{jm}(\mathbf{r}_a,\mathbf{r},\omega)\int_0^t dt' e^{i(\omega-\omega_A)t'}e^{-\frac{1}{2}\Gamma_a t'}. \end{aligned} \tag{4.32}$$

Once the formal expressions of both the coefficients C_{i_a} and $C_{f_a,m}$ have been derived, the system density matrix $\rho_{AF} = |\psi_{AF}(t)\rangle\langle\psi_{AF}(t)|$ at time t can be written

in the basis $(|i_1\rangle, |f_1\rangle, |i_2\rangle, |f_2\rangle)$ as

$$\rho_{AF} = \begin{pmatrix} \rho_{11} & \rho_{13} & \rho_{12} & \rho_{14} \\ \rho_{31} & \rho_{33} & \rho_{32} & \rho_{34} \\ \rho_{21} & \rho_{23} & \rho_{22} & \rho_{24} \\ \rho_{41} & \rho_{43} & \rho_{42} & \rho_{44} \end{pmatrix}, \tag{4.33}$$

and the atomic density matrix can be obtained by tracing over the field

$$\begin{aligned} \rho_A(t) &= \langle 0|\rho_{AF}(t)|0\rangle + \sum_i \int d^3\mathbf{r} \int_0^\infty d\omega \, \langle 1_i(\mathbf{r},\omega)|\rho_{AF}|1_i(\mathbf{r},\omega)\rangle \\ &= \begin{pmatrix} \rho_{11} & 0 & \rho_{12} & 0 \\ 0 & \rho_{33} & 0 & \rho_{34} \\ \rho_{21} & 0 & \rho_{22} & 0 \\ 0 & \rho_{43} & 0 & \rho_{44} \end{pmatrix}. \end{aligned} \tag{4.34}$$

As the interest here is in the position of the atom and not in its internal state, the atomic density matrix can be written in a simpler way, by tracing over the internal states as well,

$$\rho_A = \begin{pmatrix} \rho_{11}+\rho_{33} & \rho_{12}+\rho_{34} \\ \rho_{21}+\rho_{43} & \rho_{22}+\rho_{44} \end{pmatrix} = \begin{pmatrix} \varrho_{11}(t) & \varrho_{12}(t) \\ \varrho_{12}^*(t) & \varrho_{22}(t) \end{pmatrix}, \tag{4.35}$$

where the matrix elements ϱ_{ij} have to be calculated from

$$\varrho_{11}(t) = |C_{i_1}(t)|^2 + \sum_i \int d^3\mathbf{r} \int_0^\infty d\omega \, |C_{f_1,m}(\mathbf{r},\omega,t)|^2, \tag{4.36}$$

$$\varrho_{22}(t) = |C_{i_2}(t)|^2 + \sum_i \int d^3\mathbf{r} \int_0^\infty d\omega \, |C_{f_2,m}(\mathbf{r},\omega,t)|^2, \tag{4.37}$$

$$\begin{aligned} \varrho_{12}(t) &= C_{i_1}(t)C_{i_2}^*(t) \\ &\quad + \sum_i \int d^3\mathbf{r} \int_0^\infty d\omega \, C_{f_1,m}(\mathbf{r},\omega,t)\, C_{f_2,m}^*(\mathbf{r},\omega,t), \end{aligned} \tag{4.38}$$

First, it can be checked that the diagonal elements $\varrho_{11}(t)$ and $\varrho_{22}(t)$ are properly normalized to $\varrho_{11}(t) = \varrho_{22}(t) = 1/2$ by inserting Eqs. (4.28) and (4.32) into Eqs. (4.36) and (4.37), respectively. Thus, as a consistency check it results that $\mathrm{Tr}[\rho_A] = 1$.

The calculation of the off-diagonal term of Eq. (4.38) gives

$$\begin{aligned}\varrho_{12}(t) &= e^{-\Gamma t} + 2\left(1 - e^{-\Gamma t}\right)\frac{(\mu_B g_S)^2}{c^2 \varepsilon_0 \hbar} \\ &\times \langle i|\hat{S}_q|f\rangle\langle f|\hat{S}_k|i\rangle \frac{\mathrm{Im}\left[\vec{\nabla} \times \boldsymbol{G}(\mathbf{r}_2, \mathbf{r}_1, \omega_A) \times \overleftarrow{\nabla}\right]_{kq}}{\Gamma}\end{aligned} \tag{4.39}$$

where the summer over indices k and q is implied and $\Gamma = (\Gamma_1 + \Gamma_2)/2$ is now the arithmetic mean of the spin-flip rates, Eq. (4.26), at each site and for a planar geometry the spin-flip rates Γ_i coincide such that $\Gamma \equiv \Gamma_1 = \Gamma_2$. Equation (4.39) constitutes the main result of this Section. It provides, via the Green function $\boldsymbol{G}(\mathbf{r}_2, \mathbf{r}_1, \omega_A)$, an elegant way to assess the loss of spatial coherence for arbitrarily shaped substrates. Recalling the expression for the expectation value of the magnetic field fluctuations $\langle \hat{\mathbf{B}}(\mathbf{r}, \omega)\hat{\mathbf{B}}^\dagger(\mathbf{r}', \omega')\rangle$, Eq. (2.48), it follows that Eq. (4.39) can be rewritten as

$$\varrho_{12}(t) = e^{-\Gamma t} + \left(1 - e^{-\Gamma t}\right)\frac{\langle i|\hat{S}_q|f\rangle\langle f|\hat{S}_k|i\rangle \int_0^\infty d\omega \langle \hat{B}_k(\mathbf{r}_2, \omega_A)\hat{B}_q^\dagger(\mathbf{r}_1, \omega)\rangle}{\langle i|\hat{S}_q|f\rangle\langle f|\hat{S}_k|i\rangle \int_0^\infty d\omega \langle \hat{B}_k(\mathbf{r}_1, \omega_A)\hat{B}_q^\dagger(\mathbf{r}_1, \omega)\rangle}. \tag{4.40}$$

Equation (4.39), or equivalently Eq. (4.40), consists of two parts. The first is a (spatially local) exponential decay that describes the effect of the transition from the initial spin state $|i\rangle$ to the final spin state $|f\rangle$. The second term is a (spatially non-local) non-exponential term which is proportional to the spatial coherence function and will be investigated in more detail in the following Section.

Note that, although the calculations have been performed for surfaces held at zero temperature T, the extension to finite temperatures is trivial. As seen from Eq. (2.48), the correlation function of the magnetic field at temperature T needs

to be multiplied by a factor $(\bar{n}_{\rm th}+1)$. This means that in Eq. (4.40) both the numerator and the denominator are multiplied by factors $(\bar{n}_{\rm th}+1)$ which then cancel out.

4.2 Planar multilayer substrates

All the formulas derived up to this point were valid for arbitrary substrate geometries. A particular geometric arrangement is fixed by defining the correct boundary conditions for the dyadic Green function $\boldsymbol{G}(\mathbf{r},\mathbf{s},\omega)$. This Section focusses on the spatially non-local term of Eq. (4.40) for planar multilayer dielectrics.

4.2.1 Spatial coherence above multilayers

A function $S(\mathbf{r}_1,\mathbf{r}_2,\omega_A)$ containing all the spatially non-local information about the system can be extracted from Eq. (4.40) and $\varrho_{12}(t)$ is written in the simplified form

$$\varrho(t)=e^{-\Gamma t}+\left(1-e^{-\Gamma_{12}t}\right)S(\mathbf{r}_1,\mathbf{r}_2,\omega_A)\,. \tag{4.41}$$

In the following, only the spatially non-local term is considered (which is equivalent to taking the long-time limit of Eq. (4.41))

$$S(\mathbf{r}_1,\mathbf{r}_2,\omega_A)=\frac{\langle i|\hat{S}_q|f\rangle\langle f|\hat{S}_k|i\rangle\int_0^\infty d\omega\langle\hat{B}_k(\mathbf{r}_2,\omega_A)\hat{B}_q^\dagger(\mathbf{r}_1,\omega)\rangle}{\langle i|\hat{S}_q|f\rangle\langle f|\hat{S}_k|i\rangle\int_0^\infty d\omega\langle\hat{B}_k(\mathbf{r}_1,\omega_A)\hat{B}_q^\dagger(\mathbf{r}_1,\omega)\rangle}. \tag{4.42}$$

Note that in a planar geometry in which the atom is held at a fixed distance to the material surface, the spin-flip rates Γ_i coincide due to translational invariance, i.e. $\Gamma\equiv\Gamma_1=\Gamma_2$. Note also that Eq. (4.42) is temperature-independent as the temperature enters only in the pre-factors $e^{-\Gamma t}$ and $\left(1-e^{-\Gamma t}\right)$.

The attention is now restricted to a half-space filled with a dielectric or a metal of dielectric permittivity $\varepsilon(\omega)$. The Green tensor for the electromagnetic field scattering off a planar surface is reported in Appendix B following Ref. [74, 157]. For the case of an atom above a substrate, only the reflection term $\boldsymbol{R}^{(12)}(\mathbf{r},\mathbf{r}',\omega)$ in

Eq. (B.1) is relevant and for a planar geometry the calculations are carried out by writing $\boldsymbol{R}^{(12)}(\mathbf{r}, \mathbf{r}', \omega)$ in terms of the Weyl expansion as in Eq. (B.3). The atom-surface distance d enters the Green function as an exponential factor $e^{ik_{1z}(z+z')} \equiv e^{2ik_{1z}d}$, with k_{1z} defined as

$$k_{1z} = \sqrt{\frac{\omega^2}{c^2} - k_{\parallel}^2}, \tag{4.43}$$

and $k_{\parallel}$ is the integration variable which represents the modulus of the wave-vector in the (x, y)-plane. For typical spin transition frequencies, the ratio $\omega^2/c^2 \approx 10^{-6}$ m^{-2} is negligible and the factor $k_{1z}d$ at the exponent can be approximated as

$$k_{1z}^2 d^2 = \frac{\omega^2}{c^2} d^2 - k_{\parallel}^2 d^2 \approx -k_{\parallel}^2 d^2, \tag{4.44}$$

which means that the transition wavelength, $\lambda = c/(2\pi\omega)$, is by far the biggest length scale in the system. The two-dimensional Fourier transform in Eq. (B.2) is calculated here by adopting polar coordinates and by performing the following substitutions $\mathbf{k}_{\parallel} = (k_x, k_y) \mapsto (K\cos\varphi, K\sin\varphi)$ and $d^2\, k_{\parallel} \mapsto K\, dK\, d\varphi$. The integration over φ allows the spin-flip rate Γ to be written as

$$\Gamma = \frac{(\mu_B g_S)^2}{8c^2\varepsilon_0\hbar}\, 3\pi \int \frac{K^2 dK}{(2\pi)^2} \frac{e^{-2Kd}}{2} \mathrm{Im}[r_{12}^{TE}], \tag{4.45}$$

where the spin matrix elements have been calculated for the hyperfine transition $|2,2\rangle \rightarrow |2,1\rangle$ of a ^{87}Rb atom. The line shift $\delta\omega_a$ in Eq. (4.31) can be computed

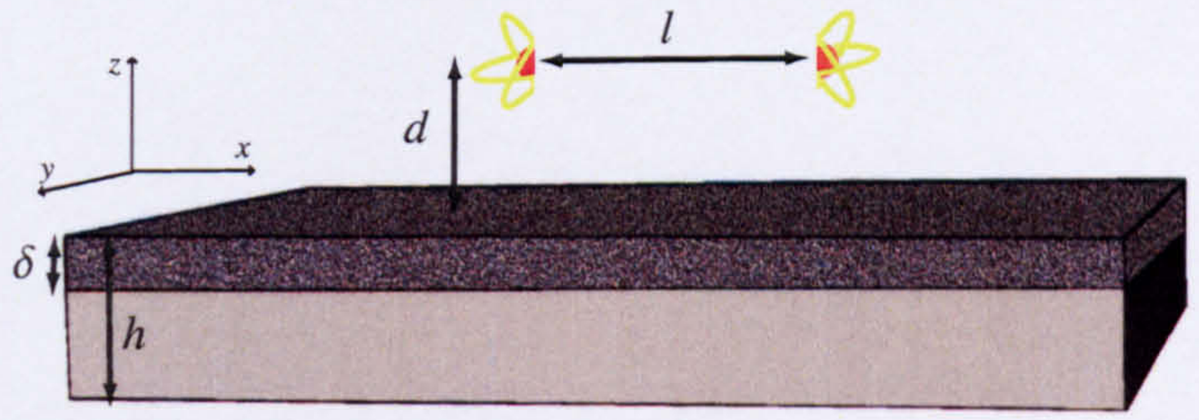

Figure 4.3: Schematic representation of the system geometry. An atom in a superposition of two positions separated by distance l, is located at a height d from a plain metallic layer of thickness h and skin depth δ.

by replacing $\mathrm{Im}[r_{12}^{TE}]$ with $\mathrm{Re}[r_{12}^{TE}]$ in Eq. (4.45). Moreover, it is easily seen that both Γ_a and $\delta\omega_a$ are of the same order of magnitude which means that $\delta\omega_a$ can be neglected when compared with spin-flip transition frequencies in the sub-Hz range.

The schematic representation of an atom located at a distance d away from the planar interface is depicted in Fig. 4.3. The lateral separation between the two distinct positions occupied by the atom is denoted by l. In particular, a ^{87}Rb atom with a transition frequency $f = 560$ kHz and an aluminium substrate with skin depth $\delta = 110\,\mu$m and dielectric permittivity $\varepsilon(\omega_A) \simeq 2.37\,10^{13}\,i$ are considered. In Fig. 4.4, the dependence of $S(\mathbf{r}_1, \mathbf{r}_2, \omega_A)$ on the separation l is shown

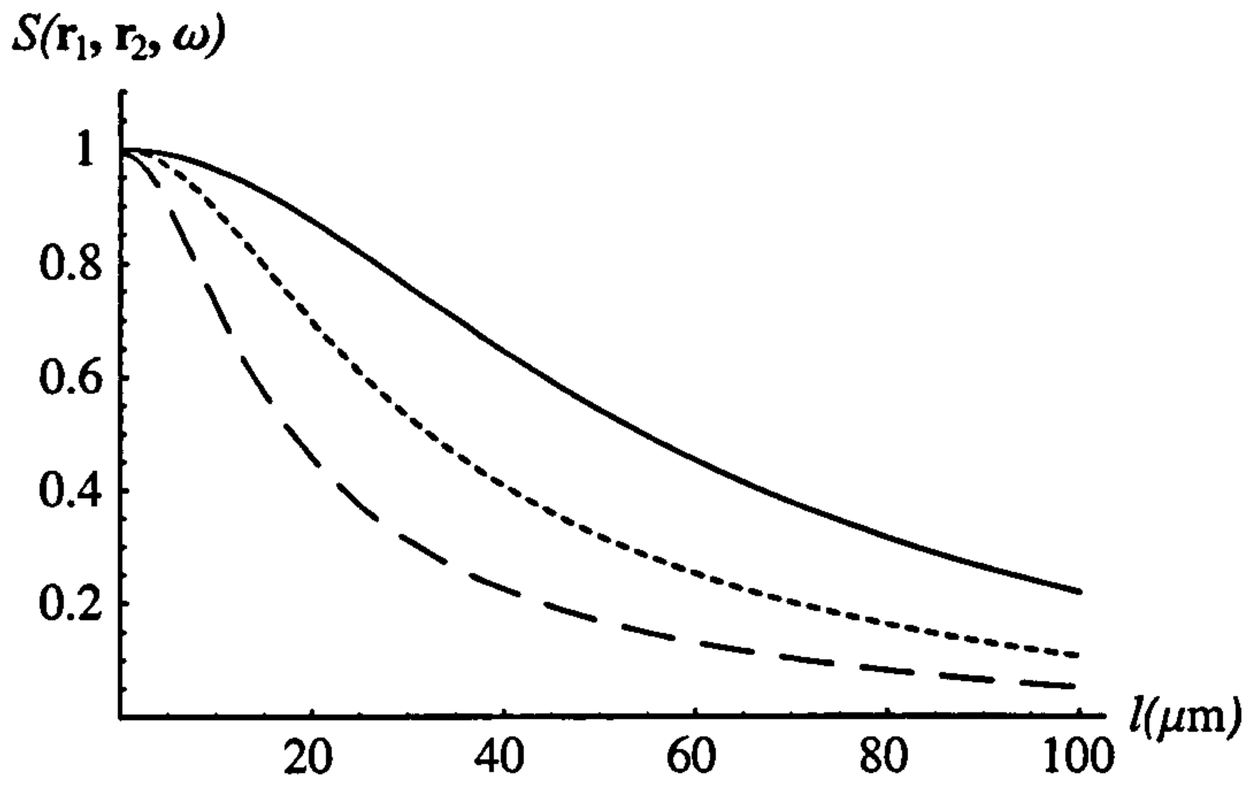

Figure 4.4: Plot of the spatial coherence function $S(\mathbf{r}_1, \mathbf{r}_2, \omega_A)$, Eq. (4.42), as a function of the lateral separation l for a transition frequency $f = 560$ kHz, and a skin depth $\delta = 110\,\mu$m. Three different distances from the surface are represented: $d = 20\,\mu$m (solid line), $d = 10\,\mu$m (dotted line), and $d = 5\,\mu$m (dashed line).

for three different atom-surface distances d. The non-local function $S(\mathbf{r}_1, \mathbf{r}_2, \omega_A)$ constitutes a measure of the spatial coherence. Clearly, for a lateral separation $l = 0$, $\mathbf{r}_1 = \mathbf{r}_2$ as the atom is placed in one site and $S(\mathbf{r}_1, \mathbf{r}_2, \omega_A) = 1$ as no spatial decoherence can take place. As a function of l, the decay of the spatial coherence starts off rather slowly. This is attributed to the fact that, for separations below the coherence length of the magnetic-field fluctuations, the spin flip is driven coherently

at both sites. The decay is much quicker for shorter atom-surface distances, as the magnetic field fluctuations are stronger.

In order to investigate the small-separation limit in some more detail, it is worth having a closer look at the Weyl expansion of the scattering Green tensor $\boldsymbol{R}^{(12)}(\mathbf{r},\mathbf{r}',\omega)$, Eq. (B.2). The separation l is nothing but $l = |\boldsymbol{\varrho} - \boldsymbol{\varrho}'|$ and serves as a parameter in the integral where $\boldsymbol{\varrho}$ is the position of the atom. Hence, the exponential $e^{i\mathbf{k}_\parallel\cdot(\boldsymbol{\varrho}-\boldsymbol{\varrho}')}$ in Eq. (B.2) can be expanded into powers of l and each term is then evaluated separately. The zeroth-order coefficient trivially leads to the spin-flip rate Γ_{12}. The contribution from terms proportional to l vanishes identically due to the symmetry of the generalized reflection coefficients $R_{ij}^{(12)}$ with respect to the wave-vector components $\mathbf{k}_\parallel$ in the (x,y)-plane. In fact, all odd powers of l vanish because of that symmetry.

Hence, the lowest non-vanishing power is l^2. It is straightforward to find analytical expressions for the spatial coherence in that limit by converting the additional factor K^2 due to the expansion of the exponential in Eq. (B.2), into a parameter differentiation with respect to the atom-surface distance d. That is, the replacement $K^2 \mapsto \frac{1}{4}\frac{\partial^2}{\partial d^2}$ is performed such that

$$S(\mathbf{r}_1,\mathbf{r}_2,\omega_A) = \frac{1}{\Gamma_{12}}\left(\Gamma - \frac{5l^2}{96}\frac{\partial^2}{\partial d^2}\Gamma\right) + \mathcal{O}(l^4). \tag{4.46}$$

In certain asymptotic regimes in which Γ can be expressed as a monomial $\propto d^{-n}$ of the atom-surface distance d (see, e.g. [45,47,50]), Eq. (4.46) can be rewritten in the form

$$S(\mathbf{r}_1,\mathbf{r}_2,\omega_A) = 1 - \frac{5n(n+1)l^2}{96d^2} + \mathcal{O}(l^4). \tag{4.47}$$

In addition to the planar half-space, the experimentally relevant situation in which a thin metallic layer of thickness h has been brought onto a dielectric substrate is addressed here. The generalized Fresnel coefficient for this three-layer system is given in Eq. (B.5). In the limit of thick films ($\delta, h \gg d$) the asymptotic behaviour of the spin-flip rate is $\Gamma \propto 1/d$ [45, 50] whereas for thin films ($\delta \gg d \gg h$),

$\Gamma \propto 1/d^2$ [47,50]. Thus, the small-l limit of Eq. (4.39) is finally obtained as

$$\varrho_{12}(t) = e^{-\Gamma t} - \frac{5\alpha l^2}{48 d^2}\left(1 - e^{-\Gamma t}\right) + \mathcal{O}(l^4)\,, \tag{4.48}$$

where $\alpha = 1$ for thick films and $\alpha = 3$ for thin films. It is interesting to note that the fall-off is three times faster for thin films than for thick films due to the fact that thick films are more likely to drive spin-flips coherently.

In order to see how the time scale is related to the expected lifetime, the exponential in Eq. (4.48) is expanded for short times as

$$|\varrho_{12}(t) - \varrho_{12}(0)| \cong \frac{5\alpha l^2}{48 d^2}\left(\frac{t}{\tau}\right) + \mathcal{O}(t^2) \tag{4.49}$$

where $\varrho_{12}(0) = 1$ and $\tau = \Gamma_{12}^{-1}$. The left-hand side in Eq. (4.49) can be thought of as a proper measure of decoherence due to spin flips in terms of physical parameters such as the spin-flip lifetime τ, the separation l and the distance from the surface d. This result is particularly interesting whenever a certain degree of spatial coherence has to be maintained, as in quantum information processing. The decoherence rate can be in principle minimised by achieving efficient control over experimental parameters as the ones appearing in Eq. (4.49).

For larger separations, however, it is difficult to find analytical approximations and one has to resort to numerical evaluations of the Fourier transform (B.2). It is interesting to calculate at what separation $l_{1/2}$ the spatial coherence drops to half its initial value as a function of the other length scales in the system. The behaviour of $l_{1/2}$ can be regarded as a measure of robustness against decoherence. The dependence of $l_{1/2}$ on the thickness h of the intermediate layer is plotted in Fig. 4.5 for three different skin depths: $\delta = 100\,\mu$m (solid line, corresponding to a good conductor such as Al of Cu at room temperature), $\delta = 50\,\mu$m (dashed line), and $\delta = 10\,\mu$m (dotted line) with a transition frequency of $f = 560$kHz. Although the latter two skin depth values are not realistic for materials at room temperature, at cryogenic temperatures these values can be achieved. For example, just above

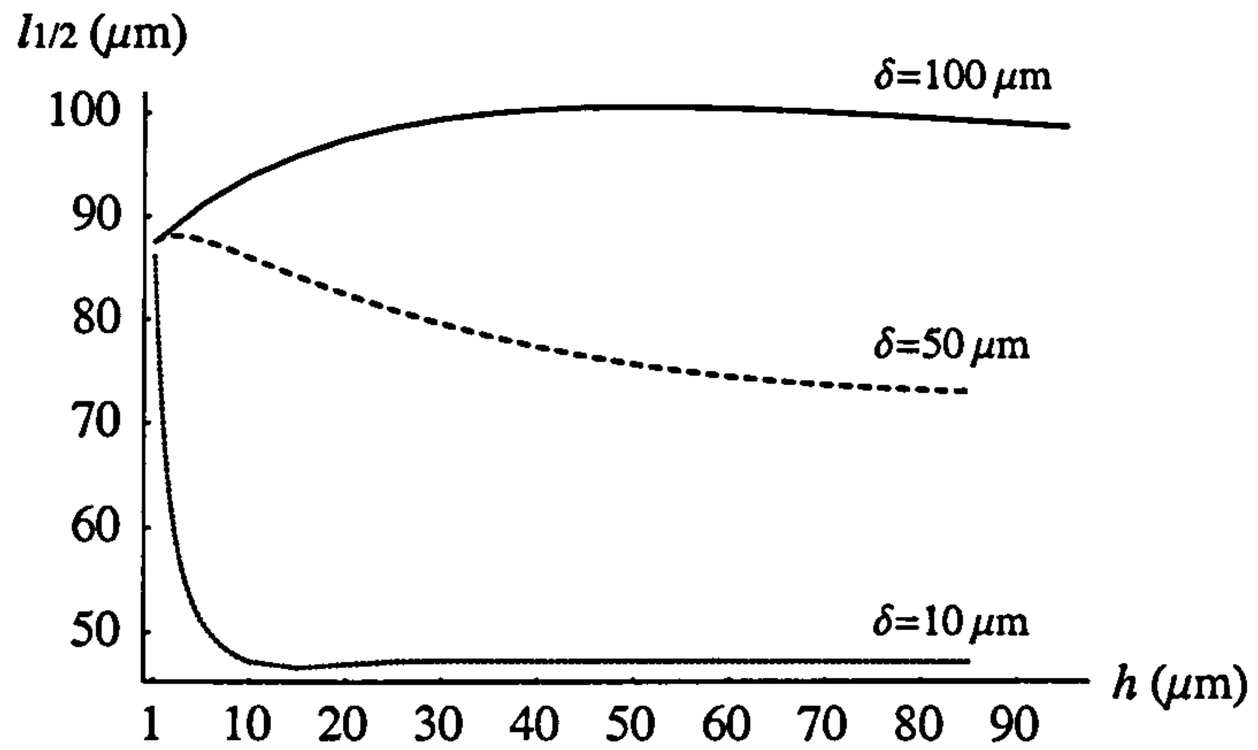

Figure 4.5: The parameter $l_{1/2}$ is represented as a function of the layer thickness h. The lateral separation $l_{1/2}$ is the distance between the two atom positons $\mathbf{r}_1$ and $\mathbf{r}_2$ after which the spatial coherence $S(\mathbf{r}_1, \mathbf{r}_2, \omega)$ has dropped to half its initial value. The skin depth varies from $\delta = 100\,\mu$m (solid line) to $\delta = 50\mu$m (dashed line) and $\delta = 1\,\mu$m (dotted line). The atom-surface distance is $d = 50\,\mu$m and all other parameters as in Fig. 4.4.

its critical temperature of $T_c = 9.2$ K, pure niobium shows a skin depth of only $\delta = 15\,\mu$m at $f \lesssim 1$ MHz [158].

For skin depths smaller than the atom-surface distance (dotted line in Fig. 4.5), the robustness of spatial coherence drops dramatically with increasing substrate thickness h until $h \sim \delta$. The number of fluctuating dipoles causing undesired spin flips increases with the thickness of the layer. Any increase beyond $h \sim \delta$ does not add much disturbance as the additional fluctuations would not reach the substrate surface. Note also that the coherence length $l_{1/2}$ levels out roughly at the value of the skin depth, $l_{1/2} \sim \delta$. For skin depths equal (dashed line in Fig. 4.5) or larger than the atom-surface distance (solid line), spatial coherence is robust over a wide range of substrate thicknesses h.

4.2.2 Near-field coherence length

So far, spatial decoherence has been considered a serious threat to the atomic superposition of two different positions. It is worth changing for a moment the point of view and look at the loss of coherence from the perspective of near-field

correlation properties. In this respect, the lateral separation $l_{1/2}$ plotted in Fig. 4.5 can be regarded as the magnetic-field coherence length. It has become clear by now that the spatial coherence strongly depends on the distance from the substrate and on the substrate's skin depth. The skin depth δ given in Eq. (1.41) is defined as the distance below the surface to which an incident electromagnetic radiation penetrates. The thickness of the layer emitting the fluctuating electromagnetic field must then be of the same order of the skin depth, and it can be thought of as an ensemble of radiating dipoles. With this in mind, a visual interpretation attempt is presented in the following for each line appearing in Fig. 4.5.

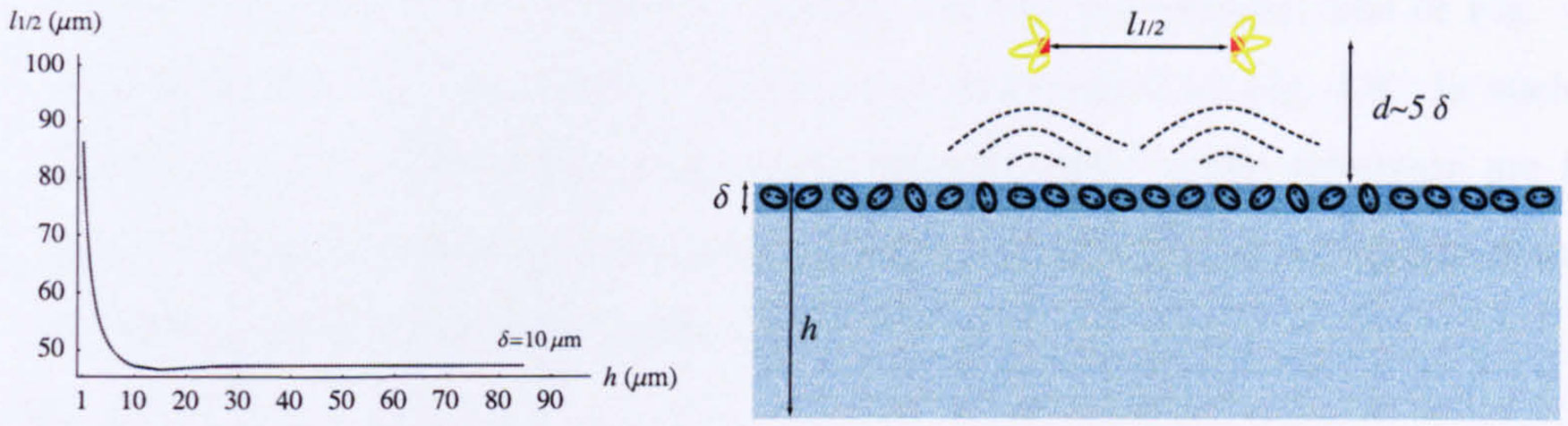

Figure 4.6: The plot on the left represents the coherence length $l_{1/2}$ as a function of the layer thickness h for an atom-surface distance $d = 50\,\mu$m and a skin depth $\delta = 10\,\mu$m. On the right, a schematic representation of the geometry of the system is given.

Consider first the bottom (dotted) line of Fig. 4.5 which has been obtained for an atom-surface distance $d = 50\,\mu$m and a skin depth $\delta = 10\,\mu$m, as depicted in Fig. 4.6. The emitting layer is much smaller than the height at which the atom is located. This causes the atom to see a very thin layer of radiating dipoles and each site experiences a different set of dipoles which acts incoherently. As soon as $h > \delta$, the coherence length $l_{1/2}$ stops decreasing as the radiating layer is not increasing anymore.

The second (dashed) line of Fig. 4.5 has been obtained for skin depth $\delta = 50\,\mu$m as illustrated in Fig. 4.7. The coherence length still decreases as long as the substrate thickness is less than or comparable with the skin depth $h \sim \delta$. Nevertheless, the decrease is not as dramatic as before and this may be ascribed to the dipoles located at the border of the skin depth layer which cannot be resolved

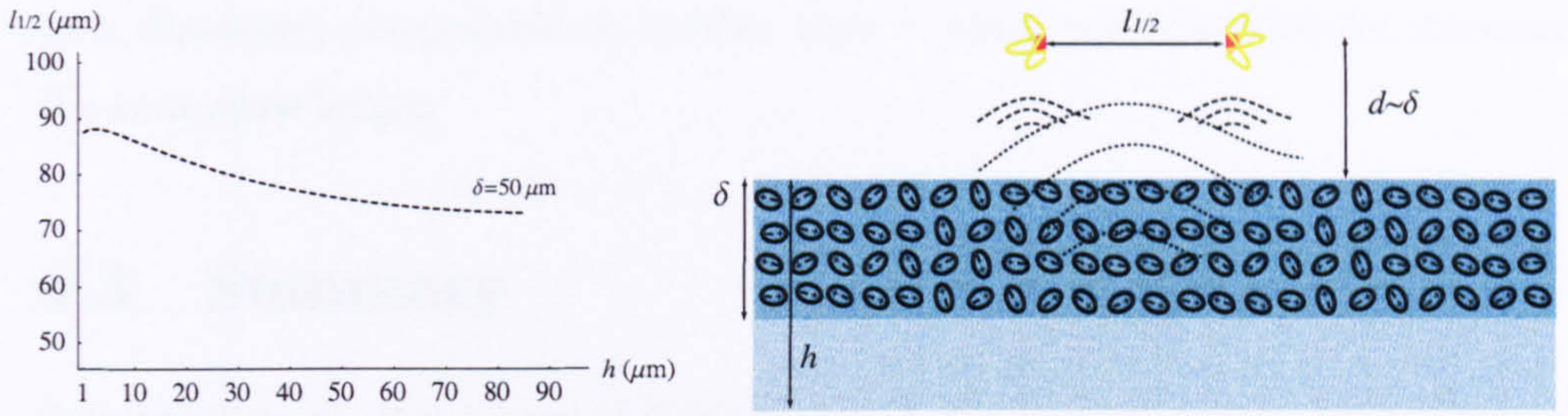

Figure 4.7: The plot on the left represents the coherence length $l_{1/2}$ as a function of the layer thickness h for an atom-surface distance $d = 50\,\mu$m and a skin depth $\delta = 50\,\mu$m. On the right, a schematic representation of the geometry of the system is given.

by each site and so act coherently. Finally, the top (continuous) line of Fig. 4.5 corresponding to a skin depth $\delta = 100\,\mu$m is represented in Fig. 4.8. In such a thick layer of emitting dipoles, the ones located deeper in the substrate are far enough from the two sites that can in principle be regarded as a coherent source of the electromagnetic field fluctuations.

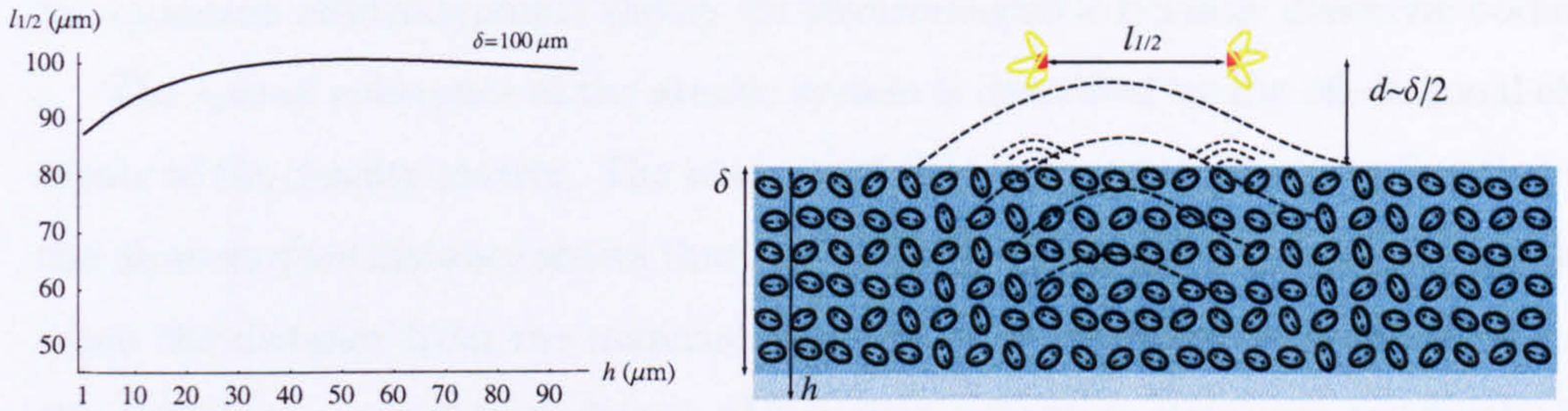

Figure 4.8: The plot on the left represents the coherence length $l_{1/2}$ as a function of the layer thickness h for an atom-surface distance $d = 50\,\mu$m and a skin depth $\delta = 100\,\mu$m. On the right, a schematic representation of the geometry of the system is given.

Obviously, this is an intuitive explanation of how the interplay of d and δ affects the coherence length $l_{1/2}$ and does not pretend to be an accurate description of reality. This discussion is still in agreement with the results presented in Ref. [50] about how small skin depths can boost the spin-flip lifetime of several orders of magnitude. A shorter skin depth is due to higher values of the conductivity, according to Eq. (1.41). A higher conductivity gives a stronger confining current density and consequently a smaller resistivity. This permits shorter trap-

ping distances, comparable or smaller than δ which are beneficial for increasing the coherence length.

4.3 Summary

In conclusion, the loss of spatial coherence of atomic superpositions due to thermally-driven spin flips has been investigated. When atoms in magnetic traps are held close to dielectric surfaces they experience fluctuating magnetic fields. These fields are produced by thermally-induced noise currents in the material, and they can be strong enough to drive an atomic spin flip. In particular, an atom in a superposition of two lattice sites above a planar dielectric surface has been considered. Thermally-driven spin-flip transitions interfere with this superposition leading to a decoherence of the atomic spatial state. The coupling between the atomic magnetic moment and the fluctuating magnetic field has been discussed in the framework of the quantum electrodynamic theory for electromagnetic fields in dielectric bodies.

The spatial coherence of the atomic system is described by the off-diagonal elements of the density matrix. The analysis of the off-diagonal term as a function of the atom-surface distance shows that the spatial decoherence rate becomes smaller when the distance from the material increases. For small lateral separations l of the atom's two possible positions, the spatial coherence decreases quadratically with l and is inversely proportional to the squared atom-surface distance d. For larger separations, a numerical study of a three-layer system shows that the coherence length $l_{1/2}$ converges for thick intermediate layers to roughly the atom-surface distance d.

The results obtained in this Chapter are in agreement with previous work carried out on the coherent transport of matter waves by Henkel *et al.* [47, 48]. Instead of working with the coherence function, Henkel and co-workers formulate a transport equation for the atomic density matrix and include the fluctuating environment via the magnetic noise spectrum. Here, the consistent quantization of the electromagnetic field in dielectric matter allows the derivation of the spatially

non local function using a first-principles approach.

Finally, the possibility to express the spatial decoherence rate in terms of experimental parameters, such as lifetime, lateral separation and atom-surface distance, is important in quantum information processing. The results presented in this Chapter may prove useful when the decoherence rate needs to be maintained within a tolerance rate. In quantum information processing, spatial superpositions are used to encode quantum information or to generate entanglement. In such cases, a full quantum control over the atomic state is required which can be achieved by properly tailoring lateral separations and atom-surface distances.

Outlook

The framework adopted in this Chapter is quite general and can be easily extended to other decoherence phenomena by choosing the proper interaction Hamiltonian. Several implementations of quantum information processing rely on the resonant dipole-dipole interaction between two atomic qubits [28, 31, 34, 36, 159]. Two

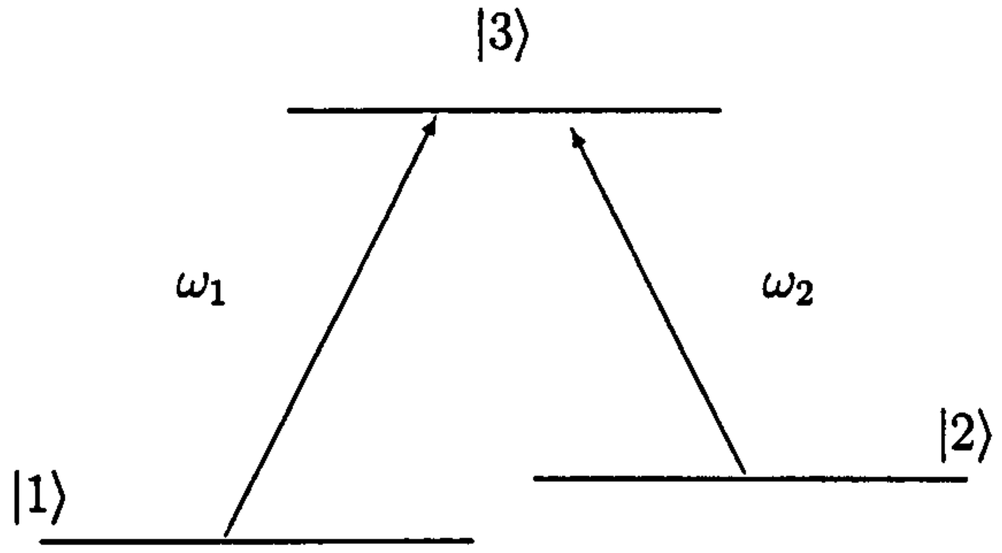

Figure 4.9: Schematic representation of a lambda system for a three-level atom, where the states $|1\rangle$ and $|2\rangle$ play the role of qubits. Fluctuating electromagnetic fields can induce transitions between those states and the decoherence of their superposition.

hyperfine states are chosen as qubits as shown in Fig. 4.9, and their coupling via Raman transition is the fundamental tool to realize quantum gates. Near field noise can perturb the coherence properties of a superposition of those states by inducing Raman transitions.

A suitable formulation of the coupling can be done by following Dung *et al.* [160] and distinguishing between the on-resonant and off-resonant interaction. An effective interaction Hamiltonian needs to be derived and the corresponding density matrix equation will contain information about the coherence properties of the system.

This system has been studied experimentally and for careful choice of the two states, the superposition state has been shown to be quite robust against thermal magnetic near field noise [32]. Coherence lifetimes longer that 1 s have been measured at distances as small as $d = 5\mu$m from the chip surface. Ramsey oscillations were observed as a function of d and the coherence lifetime appeared not to show a dependence on the atom-surface distance. However, amplitude and phase fluctuations of the interference signal were reported that can still be attributed to magnetic field fluctuations. The investigation of the lambda system presented above is then particularly interesting and may prove useful to understand the origin of phase noise in typical experimental realizations.

5

Vortex noise in superconducting atom chips

An atom close to a dielectric or metallic surface experiences magnetic field fluctuations arising from thermally-induced noise currents. The origin of those noise currents is connected with the finite resistivity and the skin depth of the substrate. As seen in Sec. 1.3, the spin-flip lifetime τ depends on physical parameters such

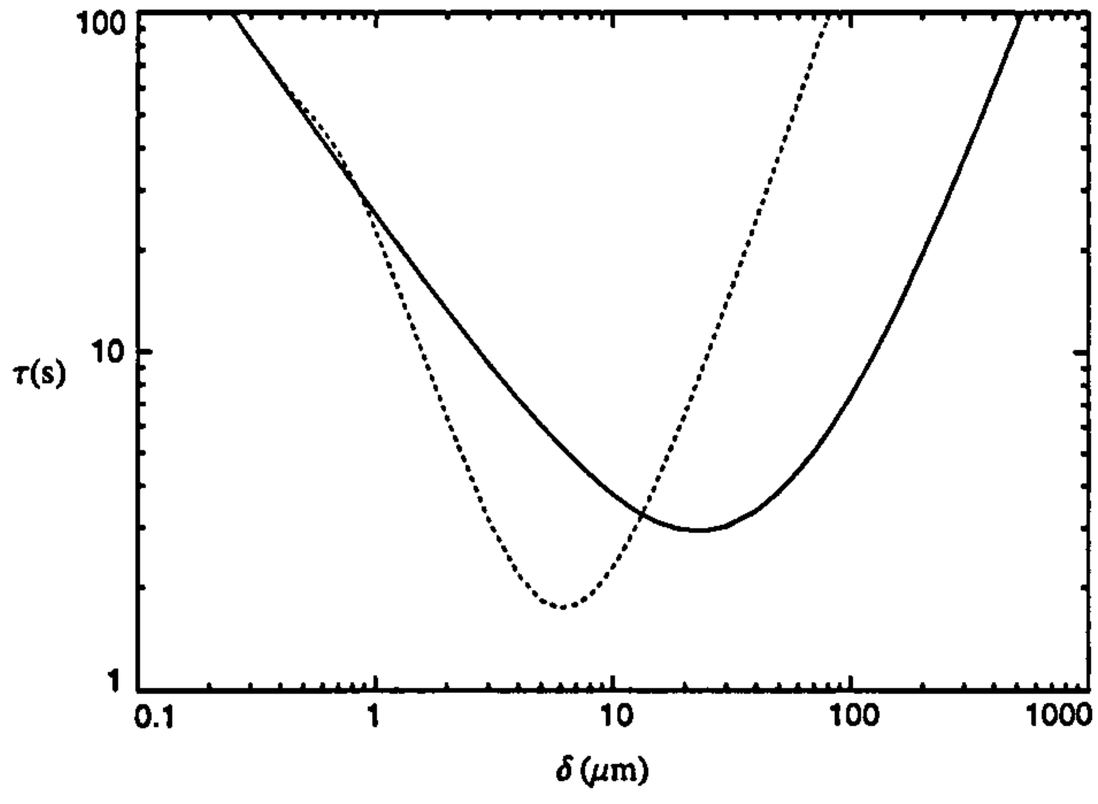

Figure 5.1: Spin-flip lifetime τ as a function of the skin depth δ, from [50]. Two different thicknesses h are considered: infinitely thick surface (solid line); 1-μm-thick surface (dotted line). The atom is located at a distance of 50 μm from the surface, the transition frequency is $\omega = 560$ kHz, and the temperature is 300 K.

as the skin depth δ, the thickness of the substrate h and the distance from the surface d. The expression of τ as a function of these parameters has been derived

by Scheel *et al.* in [50], and in Fig. 5.1 their plot is shown for a planar substrate (solid line) and a 1-μm-thick surface (dotted line).

The lifetime τ takes the highest values either for skin depths δ much bigger or much smaller than the atom-surface distance. In particular, small skin depths are of great interest, and superconductors are the most likely materials to exhibit this property. A more detailed analysis shows that superconductors may prove useful to achieve longer spin-flip lifetimes while maintaining small trapping distances [50]. Recent experimental realizations [161,162] show that neutral atoms can be trapped near superconducting surfaces. The lifetimes obtained are similar to the ones obtained by Jones *et al.* [8] at higher temperatures which indicates the feasibility of superconducting atom chips. A significant increase of the lifetimes is expected after straightforward technical improvements such as using different lithographic techniques which would allow wires bearing an higher current density.

As the resistance of a superconductor is ideally zero, there should be no thermally-induced noise and the cryogenic temperature will help reduce heating and background collisions. However, most practical applications of superconductivity involving ac currents demonstrate that dissipation phenomena can take place in superconductors [163–166]. Theoretical estimations of the spin-flip lifetime have been presented by Scheel *et al.* in [50], and by Skagerstam *et al.* in [82]. The order of magnitude obtained depends strongly on the theoretical approach used to describe the optical conductivity of the superconducting substrate. As highlighted in [83], a correct description of the problem and a realistic calculation of the conductivity require an elaborated theoretical framework, the Eliashberg theory [167], accounting for dissipative effects associated with the emission and absorption of phonons.

The approaches mentioned above apply to three dimensional superconducting materials, while in microtraps thin films are normally used. Thin superconducting films can be regarded as two-dimensional (2D) systems and fluctuations resulting from bulk losses seem to be negligible [82] such that only 2D effects need to be

considered. The dominant noise source in thin superconducting films is given by vortex motion. This suggests the possibility to probe the dynamics of vortices by looking at the atom's relaxation time. Instead of going into the theory of thin superconducting films, this Chapter presents an estimation of spin-flip lifetime of an atom near a superconducting film by referring to the experimental data obtained by Shaw *et al.* in [88].

The structure of this Chapter is the following. In Section 5.1, a brief introduction to superconductors and a review of the most important properties is presented referring to [163–166] with particular focus on vortex dynamics. In Section 5.2, the possibility of studying vortex noise with cold atoms is addressed.

5.1 Superconductivity

5.1.1 Zero resistance

The phenomenon of superconductivity was discovered in 1911 by H. Kamerlingh-Onnes while investigating the residual resistance of metals at low temperatures. He found that the resistance of a mercury sample fell to zero at a temperature of approximately 4 K. Below a certain temperature, called the transition temperature T_C, the resistance drops below the sensitivity limit of the equipment and is no longer detected. However, this is not a definitive proof of superconductivity as it is impossible, in principle, to prove experimentally that the resistance has exactly zero value. Instead only an upper limit of the resistance of the superconductor can be determined.

In metals, the conduction electrons move freely and are accelerated in an applied electric field. After a certain time τ, they collide with atoms and lose the energy gained from the electric field. The high conductivity in metals is then due to the existence of free carriers interacting with the lattice of the metallic crystal. With the increase in temperature, the atomic vibrations in the lattice become more pronounced, in contrast to 0 temperature where you don't have this effect,

and the probability of collision of the electrons with the atoms increases which leads to an increase in the resistance. In this framework, it is incomprehensible how the energy exchange with the crystal lattice by means of collisions abruptly stops in a very small temperature interval around T_C. An intuitive explanation to the zero resistance behavior is provided by the two-fluid model developed by the brothers F. and H. London in 1935 and reviewed briefly here. Only later with the advent of the Ginzburg-Landau theory in 1950, the conductivity with zero electronic resistance is understood in terms of a collective quantum phenomenon, a coherent matter wave that propagates through the superconductor without any friction. A microscopic theory of superconductivity arrived later in 1957 with Bardeen, Cooper and Schrieffer (BCS) which explains from first principles the superconducting properties by looking at things on a microscopic scale. The BCS theory is not presented here as it is not needed to explained the work reported.

Two-fluid model

The two-fluid model is a phenomenological theory describing the electrodynamics of a superconductor by assuming that two types of conduction electrons, normal electrons and superconducting ones, coexist during the superconducting phase. Below the transition temperature T_C, part of the electrons behave as super-electrons and their number density is denoted by $n_s(T)$. They move through the metal without resistance and are governed by the first London equation

$$\frac{\partial \mathbf{j}_s}{\partial t} = \varsigma \mathbf{E}, \tag{5.1}$$

where ς is a constant depending on the superconducting material. The normal electrons with number density $n_n(T)$ continue to act as if subject to a finite resistivity and obey to the usual Ohm's law

$$\mathbf{j}_n = \sigma_n \mathbf{E}. \tag{5.2}$$

The total density of conduction electrons at temperature T is $n_s(T) + n_n(T) = n_0$ and the total current $\mathbf{j} = \mathbf{j}_n + \mathbf{j}_s$ is the sum of the supercurrent of Eq. (5.1) and the normal current of Eq. (5.2). At $T = 0$ K only superconducting electrons are present, $n_s(0) = n_0$, while at temperatures above the transition temperature T_c only normal carriers appear, $n_n(T > T_c) = n_0$.

The parameter ς appearing in Eq. (5.1) is defined by London as

$$\varsigma = \frac{n_s(T)e^2}{m}, \tag{5.3}$$

and the distance inside the surface of the superconductor over which an external magnetic field is screened out to zero is called penetration depth of the superconductor and was defined by London as

$$\lambda_L = 1/(\mu_0 \varsigma)^{1/2}. \tag{5.4}$$

The current carried by the flow of super electrons is assumed to short circuit the current arising from the flow of normal electrons, causing the resistance to disappear.

5.1.2 Ideal Diamagnetism

The vanishing of the electrical resistance below a critical temperature T_C, is not the only unusual property of superconductors. An externally applied magnetic field can be expelled from the interior of superconductors except for a thin outer layer (an effect which is called ideal diamagnetism or Meissner-Ochsenfeld effect), or superconductors can concentrate the magnetic field in the form of flux tubes. The ideal magnetism of superconductors was discovered by Meissner and Ochsenfeld in 1933 and it is considered the fundamental proof for a material to be superconducting.

Ideal diamagnetism only exists within a finite range of magnetic fields and temperatures. One finds that there are two different types of superconductors:

- Type-I superconductors expel the magnetic field up to a maximum value H_C, referred to as the critical field, and for larger fields superconductivity breaks down.

- Type-II superconductors show ideal diamagnetism for magnetic fields below a so-called "lower critical magnetic field" H_{C1}. Superconductivity is destroyed for magnetic fields larger than a so-called "upper critical magnetic field" $H_{C2} > H_{C1}$. For values of the applied field such that $H < H_{C1}$, the superconductors show the Meissner effect. However, for the case $H > H_{C1}$, the magnetic field starts entering the superconductor. In this regime, often referred to as "Shubnikov phase" or "mixed state", the magnetic field penetrates the superconducting substrate and a system of flux lines, known as Abrikosov vortices, is generated. A more accurate treatment is based on the Ginzburg-Landau theory that shows that, on a length scale ξ_{GL} (known as the Ginzburg-Landau coherence length), superconductivity vanishes as one approaches the vortex axis.

The Ginzburg Landau theory

The Ginzburg-Landau (GL) theory was originally introduced as a phenomenological theory describing the passage from the normal metallic state to the superconducting state in terms of a thermodynamic phase transition. It starts from the argument that the normal-superconducting transition in the absence of a magnetic field can be described as a second-order phase transition. Landau had developed a theory for such transitions. The theory defines a parameter, called order parameter, which (during the superconducting phase) increases from 0 at T_C, up to the value 1 at $T = 0$. Ginzburg and Landau introduced a function $\Psi(\mathbf{r})$ as the order parameter to describe the superconducting state. The quantity $|\Psi(\mathbf{r})|^2$ is interpreted as the density of the superconducting charge carriers $n_s(T)$ and it must approach zero for $T \rightarrow T_C$.

Two are the characteristic lengths of the Ginzburg-Landau theory: the Lon-

don penetration length λ_L and the Ginzburg-Landau coherence length ξ_{GL}. To understand the meaning of the coherence length ξ_{GL}, consider a superconductor extending in the x direction from $x = 0$ to $x \to \infty$, then

$$\Psi(x) = \tanh(x/\sqrt{2}\xi_{GL}). \tag{5.5}$$

According to Eq. (5.5), $\Psi(x)$ first increases linearly from zero, and then approaches the limiting value of 1 in the superconductor. The coherence length ξ_{GL} can be then interpreted as the characteristic length within which the order parameter Ψ changes. Depending on the superconducting material, this length ranges between a few and a few hundred nanometers and similarly to the London penetration depth, is temperature dependent.

The ratio

$$\kappa = \frac{\lambda_L}{\xi_{GL}} \tag{5.6}$$

is usually referred to as the Ginzburg-Landau parameter. Type-I and type-II superconductors are distinguished by the value of κ:

$$\text{type} - \text{I}: \quad \kappa < 1/\sqrt{2}, \tag{5.7}$$

$$\text{type} - \text{II}: \quad \kappa \geq 1/\sqrt{2}. \tag{5.8}$$

This discrimination is valid only near T_C. For $T < T_C$ and values of κ slightly larger than $1/\sqrt{2}$, there exists a transition into a state in which both the Meissner phase and the Shubnikov phase appear next to each other.

In the Shubnikov phase magnetic flux penetrates into the superconductor in the form of quantized flux lines or vortices. A vortex is described as a singularity of the order parameter Ψ. Each vortex carries a quantum flux

$$\Phi_0 = \frac{h}{2e} = 2.07 \times 10^{-7}\,\text{Wb},$$

or an integer number of the elementary flux quantum. The highest field is in

the vortex center and decreases towards the outside. The central core of normal material is surrounded by a region of radius λ_L within which magnetic flux and screening currents flowing around the core are present together. A stable state is reached for a triangular vortex lattice system with one flux quantum at each lattice site.

5.1.3 Thin superconducting layer

In a thin superconducting layer of thickness d the circulating currents around the vortex decay with a characteristic length $\lambda_{eff} = \lambda_L^2/d$ from the axis towards the outside, and for $d \ll \lambda_L$ the length λ_{eff} can become much larger than λ_L.

Due to thermal fluctuations, the vortices can move around their equilibrium lattice site without leaving it. If the fluctuations around the equilibrium site become comparable to the distance between the vortices, then vortices will leave their lattice site and melt into a vortex liquid. It turns out that for two-dimensional or one-dimensional systems these fluctuations can become sufficiently large to destroy the macroscopic wave function characterizing the superconducting state. This result was described by Hoenberg, Mermin and Wagner in Refs. [168, 169].

In the absence of an external magnetic field, positive and negative vortices will be generated spontaneously in equal numbers such that the average magnetization of the sample vanishes. If the vortices can move independently of each other, they result in dissipation and, hence, in a finite resistance. It is widely accepted that the zero-field transition in superconducting films of thickness less than the penetration length λ_L, is described by the Berezinskii-Kosterlitz-Thouless (BKT) theory [85–87, 170]. They studied this transition in detail associating the phase transition with the emergence of a topological disorder due to the pairing of vortices and antivortices.

The Kosterlitz-Thouless-Berezinskii theory

According to the Berezinskii, Kosterltz and Thouless (BKT) theory [85–87], there is a sharply defined temperature $T_{BKT} < T_C$ at which vortex pairs dissociate into a vortex plasma because of thermal fluctuations. Above T_{BKT}, there is an equilibrium population of unbound vortices, which gives a linear resistance shown to vary as $e^{-\text{const.}/\sqrt{T-T_{BKT}}}$.

Below the transition temperature T_{BKT}, the whole system is superconducting and phase coherence is established in the thin film. In this phase, vortices and antivortices, described as topological defects of the order parameter, are generated in pairs and are bound together. Thermal energy is not sufficient to allow the vortices to unbind and the density of free vortices is zero. If a magnetic field is applied perpendicular to the layer, free vortices appear with their orientation given by the applied field.

The BKT theory is well understood in superfluid helium films [171] and in superconducting transitions in arrays of Josephson junctions [172]. Indirect evidence of the BKT transition can be obtained by looking at the macroscopic properties of these systems, however, the microscopic origin of the transition has not been explained completely and atomic clouds appear to be well suited to test theories of many-body physics and detect individual vortices [173].

5.2 Vortex Noise

The aim of this Section is to address the possibility of detecting vortex noise with cold atoms trapped near a thin superconducting film. The estimations presented in the following Section have been guided by experimental data obtained by Shaw *et al.* [88].

The objective of their experiment was to study the vortex density fluctuations at the Berenzinskii-Kosterlitz-Thouless (BKT) transition in Josephson junction arrays, which were used as a model system of a two-dimensional superconductor.

Early experimental studies at the BKT transition involved electrical resistance and the application of an external force to the system. The transition to the resistive state takes place because of the dissociation of the vortex pairs due to thermal fluctuations. Therefore, external forces may induce pairs dissociation and affect the measurements. The best way to study the BKT transition is then to use a non-invasive probe.

Vortex dynamics at the BKT transition is typically studied by monitoring the superconductor surface with a superconducting quantum interference device (SQUID) [65]. A SQUID is a superconducting ring in which two Josephson junctions are integrated. A transport current flows along the ring and the maximum current oscillates as a function of the magnetic flux through the ring. A variation of the magnetic flux can be detected by measuring the voltage drop across the Josephson junction. This is a noninvasive probe because it does not affect the vortex behaviour while detecting magnetic flux variations. However, the noise processes which limit the measuring sensitivity of this device are numerous and complex. Some are intrinsic to the SQUID coil such as thermal noise, Nyquist voltage and current fluctuations associated with the normal state resistance, while others originate in the circuit associated with the coil [65]. Cold atoms are extremely sensitive to magnetic field variation and they may prove useful as a non-invasive measurement device of vortex dynamics as they can be positioned with high precision and their interaction with a magnetic field is well understood.

5.2.1 Magnetic flux noise

Vortex motion induces a change in the magnetic flux through the SQUID which is detected as an output current. A perpendicular and spatially homogeneous magnetic field B through a pick-up loop of area A is detected as a magnetic flux $\Phi = A\,B$. In the general case of an arbitrarily oriented and spatially inhomoge-

neous magnetic field $\mathbf{B}(\mathbf{r}, t)$, one must integrate over the area of the loop

$$\Phi(t) = \int_A d\mathbf{r}\, \mathbf{n} \cdot \mathbf{B}(\mathbf{r}; t), \tag{5.9}$$

where $\mathbf{n}$ is a unitary vector normal to the surface. For a pick-up loop placed parallel to a thin superconducting film, as schematically depicted in Fig. 5.2, only the perpendicular component of the magnetic field induces a current. The flux

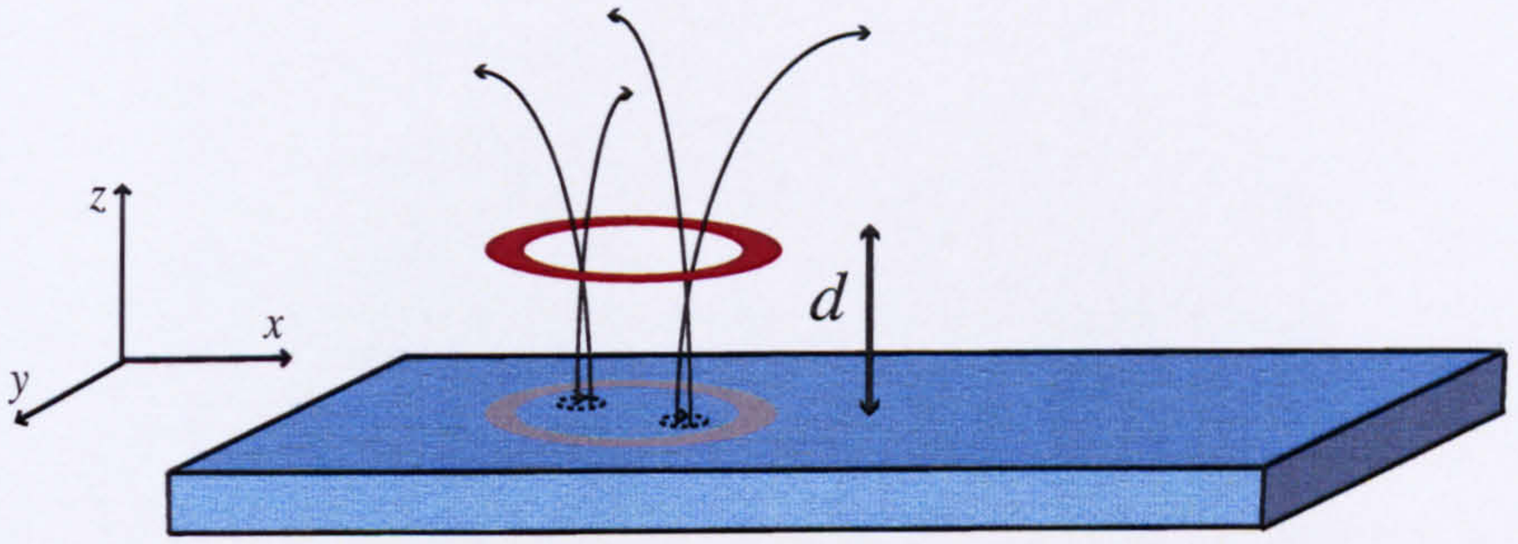

Figure 5.2: Schematic representation of the system geometry. A SQUID is placed at a distance d from a superconducting film. A magnetic flux variation is detected as a voltage in the SQUID.

correlation function in the time domain is then given by

$$C_\Phi(t) = \langle \Phi(t)\Phi(0) \rangle, \tag{5.10}$$

and the flux noise spectrum is defined as

$$\begin{aligned} S_\Phi(\omega) &= \int dt\, e^{-i\omega t} C_\Phi(t) \\ &= 2\pi \int_A d^2x\, d^2y\, \langle \hat{B}_z(\mathbf{x}, d; \omega) \hat{B}_z^\dagger(\mathbf{y}, d; \omega) \rangle, \end{aligned} \tag{5.11}$$

where $\hat{B}_z$ is the operator for the magnetic field component normal to the loop, $\mathbf{x}$ and $\mathbf{y}$ are vectors parallel to the plane of the surface and d the distance from the surface.

The experimental values of $S_\Phi(\omega)$ obtained in [88] are reported in Fig. 5.4. Shaw and co-workers measured the spectral density of flux noise at the BKT transition in a Josephson junction array. The array has dimensions of 1 mm × 1 mm and consists of niobium islands deposited on a copper film, as illustrated in Fig. 5.3(a). The SQUID used was a superconducting square with inner and outer dimensions $l_i = 180\,\mu$m and $l_o = 900\,\mu$m and was held at a distance $d = 100\,\mu$m from the array as depicted in Fig. 5.3(b). The spectral density of the magnetic flux

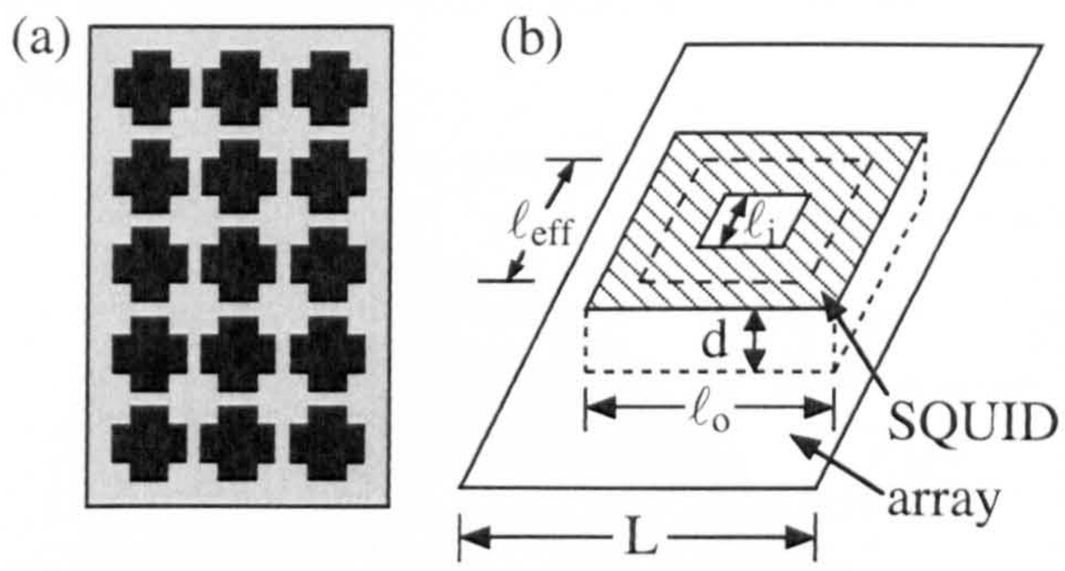

Figure 5.3: Reproduced from Ref. [88]. (a) Schematic representation of the array, the niobium islands are the cross shapes and the area between the crosses is copper. (b) Schematic representation of the SQUID at a distance d from the array and with inner and outer dimensions denoted by l_i and l_o and $l_{\text{eff}}^2 = l_i\, l_o$.

noise is plotted in Fig. 5.4 for 15 temperatures above the transition temperature T_{BKT}, but below the bulk transition temperature, as a function of frequency. The average separation between free vortices is described by the length parameter ξ and for a temperature $T \to T_{BKT}$, ξ diverges.

Thermal fluctuations perturb the equilibrium of the vortex density and the whole system relaxes through some local dynamic process. Therefore, a relaxation time τ (with corresponding frequency $f_\xi^{-1} \propto \tau$), can be defined as the time required for the disturbance of the vortex density to propagate across the distance ξ. If ξ diverges, which means that the average separation between vortices diverges, then the relaxation time τ (f_ξ^{-1}) diverges as well thereby signifying a critical slow down of the relaxation dynamics.

At a given temperature, two different regimes of the spectral density $S_\Phi(\omega)$ occur for $f < f_\xi$ and $f > f_\xi$. The spectral density $S_\Phi(\omega)$ appears to be white for $f < f_\xi$, while it scales as $1/f$ for $f > f_\xi$. The authors gave explanation for the two regimes in terms of the observation time scale compared with the time required for the disturbance to travel over the distance ξ. For $f < f_\xi$, the observation time scale is longer than the relaxation time τ and the system appears disordered, with a white spectral density. Instead, for $f > f_\xi$ the observation time is shorter than the relaxation time and the system appears to be critical. The difference between the two power spectra reflect the fundamental differences in the relaxation dynamics of the two phases.

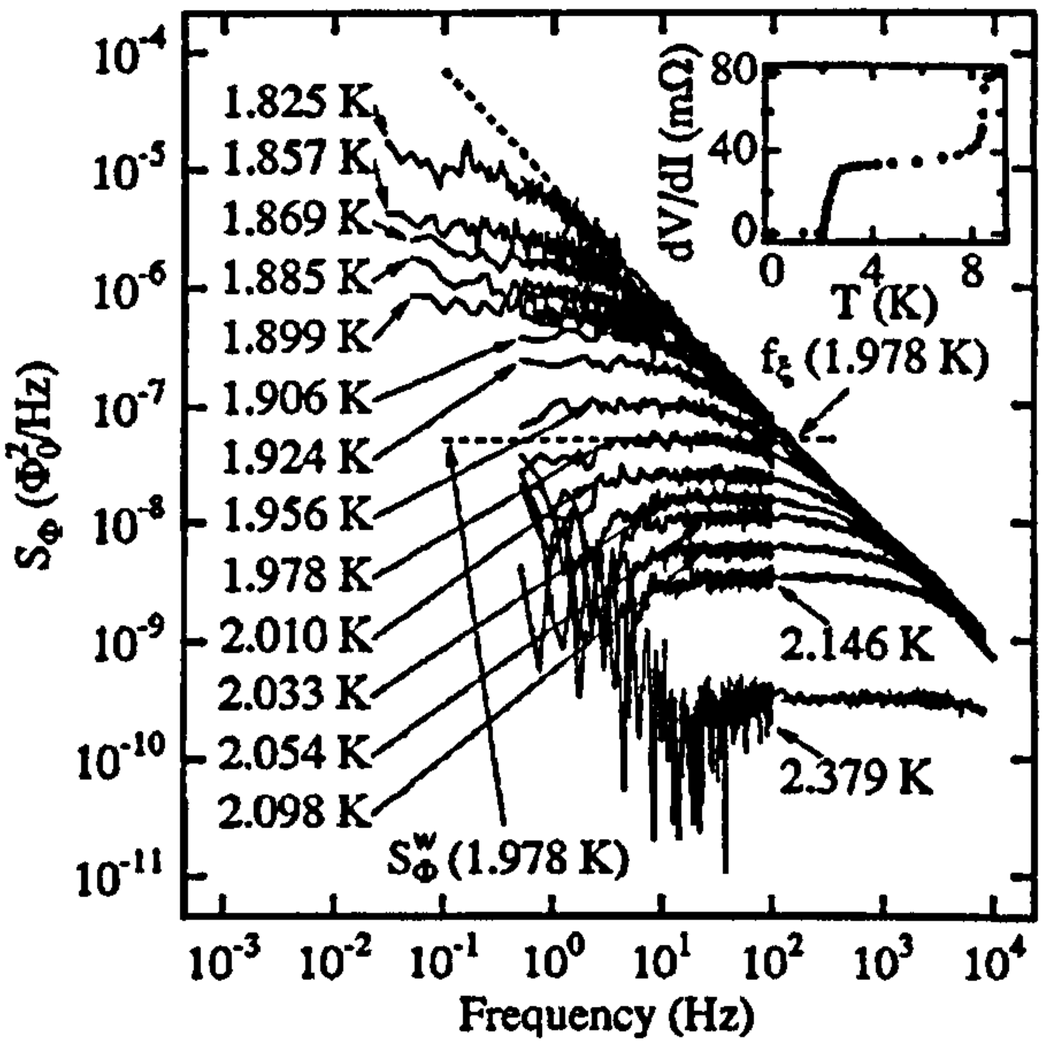

Figure 5.4: Reproduced from Ref. [88]. Spectral density of magnetic flux noise, $S_\Phi(f)$, versus frequency $f = \omega/2\pi$ for 15 temperatures above the Kosterlitz-Thouless-Berezinskii transition temperature. Dashed lines have slope -1 and 0.

5.2.2 Flux noise spectrum and spin flip rate

As shown in Chapter 2, the cross correlation function of the magnetic field at two distinct points $\mathbf{x}$ and $\mathbf{y}$ is proportional to the imaginary part of the Green function evaluated at the two positions. In thermal equilibrium, the integrand in Eq. (5.11)

can be written as

$$\langle \hat{B}_z(\mathbf{x}, d; \omega) \hat{B}_z^\dagger(\mathbf{y}, d; \omega) \rangle = \frac{\hbar \mu_0}{\pi} (\bar{n}_{\text{th}} + 1) \text{Im} \left[\overrightarrow{\nabla} \times \boldsymbol{G}(\mathbf{x}, d; \mathbf{y}, d; \omega) \times \overleftarrow{\nabla} \right]_{zz}, \quad (5.12)$$

where $\bar{n}_{\text{th}}$ is the mean thermal photon number, and the flux noise spectrum can be expressed as

$$S_\Phi(\omega) = 2\hbar\mu_0(\bar{n}_{\text{th}} + 1) \int_A d^2x\, d^2y\, \text{Im} \left[\overrightarrow{\nabla} \times \boldsymbol{G}(\mathbf{x}, d; \mathbf{y}, d; \omega) \times \overleftarrow{\nabla} \right]_{zz}. \quad (5.13)$$

The central idea of this work is to connect the spectral density $S_\Phi(\omega)$ with the spin-flip rate Γ_z

$$\Gamma_z = \frac{2\mu_0\mu_{12}^2}{\hbar} (\bar{n}_{\text{th}} + 1) \text{Im} \left[\overrightarrow{\nabla} \times \boldsymbol{G}(\mathbf{r}_A, \mathbf{r}_A, \omega) \times \overleftarrow{\nabla} \right]_{zz}, \quad (5.14)$$

where μ_{12} is the magnetic dipole matrix element corresponding to the transition between the initial and final Zeeman sublevels $|1\rangle$ and $|2\rangle$, $\mathbf{r}_A$ is the position of the atom and ω is the spin transition frequency. The spectral density of Eq. (5.13), and the spin-flip rate Γ_z of Eq. (5.14), are both proportional to the zz-component of the cross-correlation function of the magnetic field, i.e. the imaginary part of the double curl of the Green function. In physical terms, an atom trapped above a thin superconducting film experiencing the magnetic field of the vortices is subject to spin-flip transitions. The spin-flip lifetime measured experimentally is due to all the magnetic field components. Here, the quantization axis is taken along the x direction and the only nonzero spin matrix elements are $\langle 1|\hat{S}_{y,z}|2\rangle$. As a consequence, only the yy and zz components of $\text{Im} \left[\overrightarrow{\nabla} \times \boldsymbol{G}(\mathbf{r}_A, \mathbf{r}_A, \omega) \times \overleftarrow{\nabla} \right]$ are necessary. Symmetry considerations for the planar surface yield

$$\text{Im} \left[\overrightarrow{\nabla} \times \boldsymbol{G} \times \overleftarrow{\nabla} \right]_{xx} = \text{Im} \left[\overrightarrow{\nabla} \times \boldsymbol{G} \times \overleftarrow{\nabla} \right]_{yy} = 2\,\text{Im} \left[\overrightarrow{\nabla} \times \boldsymbol{G} \times \overleftarrow{\nabla} \right]_{zz},$$

which leads to the following relation: $\Gamma = 3/2\Gamma_z$.

Neglecting the contribution of the vacuum Green tensor and using the Weyl expansion for the scattering part of the Green tensor, as presented in Appendix B, allows Eq. (5.13) to be rewritten as

$$S_\Phi(\omega) = 2\hbar\mu_0(\bar{n}_{\rm th}+1)\mathrm{Im}\left[\int_A d^2x\, d^2y \int \frac{d^2k_\parallel}{(2\pi)^2}\, e^{i\mathbf{k}_\parallel\cdot(\mathbf{x}-\mathbf{y})}\, r_{12}^{TE}\, \frac{ik_\parallel^2}{2k_z} e^{2ik_z d}\right], \quad (5.15)$$

and Eq. (5.14) as

$$\Gamma_z = \frac{2\mu_0\mu_{12}^2}{\hbar}(\bar{n}_{\rm th}+1)\mathrm{Im}\left[\int \frac{d^2k_\parallel}{(2\pi)^2}\, r_{12}^{TE}\, \frac{ik_\parallel^2}{2k_z} e^{2ik_z d}\right], \quad (5.16)$$

where $k_z = \sqrt{\omega^2/c^2 - k_\parallel^2}$ and r_{12}^{TE} is the Fresnel reflection coefficient for s-polarized waves, whose electric vector is perpendicular to the plane of incidence. The structure of Eqs. (5.15)-(5.16) differs only by the integration over the area of the SQUID but some algebraic manipulation permits S_Φ to be written in terms of the integral appearing in Eq. (5.16), so that it can be related to Γ_z.

The integration is performed for a circular pick-up coil of radius R. After switching to polar coordinates, the integration is carried out by means of the following identity for Bessel functions

$$\int_0^{2\pi} d\varphi\, e^{i\mathbf{k}_\parallel\cdot(\mathbf{x}-\mathbf{y})} = 2\pi J_0(k)\,, \quad (5.17)$$

where $\mathbf{k}_\parallel\cdot(\mathbf{x}-\mathbf{y}) = k_\parallel l\cos\varphi$ with $l = |\mathbf{x}-\mathbf{y}|$ and $J_0(k)$ is the zeroth-order Bessel function. The integration over the radial variables is performed by using the Bessel function integration properties

$$\int_0^R dl\, l J_0(kl) = \frac{R}{k} J_1(kR)\,, \quad (5.18)$$

permitting Eq. (5.15) to be written as

$$S_\Phi(\omega) = 2\hbar\mu_0(\bar{n}_{\rm th}+1)\,{\rm Im}\left[(2\pi)^3\int\frac{dk}{(2\pi)^2}\,k\,\frac{R^2J_1^2(kR)}{k^2}\,r_{12}^{TE}\,\frac{ik^2}{2k_z}e^{2ik_zd}\right]. \quad (5.19)$$

The factor $A^2 = (\pi R^2)^2$, which is the squared area of the loop, can be extracted from Eq. (5.19) which finally leads to

$$S_\Phi(\omega) = \frac{16\pi A^2}{R^2}\hbar\mu_0(\bar{n}_{\rm th}+1)\,{\rm Im}\left[\int\frac{dk}{(2\pi)^2}\,k\,J_1^2(kR)\,r_{12}^{TE}\,\frac{i}{2k_z}e^{2ik_zd}\right]. \quad (5.20)$$

The separation z between the trapped atoms and the surface (typically 1-100 μm) is very small when compared with the spin-flip transition wavelength in free space. Similarly to Chapter 4, the transition wavelength $\lambda = c/(2\pi\omega)$ (typically 3 cm-300 m) is the largest length scale in the system such that the integral over k is dominated by the region in which $k^2 \gg \omega^2/c^2$ and the approximation $k_{1z}^2 \approx -k^2$ holds, permitting to simplify Eq. (5.20) even further as

$$S_\Phi(\omega) = \frac{16\pi A^2}{R^2}\hbar\mu_0(\bar{n}_{\rm th}+1)\int\frac{dk}{(2\pi)^2}\,J_1^2(kR)\,{\rm Im}\left[r_{12}^{TE}\right]\,\frac{e^{-2kd}}{2}. \quad (5.21)$$

The same approximation allows the spin-flip rate of Eq. (5.16) to be written as

$$\Gamma_z = \frac{4\pi\mu_0\mu_{12}^2}{\hbar}(\bar{n}_{\rm th}+1)\int\frac{dk}{(2\pi)^2}\,k^2\,{\rm Im}\left[r_{12}^{TE}\right]\,\frac{e^{-2kd}}{2}, \quad (5.22)$$

which is similar to Eq. (5.21) except for an additional factor k^2 in the integrand. The integration over k cannot be done in closed form. In order to express Eq. (5.21) as a function of the integral in Eq. (5.22), the Bessel function is expanded in power series in k such that

$$J_1^2(p) = \left(\sum_{j=0}^{\infty}c_j\,p^{2j+1}\right)^2 = \sum_{q=0}^{\infty}\sum_{l=0}^{q}c_l\,c_{q-l}\,p^{2q+2}, \quad (5.23)$$

with

$$c_j = \frac{(-1)^j}{2^{2j+1}j!(j+1)!}. \quad (5.24)$$

The sum over l in Eq. (5.23) can be simplified by using the Gamma function $\Gamma(n) = (n-1)!$. Once substituted in Eq. (5.23) this gives

$$J_1^2(p) = p^2 \sum_{q=0}^{\infty} C_q \, p^{2q}, \tag{5.25}$$

with

$$C_q = \frac{(-1)^q \Gamma(q+3/2)}{\sqrt{\pi}\,\Gamma(q+1)\Gamma(q+2)\Gamma(q+3)}, \tag{5.26}$$

and Eq. (5.21) can then be written as

$$S_\Phi(\omega) = 16\pi A^2 \hbar \mu_0 (\bar{n}_{\rm th}+1) \sum_{q=0}^{\infty} C_q R^{2q} \int \frac{dk}{(2\pi)^2} k^2 k^{2q} \, \mathrm{Im}\left[r_{12}^{TE}\right] \frac{e^{-2kd}}{2}. \tag{5.27}$$

The factor k^{2q} in Eq. (5.27), which results from the expansion of Bessel function, can be converted into a differentiation with respect to the atom-surface distance d. The replacement $k \equiv -\frac{1}{2}\frac{\partial}{\partial d}$ allows the flux noise spectrum to be written as

$$\begin{aligned} S_\Phi(\omega) \;\; = \;\; & 16\pi A^2 \hbar \mu_0 (\bar{n}_{\rm th}+1) \sum_{q=0}^{\infty} C_q \left(\frac{R}{2}\right)^{2q} \\ & \frac{\partial^{2q}}{\partial d^{2q}} \left(\int \frac{dk}{(2\pi)^2} k^2 \, \mathrm{Im}\left[r_{12}^{TE}\right] \frac{e^{-2kd}}{2} \right), \end{aligned} \tag{5.28}$$

and it is finally possible to obtain the following expression

$$S_\Phi(\omega) \;\; = \;\; \frac{4A^2\hbar^2}{\mu_{12}^2} \sum_{q=0}^{\infty} C_q \left(\frac{R}{2}\right)^{2q} \frac{\partial^{2q}}{\partial d^{2q}} \Gamma_z, \tag{5.29}$$

which constitutes the main result of this Chapter. In the asymptotic regimes reported in Eq. (1.40) from Scheel *et al.* [50], Γ_z can be expressed as a monomial $\Gamma_z \propto d^{-n}$ with respect to the atom-surface distance d. The derivatives in Eq. (5.29) then become

$$\frac{\partial^{2q}}{\partial d^{2q}} \Gamma_z = \frac{(n+2q-1)!}{(n-1)!} \frac{\Gamma_z}{d^{2q}}, \tag{5.30}$$

and performing the summation over q in Eq. (5.29), one obtains

$$S_\Phi(\omega) = \frac{\hbar^2 A^2}{\mu_{12}^2}\Gamma_z \, {}_3F_2\left[\left\{\frac{3}{2}, \frac{n+1}{2}, \frac{n}{2}\right\}, \{2,3\}, -\frac{R^2}{d^2}\right], \tag{5.31}$$

where ${}_3F_2$ denotes a hypergeometric function. Flux noise spectrum and spin-flip rate are then related via Eq. (5.31), which is the main result of this Chapter. Physical parameters such as atom-surface distance, skin depth of the substrate and SQUID dimensions enter in this relation via the argument $(R/d)^2$ of the hypergeometric function and the power law associated with the spin-flip rate.

Comparison with experimental geometry

In order to compare Eq. (5.31) with real geometries, the hypergeometric function is approximated for two limiting situations: $R \ll d$ when the size of the loop is small compared to the distance from the surface, or the opposite limit $R \gg d$ when the loop is located very close to the superconducting surface, as illustrated in Fig. 5.5.

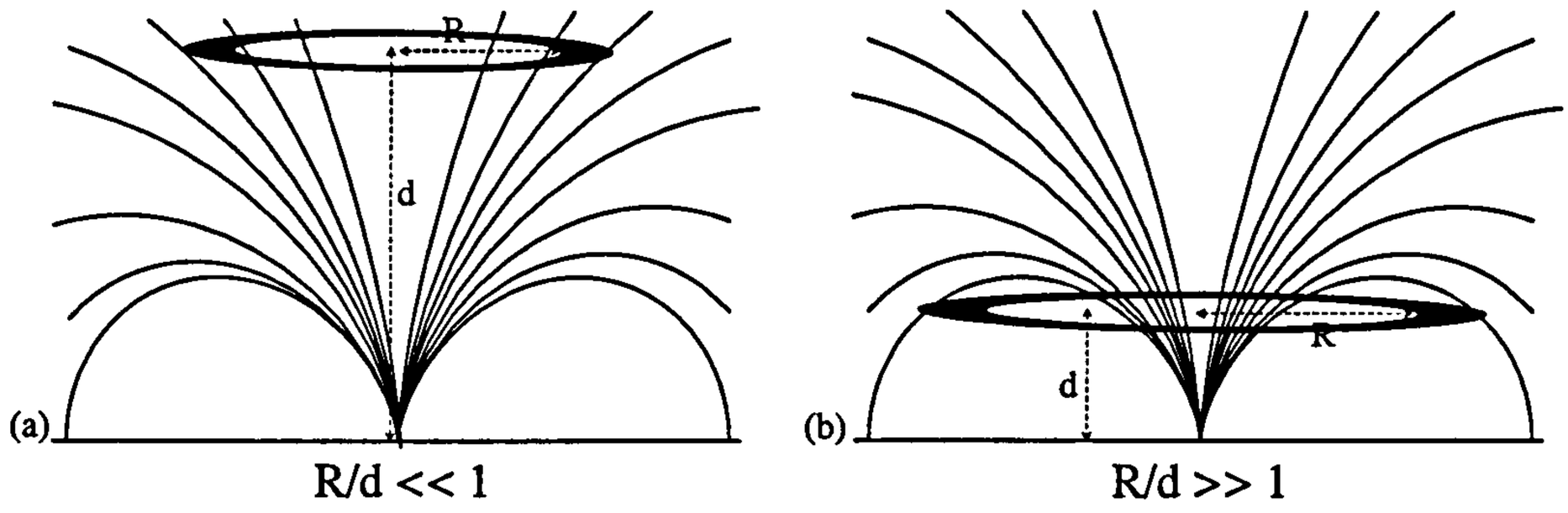

Figure 5.5: Schematic representation of the geometry of the system. A circular SQUID of radius R is located at a distance d from the surface and it measures any variation in the magnetic flux. In (a) and (b), the magnetic field lines of a single vortex are illustrated for two limiting situations: in the limit $R/d \ll 1$ (a), corresponding to the case of a small pick-up loop located far from the surface, and in the opposite limit $R/d \gg 1$ (b), corresponding to the case of a pick-up loop located very close to the surface such that its radius is greater that the height.

In the limit $R/d \ll 1$, the hypergeometric function in Eq. (5.31) can be ap-

proximated [174] by

$$ {}_3F_2\left[\left\{\frac{3}{2},\frac{n+1}{2},\frac{n}{2}\right\},\{2,3\},-\frac{R^2}{d^2}\right] \overset{R\ll d}{\approx} 1-\frac{n(n+1)}{16}\frac{R^2}{d^2}+\mathcal{O}\left(\frac{R^4}{d^4}\right), \quad (5.32) $$

which means that the largest contribution to the flux noise spectrum is proportional to the squared area of the pick-up loop times the spin-flip rate. In this limit, the loop is small enough to sample only the local magnetic field. However, the flux measurements reported in [88] were made in the opposite limit $R/d \gg 1$, with a large pick-up loop located very close to the surface. Assuming a power law $\Gamma_z \propto 1/d^4$ (valid in the case $\delta \ll d$, with δ being the penetration depth of the substrate material [45,47,50,51]), the following limiting behaviour is obtained

$$ \begin{aligned} {}_3F_2\left[\left\{\frac{3}{2},\frac{5}{2},2\right\},\{2,3\},-\frac{R^2}{d^2}\right] &\equiv {}_2F_1\left[\frac{3}{2},\frac{5}{2},3,-\frac{R^2}{d^2}\right] \\ &\overset{R\gg d}{\approx} \frac{16}{3\pi}\frac{d^3}{R^3}+\frac{4}{3\pi}\frac{d^5}{R^5}\left[5+6\log\frac{d}{4R}\right]+\mathcal{O}\left(\frac{d^7}{R^7}\right). \end{aligned} \quad (5.33) $$

The presence of the factor $(d/R)^3$ in the limit $R \gg d$, (and its absence in the opposite limit) can be understood by comparing the radius of the pick-up loop with the coherence length of the magnetic field. In Section 4.2, the lateral separation $l_{1/2}$ has been regarded as a measure of the magnetic field coherence length. It has been shown that $l_{1/2}$ drops off over a distance d from the surface comparable with the skin depth δ, which for niobium is of the order of a few μm. In the experiment considered here, the pick-up loop radius is of the order of 200 μm and then much bigger than both δ and $l_{1/2}$. The spectrum of the magnetic field is not constant within the area of the coil in the limit $R \gg d$ as it decays over a distance $\simeq \delta$. The length scales involved are then R/δ and d/δ which explain the dependence on the ratio R/d in the spectral density. On the other hand, it is now clear that in the limit $R \ll d$ the loop is small compared to the magnetic field coherence length and the measured flux does not vary over the loop's radius.

5.2.3 Spin-flip relaxation time

In order to carry out a quantitative comparison with the experimental data, the transition between Zeeman sublevels $|1\rangle = |F = 2, m_F = 2\rangle$ and $|2\rangle = |F = 2, m_F = 1\rangle$ of a ground-state rubidium atom is considered. The corresponding magnetic dipole matrix element is $\mu_{12} = g_S \mu_B \langle 1|\hat{S}_z|2\rangle = \mu_B/2$ and Eq. (5.31) becomes

$$S_\Phi(\omega) = \frac{16\, m_e^2}{e^2}\, \Gamma_z A^2 f(d, R)\,, \tag{5.34}$$

where e and m_e are the charge and mass of the electron and $f(d, R)$ denotes the function in Eq. (5.33). The flux measurements reported in Ref. [88] and reproduced in Fig. 5.4, are expressed in terms of the flux quantum $\Phi_0 = h/(2e)$ as $S_\Phi(\omega) = x\Phi_0^2$ where x is the proportionality factor with units of Hz. This gives

$$\Gamma_z = x\, \frac{\pi^2 \hbar^2}{16\, m_e^2 A^2 f(d, R)} \overset{d \ll R}{\simeq} x\, \frac{3\pi^3 \hbar^2}{256\, m_e^2 A^2} \left(\frac{R}{d}\right)^3 . \tag{5.35}$$

The pick-up loop used to measure the flux had an area $A = l_{\text{eff}} \approx 2\,10^{-7}\,\text{m}^2$ and a ratio $R/d \geq 2.3$, giving a spin-flip rate of

$$\Gamma_z \geq x\, 2\,10^6\,\text{s}^{-1}.$$

Clearly, it makes no physical sense to speak of a spin-flip lifetime $\tau = \Gamma_z$, as the lifetime observed experimentally is due to all the magnetic field components. However, the total spin-flip rate Γ can be obtained from Γ_z via the relation $\Gamma = 3/2\,\Gamma_z$ as seen before, hence they have the same order of magnitude. Spin-flip transition frequencies are usually above 10 kHz and for those frequencies the value of x shown in Fig. 5.4 is below 10^{-9} Hz. It corresponds to a spin-flip rate $\Gamma_z \geq 2\,10^{-3}\,\text{s}^{-1}$ and to a spin-flip lifetime greater than $\tau_1 = 1/\Gamma \simeq 500\,\text{s}$. This means that atoms can be trapped above a superconducting surface long enough to be manipulated and this result is particularly interesting when combined with the fact that the heating noise is almost completely suppressed in a cryostat.

Given the rather long relaxation time τ_1, cold atomic clouds may provide an useful way to image the vortices. The typical vortex separation is of the order of $\xi \simeq 2\,\mu$m and at a distance from the surface $d \simeq \xi$, the field of each vortex is of the order of $\Phi_0/(\pi\xi^2) \simeq 1$ G. The effect of the vortex motion is to alter the trapping potential and this provokes changes in the density distribution of the atoms. If an atomic cloud can be held close to the surface long enough to study its density distribution, the motion of a single vortex would be ideally reflected in a pattern on the atomic cloud.

5.2.4 Dephasing time

Additional information on vortex dynamics can be obtained by looking at the phase noise induced between two Zeeman sublevels $|1\rangle$ and $|2\rangle$. To study the coherence of the two Zeeman sublevels, a coherent superposition $|1\rangle + |2\rangle$ is prepared and the phase between $|1\rangle$ and $|2\rangle$ evolves coherently with their energy difference. However, the interaction with a fluctuating environment introduces an additional relative phase factor φ that evolves incoherently and leads to dephasing, or phase noise. The extra phase factor $e^{i\varphi}$ between the levels $|1\rangle$ and $|2\rangle$ due to the fluctuations of the magnetic field, can be written as

$$\varphi(T) = \frac{(\mu_{22} - \mu_{11})}{\hbar} \int_0^T dt\, \hat{B}_z(t), \tag{5.36}$$

with $\hat{B}_z(t)$ the normal field component and $\mu_{jj} = g_S \mu_B \langle j|\hat{S}_z|j\rangle$. The phase variance is given by $\sigma[\varphi]^2 = \langle\varphi^2\rangle - \langle\varphi\rangle^2$, but $\langle\varphi\rangle = 0$ as the average over the field fluctuations is zero and this leads to

$$\sigma[\varphi(T)]^2 = \frac{(\mu_{22} - \mu_{11})^2}{\hbar^2} \int_0^T dt \int_0^T dt' \langle \hat{B}_z(t)\hat{B}_z(t')\rangle\,. \tag{5.37}$$

Again, only the normal contribution of the magnetic field is considered in order to give an estimation of the dephasing time τ_2 based on existent experimental data.

Equation (5.37) is proportional to the correlation function of the magnetic field. The phase variance can be easily related to the spin flip rate Γ_z by relating $\hat{B}_z(t)$ and $\hat{B}_z(\omega)$ via the Fourier transform

$$\hat{B}_z(t) = \int_0^\infty d\omega \left[\hat{B}_z(\omega)e^{-i\omega t} + \text{h.c.}\right]. \tag{5.38}$$

The phase variance can then be expressed as

$$\begin{aligned}\sigma[\varphi(T)]^2 &= \frac{(\mu_{22}-\mu_{11})^2}{\hbar^2}\int_0^T dt\int_0^T dt'\int_0^\infty d\omega\int_0^\infty d\omega' \\ &\left\{\langle\hat{B}_z(\omega)\hat{B}_z^\dagger(\omega')\rangle e^{-i\omega t+i\omega' t'} + \langle\hat{B}_z^\dagger(\omega)\hat{B}_z(\omega')\rangle e^{i\omega t-i\omega' t'}\right\}. \end{aligned}\tag{5.39}$$

Combining together Eq. (5.12) and Eq. (5.14) allows one to write

$$\langle\hat{B}_z(\omega)\hat{B}_z^\dagger(\omega')\rangle = \delta(\omega-\omega')\frac{\hbar^2}{2\pi\mu_{12}^2}\Gamma_z(\omega, T=0), \tag{5.40}$$

and

$$\langle\hat{B}_z^\dagger(\omega)\hat{B}_z(\omega')\rangle = \delta(\omega-\omega')\frac{\hbar^2}{2\pi\mu_{12}^2}\frac{\bar{n}_{\text{th}}}{\bar{n}_{\text{th}}+1}\Gamma_z(\omega, T=0), \tag{5.41}$$

such that

$$\langle\hat{B}_z^\dagger(\omega)\hat{B}_z(\omega')\rangle = \langle\hat{B}_z(\omega)\hat{B}_z^\dagger(\omega')\rangle\frac{\bar{n}_{\text{th}}}{\bar{n}_{\text{th}}+1}. \tag{5.42}$$

The integration over t and t' gives

$$\int_0^T dt\int_0^T dt' e^{\pm i\omega(t-t')} = 2\,\frac{1-\cos\omega T}{\omega^2}, \tag{5.43}$$

leading to

$$\sigma[\varphi(T)]^2 = \frac{(\mu_{22}-\mu_{11})^2}{2\pi\mu_{12}^2}\int_0^\infty d\omega\,\Gamma_z(\omega)\left(1+\frac{\bar{n}_{\rm th}}{\bar{n}_{\rm th}+1}\right)\frac{2(1-\cos\omega T)}{\omega^2}. \tag{5.44}$$

Note that the Dirac delta function can be defined as

$$\delta(\omega_0-\omega) = \frac{2}{\pi}\lim_{T\to\infty}\frac{2(1-\cos[(\omega_0-\omega)T])}{(\omega_0-\omega)^2}, \tag{5.45}$$

and given any function $f(\omega)$ of ω non-singular at $\omega=\omega_0$, it satisfies the integral relation

$$f(\omega_0) = \frac{2}{\pi}\lim_{T\to\infty}\int_{\omega_1}^{\omega_2} d\omega f(\omega)\frac{2(1-\cos[(\omega_0-\omega)T])}{(\omega_0-\omega)^2}, \tag{5.46}$$

where $\omega_1 < \omega_0 < \omega_2$. For large enough observation times T, the integral in Eq. (5.44) can thus be rewritten as [175]

$$\begin{aligned}\sigma[\varphi(T)]^2 &= \frac{(\mu_{22}-\mu_{11})^2}{2\mu_{12}^2}\int_0^\infty d\omega\,\Gamma_z(\omega)\left(1+\frac{\bar{n}_{\rm th}}{\bar{n}_{\rm th}+1}\right)T\delta(\omega)\\ &= \frac{(\mu_{22}-\mu_{11})^2}{2\mu_{12}^2}\Gamma_z(0)T.\end{aligned} \tag{5.47}$$

The result of integration in Eq. (5.44) is proportional to $\Gamma_z(0)$, as the integral is completely dominated by the low frequency region. In this range, the spectral density $S_\Phi(\omega)$ is constant up to a characteristic frequency $f_\xi = \omega_\xi/2\pi$, as represented in Fig. 5.4. The relation between the spin-flip rate $\Gamma_z(\omega)$ and $S_\Phi(\omega)$ shown in Eq. (5.34), leads to $\Gamma_z(\omega)\approx\Gamma_z(0)$ for frequencies $\omega<\omega_\xi$. Above ω_ξ, $\Gamma_z(\omega)$ decays roughly as $1/\omega$, such that the largest contribution to the integral in Eq. (5.44) is given by frequencies in the range $0\le\omega\le 2\pi/T$. The approximation $\Gamma_z(\omega)\simeq\Gamma(0)$ holds as long as the observation time T satisfies $T>1/f_\xi$. Indeed, as f_ξ exceeds 100 Hz, this is the case for $T>10$ ms.

Supposing once again that the states $|1\rangle$ and $|2\rangle$ are the ground states $|F=2,m_F=2\rangle$ and $|F=2,m_F=1\rangle$ of a rubidium atom, then $(\mu_{22}-\mu_{11})^2=\mu_B^2 3/4$

and a particularly simple result can be obtained as

$$\sigma[\varphi(T)]^2 = \frac{3}{8}\Gamma_z(0)\,T \simeq 10^6\,x(0)\,T. \tag{5.48}$$

Since the value of $x(0)$ reported in [88] is in the range 10^{-9}–10^{-5}, the corresponding dephasing time $\tau_2 \simeq 2/\sigma[\varphi^2]^2$ is in the range 0.2 s – 2000 s. This provides a very convenient time scale for the study of vortex noise using Ramsey interferometry, in which atoms prepared in a coherent superposition of Zeeman sublevels are later interrogated to measure the time-evolution of the coherence. The vortex field noise would be manifested as a loss of Ramsey fringe visibility, which could be studied as a function of the atom-surface distance.

5.3 Summary

To conclude, neutral atoms can act as sensitive probes in the detection of vortex dynamics in thin superconducting films. Magnetic field noise due to the vortex motion can be sampled by observing the spin-flip lifetime. This lifetime can be obtained from existing experimental data and the relation between the spectral density of the magnetic flux noise to the spin-flip rate consists the main result of this Chapter. The relation obtained depends on physical parameter such as the distance from the surface and the SQUID dimensions. Depending on the ratio of those parameters, two different limiting regimes occur and two corresponding power laws are encountered. The two power laws are compared and understood in terms of the electromagnetic field coherence length encountered in Chapter 4 and of its decay over a distance of the order of the skin depth.

For a separation from the surface of 100 μm, the lifetime appears to be longer than 500 s. This is long enough to keep atoms trapped above a superconducting film. Moreover, mapping of vortices could be achieved by means of cold atomic clouds or Bose Einstein condensates, as they are well known to feature simultaneously high spatial resolution and high field sensitivity. Magnetic fields from

vortices alter the trapping potential and this would reflect on the density profile of the atomic cloud, which is measurable with high resolution imaging.

Further information about vortex dynamics can be inferred by studying the dephasing time of a coherent superposition of Zeeman sublevels by Ramsey interferometry. The fringe visibility would be affected with time and the coherence lifetime could be measured. The variance of the phase induced by magnetic field fluctuations can be expressed in terms of the spin-flip rate and estimates of the relaxation time can be obtained by looking at the flux noise spectrum provided by experimental data.

The result obtained is also interesting for cold atoms trapped in atom chips using dielectric or conducting substrates. In quantum information processing, long coherence lifetimes are of fundamental importance to realize a phase gate and the interaction of neutral atoms with the chip surface results in a reduction of this lifetime. The ability to describe the loss of coherence in terms of the distance from the surface and other experimental length scale is then extremely important.

Conclusions and Outlooks

It was the intention of this thesis to investigate relaxation phenomena due to the interaction of an atom with different substrates. A magnetically trapped neutral atom is subjected to near-field magnetic noise when it is held close to a dielectric or metallic surface. The origin of the magnetic noise lies in thermally induced currents originating in the substrate which result in magnetic-field fluctuations near the surface. These fluctuations can be strong enough to drive spin transitions to non-trapped states of the atom. This problem is relevant to proposals and experiments concerned with achieving both long trapping lifetimes and robust manipulation of neutral atoms.

The work presented in this thesis aims at giving a better understanding of decoherence processes induced by near-field magnetic noise and at suggesting novel ways or realising atomic microchip traps. The latter has been addressed in Chapter 3 by considering an atom trapped near a carbon nanotube. In Chapter 4, spatial decoherence has been investigated for an atom in a superposition of two distinct positions. Previous theoretical and experimental studies have shown the dependence of the spin-flip lifetime on the skin depth of the materials adopted showing that superconductors are expected to boost this lifetime by several orders of magnitude. Although thermal noise is in principle absent in superconductors, in the superconducting thin films adopted in atom chips the dominant noise source will be vortex motion and this issue is addressed in Chapter 5. In the following a summary of the results obtained is given.

Chapter 3

The realization of a wire-based atom chip where a carbon nanotube is used instead of a macroscopic current-carrying wire has been the focus of Chapter 3. Carbon nanotubes have two main advantages. First, their small dimensions would ideally permit the next step towards miniaturization of atomic traps. This appear to be relevant in order to obtain strong trapping potentials and also to realize integrable microstructured devices. Secondly, the carbon nanotube is a graphene sheet rolled up into a cylinder which menas that it consists of a reduced amount of matter and for this reason is less likely to induce inhomogeneities in the trapping potential.

The calculation of the spin-flip lifetime has been presented for a conducting carbon nanotube of radius R_{CN}. This lifetime increases with the atom-surface distance and values of a few seconds are achievable for distances of the order of $\simeq 5R_{CN}$. The estimation of the spin-flip lifetime is very promising, but the close proximity of the atom to the carbon nanotube surface has suggested that the attractive Casimir-Polder potential may modify significantly the trapping potential. The Casimir-Polder potential has been added to the (repulsive) trapping potential revealing that an atom can tunnel through the potential barrier and get stuck at the nanotube surface. In particular, the height and width of the potential barrier vary with the trapping distance and below certain distances the barrier disappears. Only for trapping distances that are several multiples of R_{CN}, the total potential shows a pronounced minimum where the atom can be placed. The tunnelling lifetime through such a potential barrier has been evaluated by adopting the WKB approximation and the results for a ground-state atoms show that the Casimir-Polder potential imposes more severe limitations on the minimum trapping distance.

Finally, the fact that an atom trapped in such a potential occupies resonant states and has no true bound states has been discussed. This lead to addressing the possibility of having bound states for distances below the trapping ones such that the atom would be trapped between the carbon nanotube surface, considered

as a delta potential, and the Casimir-Polder potential. In order to estimate the energy of the first bound state, it has been necessary to approximate the Casimir-Polder potential as a power law of the distance from the surface and numerical interpolations has shown a $1/r^3$ dependence. According to the description adopted here, the wavelength associated to such a state would bee too big and this suggests that no bound state exists.

Chapter 4

In Chapter 4 the loss of spatial coherence due to thermally-induced spin-flip transitions has been investigated. The evolution of a macroscopic quantum coherence state has been studied by considering an atom in a double-well potential above a dielectric surface. The atom, in a superposition of the two sites, experiences a loss of its spatial coherence due to thermally-induced spin-flip transitions. Magnetic field fluctuations act incoherently at the two atomic positions and this represents a concern in experiments requiring high degree of coherence.

The spatial coherence of the atomic system has been described by the off-diagonal elements of the atomic density matrix from which a decoherence rate has been extracted. Calculations have been carried out for a planar substrate and the corresponding Green tensor has been expressed in terms of the Weyl expansion. The spatial decoherence rate obtained decreases with the distance from the surface and with the lateral separation of the atom's positions. The decay of the spatial coherence starts off rather slowly as spin-flip transitions are induced coherently at both sides for lateral separations below the coherence length of the electromagnetic field. For the spin-flip transition considered in this thesis, it has been observed that the transition wavelength is the biggest length scale in the system. This approximation allows the Green tensor to be written in a simplified form such that an analytical expression of the spatial decoherence rate is obtained for small lateral separations. In this limit, the decoherence rate has been written as an explicit function of the atom-surface distance and the separation between the sites

of the double-well. The expression obtained in terms of experimental parameters may prove very useful in tailoring microstrucured devices in order to maintain the decoherence rate within a tolerance range.

A numerical study of the decoherence rate for a three layer system has been presented for larger separations. In particular, the lateral separation at which the spatial coherence drops to half of its initial value has been plotted as a function of the layer thickness and for different skin depths of the substrate. This separation has been regarded as a measure of robustness against decoherence and it reveals that the robustness of the spatial coherence drops dramatically for thicknesses of the order of the skin depth. An intuitive explanation of the behaviour encountered for different skin depths has been attempted at the end of Chapter 4 by considering the skin depth as a layer of radiating dipoles.

Chapter 5

Understanding the origin of microscopic vortex noise was beyond the scope of this thesis and the focus of Chapter 5 has then become to address the possibility of probing vortex dynamics with cold neutral atoms. This has been done by estimating the spin-flip lifetime and the dephasing time. The estimates have been guided by existing experimental data on the spectral density of the magnetic flux noise. In the experiment considered, magnetic flux variations due to vortex dynamics were measured by monitoring a Josephson junction with a superconducting quantum interference device (SQUID).

A relation between the noise spectrum and the spin-flip rate has been derived and it depends on physical parameters such as the distance from the surface and the SQUID dimensions. Two different limiting situations have been considered depending on the ratio between those parameter and the case of a large SQUID close to the surface has been studied in more detail. In this case the assumption introduced in Chapter 4 about the spin-flip transition wavelength being the biggest length scale of the system can be safely applied.

A rather long spin-flip lifetime has been obtained which suggests that atoms can be held and manipulated above a superconducting thin film. Nevertheless, this lifetime is short enough to be observed and the imaging of vortices could be in principle possible by studying the density distribution of an atomic cloud. Additional information on vortex dynamics are provided by the phase noise induced between two Zeeman sublevels. A superposition of those levels has been considered and the variance of the phase induced by magnetic field fluctuations has been calculated, which is proportional to the magnetic field correlation function. The variance can then be expressed in terms of the spin-flip rate and estimates of the relaxation time has been, again, guided by experimental data. The dephasing time obtained appears to be long enough to perform Ramsey interferometry and so to obtain information about phase coherence by looking at the interference pattern.

Outlook

In Chapter 3 there are two open questions. First of all, the power law of the atom-surface distance encountered for the Casimir-Polder potential needs to be investigated in more detail. The power law obtained here (for very short distances from the carbon nanotube surface) is typical of the interaction of an atom with a half space while in this situation one would expect the power law associated to the interaction of an atom with a thin wall. This leads to a second wider issue regarding the validity of the electrodynamic in dielectric media in the close proximity of a substrate where the atomic structure can be resolved.

The study presented in Chapter 4 needs to consider additional decoherence mechanism to be complete, such as thermally-induced Raman transitions between two hyperfine states. The same theoretical framework presented in Chapter 4 can be used once a proper interaction Hamiltonian has been derived. A suitable formulation of the coupling between the atomic system and the fluctuating electromagnetic field will distinguish between the on-resonant and the off-resonant interaction. A decoherence rate can be derived by looking at the off-diagonal el-

ement of the atomic density matrix. This study, together with the results about spatial decoherence, will prove useful in the understanding of amplitude and phase fluctuations occurring in typical experimental realizations.

Regarding the detection of vortices addressed in Chapter 5, a step further would be to describe the magnetic flux of a single vortex as if radiating from an individual magnetic dipole. This would allow a first principle derivation of the spectral density of the magnetic flux noise and a better understanding of the power laws obtained when considering a large SQUID placed very close to the surface or the opposite limiting situation. An additional prospect would be to estimate the resolution provided by an atomic cloud compared with superconducting interference devices. Cold atomic clouds have the potential to provide high resolution and high sensitivity when a magnetic field is applied and they could provide a deeper understanding of the vortex dynamics.

A

Axial conductivity and dielectric permittivity of a carbon nanotube

In this appendix, the frequency dependence of the axial surface conductivity $\sigma(\omega)$ and of the dielectric permittivity $\epsilon(\omega)$ for a single-wall carbon nanotube (CN) are briefly reviewed following the work presented in [130, 132].

A single-wall carbon nanotube can be though of as a layer of graphene rolled up into a cylinder. The carbon nanotube energy bands derive from the π orbits (π bands) and σ orbits (σ bands) of the graphene sheet. Due to the cylindrical symmetry of the system, the electron wave number perpendicular to the CN axis, $p_\perp$, is quantised and needs to satisfy the boundary condition $2\pi R_{CN} p_\perp = 2\pi j$, wehre R_{CN} is the nanotube radius and j is an integer. A graphene sheet consists of an hexagonal lattice structure with a carbon atom sitting at each vertex and the structure of a carbon nanotube can be specified by a lattice vector between two hexagons defined as $\mathbf{R}_{a,b} = a\mathbf{x} + b\mathbf{y}$ where a and b are integer numbers and $\mathbf{x}$ and $\mathbf{y}$ are the unit vectors of the two-dimensional graphene lattice as shown in Fig. 3.2.

The conduction properties of a carbon nanotube depend on the way it is rolled and this reflects on the relation between a and b. In the following the tubule index (a,b) is adopted and a nanotube (a,b) is said to be conducting when $2a + b = 3n$

with n an integer. A carbon nanotube (a, b) has a one-dimensional energy bands

$$E_{\pm}(N,p) = \pm t_0 \sqrt{1 + 4\cos\left(\frac{2\pi N}{a} - \frac{a+2b}{2a}p\ell\right)\cos\frac{p\ell}{2} + 4\cos^2\frac{p\ell}{2}} \qquad \text{(A.1)}$$

where $\ell = 2.13$ Å is $\frac{3}{2}$ times the interatomic distance, $t_0 = 4.32 \times 10^{-19}$ J is the tunnelling energy of the electrons along the lattice sites [130], $N = 0, 1, \ldots, a-1$, and $\pi/\ell \leq p \leq \pi/\ell$ with p the electronic wave number. The corresponding Fermi distribution function is $f(E) = 1/\{\exp[\beta(E-\mu)]+1\}$ with inverse temperature β and chemical potential μ.

The dielectric permittivity of a conducting carbon nanotube is well described by the Drude relation

$$\epsilon_r^d(\omega) = -\frac{(\hbar\omega_{pl})^2}{\hbar\omega(\hbar\omega + i\hbar/\tau_r)}, \qquad \text{(A.2)}$$

with ω_{pl} the plasma frequency

$$\begin{aligned}\omega_{pl}^2 &= -\left(\frac{e\hbar}{m}\right)^2 \frac{2\rho_C}{a\ell} \sum_N \int_{-\pi/\ell}^{\pi/\ell} dp\, [\mathrm{Im}K_0(N,p)]^2 \\ &\quad \times \{f'(E_+(N,p)) + f'(E_-(N,p))\}, \qquad \text{(A.3)}\end{aligned}$$

where $\rho_C = 2a\rho_T = (\pi\sqrt{3})/(2R_{\mathrm{CN}}\ell^2)$ is the density of carbon atoms per volume [133] and ρ_T is the volume density. The quantity $K_0(N,p)$ corresponds to the (dimensionless) matrix element of the momentum operator and is expressed as

$$K_0(N,k) = e^{-i\theta(N,k)} \sum_{\lambda=1}^{3} e^{-i\phi_\lambda}(N,k)[J_1\cos\eta_\lambda + J_2(1-\cos\eta_\lambda))^2]\xi_\lambda, \qquad \text{(A.4)}$$

where the subscripts λ =1, 2 and 3 correspond to three different nearest neighbour pairs and θ is the argument of

$$\left\{\exp\left[-i\left(\frac{2\pi N}{a} - \frac{b}{a}kl\right)\right] + \exp(-ikl) + 1\right\}.$$

For the sake of simplicity, the tables of the auxiliary variables $\phi_\lambda(N,k)$, η_λ and ξ_λ,

and of the matrix elements of the momentum operator J_1 and J_2 are not reported here and can be found in [130].

For high frequency regimes transitions between conduction and valence bands become important and an additional term ϵ_r^b needs to be considered in the total dielectric permittivity

$$\epsilon_r(\omega) = \epsilon_r^d(\omega) + \epsilon_r^b(\omega)\,, \tag{A.5}$$

with the interband transition term given by

$$\begin{aligned}\epsilon_r^b(\omega) = 1 + \left(\frac{e\hbar^2}{m}\right)^2 \frac{4\rho_C}{a\ell} \sum_N \\ \times \int_{-\pi/l}^{\pi/l} dp \, \frac{f(E_+(N,p)) - f(E_-(N,p))}{E_+(N,p) - E_-(N,p)} \\ \times \frac{[\mathrm{Re}K_0(N,p)]^2}{(\hbar\omega)^2 + i\hbar^2\omega/\tau_r - [E_+(N,p) - E_-(N,p)]^2},\end{aligned} \tag{A.6}$$

where τ_r is a phenomenological relaxation time such that $\hbar/\tau_r = 4.8\times10^{-21}$ J [130].

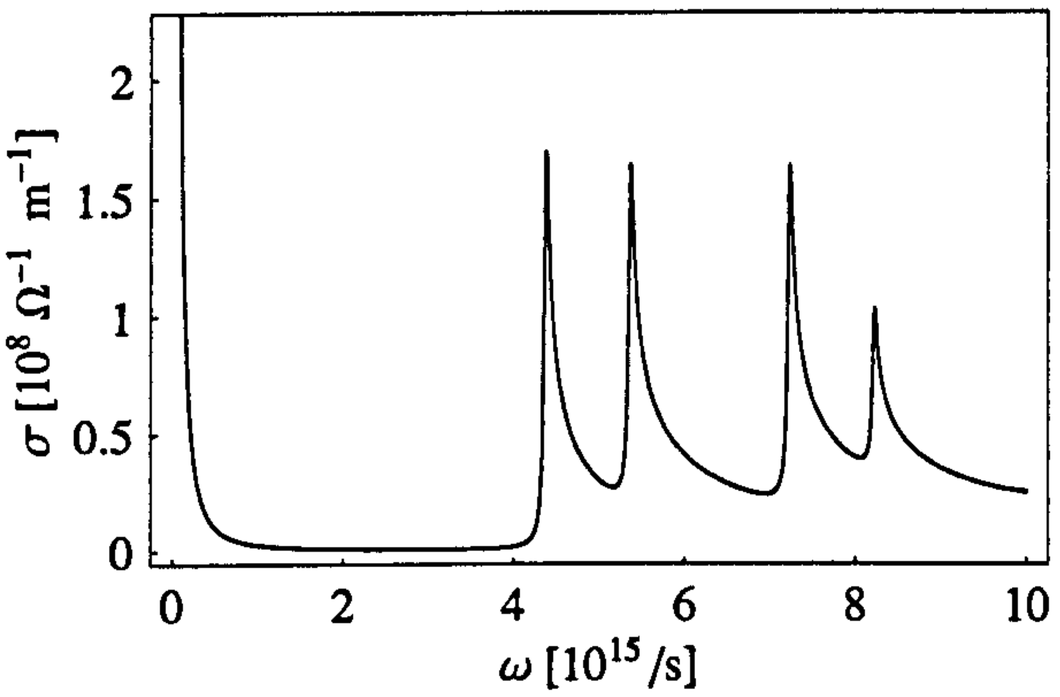

Figure A.1: Real part of the axial conductivity as a function of the frequency for a (9,0) carbon nanotube with radius $R_{CN} = 3.52$ Å.

The axial conductivity for a single wall nanotube can then be expressed as

$$\sigma_{zz}(\mathbf{R},\omega) \;=\; -\frac{i\omega\epsilon_0}{S}\frac{\epsilon_r(\mathbf{R},\omega) - 1}{\rho_T}, \tag{A.7}$$

and the frequency dependence of the real part of the parallel conductivity for a

metallic nanotube (9,0) is shown in Fig. A.1. The growth of the conductivity at low frequency is due to the Drude term of Eq. (A.2). The peaks appearing for larger frequencies correspond to interband transitions. In particular, the parallel dielectric function, and as a consequence the axial conductivity, exhibits a plasmon peak at about $\omega = 2t_0/\hbar \simeq 1.310^{15}$ Hz which is due to the π electrons.

B

Green tensor of planar multilayers

Here, the calculation of the Green function for planar multilayers is reviewed following [74, 157]. The notation adopted for planar layers is slightly different from the one used for carbon nanotubes in Section 3.1.1 and the reason is merely related to a question of simplicity in choosing the labels. The dyadic Green function for the electromagnetic field scattering from a material interface can always be decomposed into

$$\boldsymbol{G}(\mathbf{r},\mathbf{r}',\omega) = \begin{cases} \boldsymbol{G}^{(1)}(\mathbf{r},\mathbf{r}',\omega) + \boldsymbol{R}^{(12)}(\mathbf{r},\mathbf{r}',\omega)\,, & \mathbf{r},\mathbf{r}' \in \mathcal{V}_1 \\ \boldsymbol{T}^{(12)}(\mathbf{r},\mathbf{r}',\omega)\,, & \mathbf{r} \in \mathcal{V}_1\,, \mathbf{r}' \in \mathcal{V}_2 \end{cases} \tag{B.1}$$

where $\boldsymbol{G}^{(1)}(\mathbf{r},\mathbf{r}',\omega)$ denotes the solution to the inhomogeneous Helmholtz equation with the source in region $\mathcal{V}_1$, which in the present case is the vacuum with $\varepsilon_1(\omega) \equiv 1$. The two scattering terms $\boldsymbol{R}^{(12)}(\mathbf{r},\mathbf{r}',\omega)$ and $\boldsymbol{T}^{(12)}(\mathbf{r},\mathbf{r}',\omega)$ have to be introduced to satisfy the boundary conditions for the electromagnetic field at the interface and they represent the reflection and transmission parts of the total scattering Green function, respectively.

For an atom located in the vacuum above the substrate material, only the reflection part $\boldsymbol{R}^{(12)}(\mathbf{r},\mathbf{r}',\omega)$ needs to be considered as the contribution to the spin flip rate and spatial decoherence given by the vacuum part $\boldsymbol{G}^{(1)}(\mathbf{r},\mathbf{r}',\omega)$ can

be neglected. The translational invariance in two spatial directions, say in the (x, y)-plane, allows one to write the Green function in terms of its Weyl expansion

$$\boldsymbol{R}^{(12)}(\mathbf{r}, \mathbf{r}', \omega) = \int \frac{d^2 k_\parallel}{(2\pi)^2} \boldsymbol{R}^{(12)}(\mathbf{k}_\parallel, \omega; z, z') e^{i\mathbf{k}_\parallel \cdot (\boldsymbol{\rho} - \boldsymbol{\rho}')} \tag{B.2}$$

where $\boldsymbol{\rho} = (x, y)$ and $\mathbf{k}_\parallel = (k_x, k_y)$ are the position vector and the wave-vector, respectively, in the (x, y)-plane. The matrix components of $\boldsymbol{R}^{(12)}(\mathbf{k}_\parallel, \omega; z, z')$ can be read off from [74] as (here the arguments are omitted to enhance readability)

$$\begin{aligned}
R_{xx}^{(12)} &= \frac{i}{2k_{1z}} e^{ik_{1z}(z+z')} \left[-r_{12}^{TM} \frac{k_{1z}^2 k_x^2}{k_1^2 k_\parallel^2} + r_{12}^{TE} \frac{k_y^2}{k_\parallel^2} \right], \\
R_{xy}^{(12)} &= \frac{i}{2k_{1z}} e^{ik_{1z}(z+z')} \left[-r_{12}^{TM} \frac{k_{1z}^2 k_x k_y}{k_1^2 k_\parallel^2} - r_{12}^{TE} \frac{k_x k_y}{k_\parallel^2} \right], \\
R_{xz}^{(12)} &= \frac{i}{2k_{1z}} e^{ik_{1z}(z+z')} \left[r_{12}^{TM} \frac{k_{1z} k_x}{k_1^2} \right], \\
R_{zz}^{(12)} &= \frac{i}{2k_{1z}} e^{ik_{1z}(z+z')} \left[r_{12}^{TM} \frac{k_\parallel^2}{k_1^2} \right], \\
R_{zx}^{(12)} &= R_{xz}^{(12)}, \\
R_{zx}^{(12)} &= -R_{xz}^{(12)}, \quad R_{zy}^{(12)} = -R_{yz}^{(12)}, \\
R_{yy}^{(12)} &= R_{xx}^{(12)}(k_x \leftrightarrow k_y), \quad R_{yz}^{(12)} = R_{xz}^{(12)}(k_x \leftrightarrow k_y),
\end{aligned} \tag{B.3}$$

where $k_i^2 = \frac{\omega^2}{c^2} \varepsilon_i(\omega)$ and $k_{iz}^2 = k_i^2 - k_\parallel^2$.

The functions r_{12}^{TE} and r_{12}^{TM} denote the Fresnel reflection coefficients for TE and TM waves, respectively, and are defined by

$$r_{12}^{TE} = \frac{k_{1z} - k_{2z}}{k_{1z} + k_{2z}}, \quad r_{12}^{TM} = \frac{\varepsilon_2(\omega) k_{1z} - \varepsilon_1(\omega) k_{2z}}{\varepsilon_2(\omega) k_{1z} + \varepsilon_1(\omega) k_{2z}}. \tag{B.4}$$

The Fresnel coefficients obey certain recursion relations that permit one to calculate the dyadic Green function for arbitrarily multi-layered materials [140,157,176]. In particular, the generalized Fresnel coefficient for a three-layer geometry reads

(for both TE and TM polarizations)

$$\tilde{r}_{12} = \frac{r_{12} + r_{23}e^{2ik_{2z}h}}{1 - r_{21}r_{23}e^{2ik_{2z}h}} \tag{B.5}$$

where h is the thickness of the intermediate layer indicated by the label 2.

Bibliography

[1] T. L. Gustavson, P. Bouyer, and M. A. Kasevich, Phys. Rev. Lett. **78**, 2046 (1997).

[2] G. Ferrari, N. Poli, F. Sorrentino, and G. M. Tino, Phys. Rev. Lett. **97**, 060402 (2006).

[3] I. K. Kominis, T. W. Kornack, J. C. Allred, and M. V. Romalis, Nature (London) **422**, 596 (2003).

[4] S. Wildermuth, S. Hofferberth, I. Lesanovsky, E. Haller, L. M. Andersson, S. Groth, I. Bar-Joseph, P. Krüger and J. Schmiedmayer, Nature **435**, 440 (2005).

[5] S. Wildermuth, S. Hofferberth, I. Lesanovsky, S. Groth, P. Krüger,J. Schmiedmayer, and I. Bar-Joseph, Appl. Phys. Lett. **88**, 264103 (2006).

[6] B. V. Hall, S. Whitlock, R. Anderson, P. Hannaford, and A. I. Sidorov, Phys. Rev. Lett. **98**, 030402 (2007).

[7] J. Fortágh, H. Ott, S. Kraft, A. Günther, and C. Zimmermann, Phys. Rev. A **66**, 041604 (2002).

[8] M. P. A. Jones, C. J. Vale, D. Sahagun, B. V. Hall, and E. A. Hinds, Phys. Rev. Lett. **91**, 080401 (2003).

[9] D. M. Harber, J. M. McGuirk, J. M. Obrecht, and E. A. Cornell, J. Low Temp. Phys. **133**, 229 (2003).

[10] Y. J. Lin, I. Teper, C. Chin, and V. Vuletić, Phys. Rev. Lett. **92**, 050404 (2004).

[11] D. M. Harber, J. M. Obrecht, J. M. McGuirk, and E. A. Cornell, Phys. Rev. A **72**, 033610 (2005).

[12] P. W. Milonni, *The quantum vacuum: An introduction to quantum electrodynamics* (Academic Press, London, 1994).

[13] H. B. G. Casimir and D. Polder, Phys. Rev. **73**, 360 (1948).

[14] I. E. Dzyaloshinskii, E. M. Lifshitz, L. P. Pitaevskii, Adv. Phys. **10**, 165 (1961).

[15] C. I. Sukenik, M. G. Boshier, D. Cho, V. Sandoghdar, and E. A. Hinds, Phys. Rev. Lett. **70**, 560 (1993).

[16] S. Y. Buhmann, L. Knöll, D.-G. Welsch and H. T. Dung, Phys. Rev. A **70**, 052117 (2004).

[17] S. Y. Buhmann, T. D. Ho, and D.-G. Welsch, J. Opt. B: Quantum Semiclass. Opt. **6**, S127 (2004).

[18] T. A. Pasquini, Y. Shin, C. Sanner, M. Saba, A. Schirotzek, D. E. Pritchard, and W. Ketterle, Phys. Rev. A **93**, 223201 (2004).

[19] T. A. Pasquini, M. Saba, G. Jo, Y. Shin, W. Ketterle, and D. E. Pritchard, Phys. Rev. Lett. **97**, 093201 (2006).

[20] E. Yablonovitch, Phys. Rev. Lett. **58**, 2059 (1987).

[21] S. M. Barnett, B. Huttner, and R. Loudon, Phys. Rev. Lett. **68**, 3698 (1992).

[22] E. A. Hinds, and I. G. Hughes, J. Phys. D.: Appl. Phys. **32**, R119 (1999).

[23] M. Bartenstein, D. Cassettari, T. Calarco, A. Chenet, R. Folman, K. Brugger, A. Haase, E. Hartungen, B. Hessmo, A. Kasper, P. Krüger, T. Maier, F. Payr, S. Schneider, and J. Schmiedmayer, IEEE Journ. Quant. El. **63**, 10 (2000).

[24] R. Folman, P. Krüger, J. Schmiedmayer, J. Denschlag, and C. Henkel, Adv. At. Mol. Opt. Phys. **48**, 263 (2002).

[25] J. Reichel, Appl. Phys. B **75**, 469-487 (2002).

[26] J. Fortágh and C. Zimmermann, Rev. Mod. Phys. **79**, 1 (2007).

[27] J. I. Cirac and P. Zoller, Phys. Rev. Lett. **74**, 4091 (1995).

[28] G. K. Brennen, C. M. Caves, P. S. Jessen, and I. Deutsch, Phys. Rev. Lett. **82**, 1060 (1999).

[29] T. Calarco, E. A. Hinds, D. Jaksch, J. Schmiedmayer, J. I. Cirac, and P. Zoller, Phys. Rev. A **61**, 022304 (2000).

[30] J. Schmiedmayer, R. Folman, and T. Calarco, J. Mod. Opt. **49**, 1375 (2002).

[31] J. K. Pachos and P. L. Knight, Phys. Rev. Lett. **91**, 107902 (2003).

[32] P. Treutlein, P. Hommelhoff, T. Steinmetz, T. W. Hänsch, and J. Reichel, Phys. Rev. A **92**, 203005 (2004).

[33] D. Jaksch, Contemp. Phys. **45**, 367 (2004).

[34] E. Charron, M. A. Cirone, A. Negretti, J. Schmiedmayer, and T. Calarco, Phys. Rev. A **74**, 012308 (2006).

[35] P. Treutlein, T. W. Hänsch, J. Reichel, A. Negretti, M. A. Cirone, and T. Calarco, Phys. Rev. A **74**, 022312 (2006).

[36] R. Zhang, R. E. Sapiro, N. V. Morrow, and G. Raithel, Phys. Rev. A **74**, 033404 (2006).

[37] J. Schmiedmayer, Phys. Rev. A **52**, R13 (1995).

[38] J. D. Weinstein and K. G. Libbrecht, Phys. Rev. A **52**, 4004 (1995).

[39] J. P. Dowling, and J. Gea-Banacloche, Adv. At. Mol. Opt. Phys. **37**, 1 (1996).

[40] V. Vuletic, T. Fischer, M. Praeger, T. W. Hänsch, and C. Zimmermann, Phys. Rev. Lett. **80**, 1634 (1998).

[41] J. Fortágh, A. Grossman, C. Zimmermann, and T. W. Hänsch, Phys. Rev. Lett. **81**, 5310 (1998).

[42] D. Müller, D. Z. Anderson, R. J. Grow, P. D. D. Schwindt, and E. A. Cornell, Phys. Rev. Lett. **83**, 5194 (1999).

[43] M. Key, I. G. Hughes, W. Rooijakkers, B. E. Sauer, E. A. Hinds, D. J. Richardson, and P. G. Kazansky, Phys. Rev. Lett. **84**, 1371 (2000).

[44] N. H. Dekker, C. S. Lee, V. Lorent, J. H. Thywissen, S. P. Smith, M. Drndić, R. M. Westervelt, and M. Prentiss, Phys. Rev. Lett. **84**, 1124 (2000).

[45] C. Henkel, S. Pötting, and M. Wilkens, Appl. Phys. B: Lasers Opt. **69**, 379 (1999).

[46] C. Henkel, and M. Wilkens, Europhys. Lett. **47**, 414 (1999).

[47] C. Henkel, and S. Pötting, Appl. Phys. B **72**, 73 (2001).

[48] C. Henkel, P. Krüger, R. Folman, and J. Schmiedmayer, Appl. Phys. B **76**, 173 (2003).

[49] P. K. Rekdal, S. Scheel, P. L. Knight, and E. A. Hinds, Phys. Rev. A **70**, 013811 (2004).

[50] S. Scheel, P. K. Rekdal, P. L. Knight, and E. A. Hinds, Phys. Rev. A **72**, 042901 (2005).

[51] C. Henkel, Eur. Phys. J. D. **35**, 59 (2005).

[52] V. Dikovsky, Y. Japha, C. Henkel, and R. Folman, Eur. Phys. J. D **35**, 87 (2005).

[53] C. Schroll, W. Belzig, and C. Bruder, Phys. Rev. A **68**, 043618 (2003).

[54] J. A. Dunningham and K. Burnett, and S. M. Barnett, Phys. Rev. Lett. **89**, 150401 (2004).

[55] J. Baudon, R. Mathevet and J. Robert, J. Phys. B: At. Mol. Opt. Phys. **32**, R173 (1999).

[56] M. Kasevich, and S. Chu, Phys. Rev. Lett. **67**, 181 (1991).

[57] E. A. Hinds, C. J. Vale, and M. G. Boshier, Phys. Rev. Lett. **86**, 1462 (2001).

[58] E. Andersson, T. Calarco, R. Folman, M. Andersson, B. Hessmo, and J. Schmiedmayer, Phys. Rev. Lett. **88**, 100401 (2002).

[59] Y. Shin, M. Saba, T. A. Pasquini, W. Ketterle, D. E. Pritchard, and A. E. Leanhardt, Phys. Rev. Lett. **92**, 050405 (2004).

[60] Y.-J. Wang, D. Z. Anderson, V. M. Bright, E. A. Cornell, Q. Diot, T. Kishimoto, M. Prentiss, R. A. Saravanan, S. R. Segal, and S. Wu, Phys. Rev. Lett. **94**, 090405 (2005).

[61] T. Schumm, S. Hofferberth, L. M. Andersson, S. Wildermuth, S. Groth, I. Bar-Joseph, J. Schmiedmayer, and P. Krüger, Nature Phys. **1**, 57 (2005).

[62] A. Günther, S. Kraft, C. Zimmermann, and J. Fortágh, Phys. Rev. Lett. **98**, 140403 (2007).

[63] G.-B. Jo, Y. Shin, S. Will, T. A. Pasquini, M. Saba, W. Ketterle, D. E. Pritchard, M. Vengalattore, and M. Prentiss, Phys. Rev. Lett. **98**, 030407 (2007) .

[64] W. Hänsel, J. Reichel, P. Hommelhoff, and T. W. Hänsch, Phys. Rev. A **64**, 063607 (2001).

[65] J. C. Gallop, *SQUIDS, the Josephson effects and superconducting electronics*, (Adam Hilger, Bristol, 1991)

[66] J. A. Sidles, J. L. Garbini, K. J. Bruland, D. Rugar, O. Züger, S. Hoen, and C. S. Yannoni, Rev. Mod. Phys. **67**, 249 (1995).

[67] G. S. Agarwal, Phys. Rev. A **11**, 230 (1975).

[68] T. Varpula, and T. Poutanen, J. Appl. Phys. **55**, 4015 (1984).

[69] J. M. Wylie, and J. E. Sipe, Phys. Rev. A **30**,1185 (1984).

[70] S. M. Rytov, Y. A. Kravtsov, V. I. Tatarskii, *Elements of Random Fields*, Vol. 3 of Principles of Statistical Radiophysics (Springer, Berlin, 1989).

[71] L. Knöll, and U. Leonhardt, J. Mod. Opt. **39**, 1253 (1992).

[72] T. Gruner and D.-G. Welsch, Phys. Rev. A **51**, 3246 (1995).

[73] T. Gruner and D.-G. Welsch, Phys. Rev. A **53**, 1818 (1996).

[74] H. T. Dung, L. Knöll, and D.-G. Welsch, Phys. Rev. A **57**, 3931 (1998).

[75] S. Scheel, L. Knöll, and D.-G. Welsch, Phys. Rev. A **58**, 700 (1998).

[76] L. Knöll, S. Scheel, and D.-G. Welsch, in *Coherence and Statistics of Photons and Atoms*, edited by J. Peřina (Wiley, New York, 2001).

[77] S. Iijima, Nature **354**, 56 (1994).

[78] M. S. Dresselhaus, G. Dresselhaus, and P. C. Eklund, *Science of Fullerens and Carbon Nanotubes* (Academic, New York, 1996).

[79] H. Dai, Surf. Sci. **500**, 218 (2002).

[80] R. H. Baughman, A. A. Zakhidov, and W. A. de Heer, Science **297**, 787 (2002).

[81] V. Peano, M. Thorwart, A. Kasper, and R. Egger, Appl. Phys. B **81**, 1075 (2005).

[82] B. S. Skagerstam, U. Hohenester, A. Eiguren, and P. K. Rekdal, Phys. Rev. Lett. **97**, 070401 (2006).

[83] U. Hohenester, A. Eiguren, S. Scheel, and E. A. Hinds, Phys. Rev. A **76**, 033618 (2007).

[84] A. A. Abrikosov, Zh. Eksperim. i Teor. Fiz. **32**, 1442 (1957).

[85] V. L. Berezinskii, Zh. Eksp. Teor. Fiz. **59**, 207 (1970).

[86] V. L. Berezinskii, Sov. Phys. JETP **34**, 610 (1971).

[87] J. M. Kosterlitz, and D. J. Thouless, J. Phys. **C6**, 1181 (1973).

[88] T. J. Shaw, M. J. Ferrari, L. L. Sohn, D. H. Lee, M. Tinkham, and J. Clarke, Phys. Rev. Lett. **76**, 2551 (1996).

[89] A. L. Migdall, J. V. Prodan, W. D. Phillips, T. H. Bergeman, and H. J. Metcalf, Phys. Rev. Lett. **54**, 2596 (1985).

[90] H. F. Hess, G. P. Kochanski, J. M. Doyle, N. Masuhara, D. Kleppner, and T. J. Greytak, Phys. Rev. Lett. **59**, 672 (1987).

[91] T. W. Hijmans, O. J. Luiten, I. D. Setija, and J. T. M. Walraven, J. Opt. Soc. Am. B **6**, 2235 (1989).

[92] N. J. van Druten, and W. Ketterle, Phys. Rev. Lett. **79**, 549(1997).

[93] M. Olshanii, Phys. Rev. Lett. **81**, 938 (1998).

[94] W. H. Wing, Prog. Quantum Electrom. **8**, 181-199 (1984).

[95] W. Ketterle and D. E. Pritchard, Appl. Phys. B **54**, 403-406 (1992).

[96] E. Majorana, Nuovo Cimento **9**, 43 (1932).

[97] C. V. Sukumar, and D. M. Brink, Phys. Rev. A **56**, 2451 (1997).

[98] S. Gov, S. Shtrikman, and H. Thomas, J. Appl. Phys. **87**, 3989 (2000).

[99] R. Frisch and E. Segré, Z. Phys. **75**, 610 (1933).

[100] M. E. Gehm, K. M. O'Hara, T. A. Savard, and J. E. Thomas, Phys. Rev. A **58**, 3914 (1998).

[101] J. Weiner, V. S. Bagnato, S. Zilio, and P. S. Julienne, Rev. Mod. Phys. **71**, 1 (1999).

[102] S. Bali, K. M. OHara, M. E. Gehm, S. R. Granade, and J. E. Thomas, Phys. Rev. A **60**, R29 (1999).

[103] J. P. Burke, J. L. Bohn, B. D. Esry, and C. H. Greene, Phys. Rev. A **55**, R2511 (1997).

[104] P. S. Julienne, F. H. Mies, E. Tiesinga, and C. J. Williams, Phys. Rev. Lett. **78**, 1880 (1997).

[105] J. Söding, D. Guéry-Odelin, P. Desbiolles, G. Ferrari, and J. Dalibard, Phys. Rev. Lett. **80**, 1869 (1998).

[106] J. M. Gerton, C. A. Sackett, B. J. Frew, and R. G. Hulet, Phys. Rev. A **59**, 1514 (1999).

[107] O. J. Luiten, M.W. Reynolds, and J. T. M. Walraven, Phys. Rev. A **53**, 381 (1996).

[108] J. Schmiedmayer, Eur. Phys. J. B **4**, 57 (1998).

[109] A. Stern, Y. Aharonov, and Y. Imry, Phys. Rev. A **41**, 3436 (1990).

[110] J. M. Jauch and K. M. Watson, Phys. Rev. **74**, 950 (1948).

[111] P. D. Drummond, Phys. Rev. A **42**, 6845 (1990).

[112] R. J. Glauber and M. Lewenstein, Phys. Rev. A **43**, 467 (1991).

[113] H. M. Nussenzveig, *Causality and Dispersion Relations* (Academic Press, New York, 1972).

[114] D. C. Hutchings, M. Sheik-Bahae, D. J. Hagan, and E. W. Van Stryland, Opt. Quantum Electron. **24**, 1 (1992).

[115] B. Huttner, and S. M. Barnett, Phys. Rev. A **46**, 4306 (1992).

[116] R. Matloob, R. Loudon, S. M. Barnett, and J. Jeffers, Phys. Rev. A **52**, 4823 (1995).

[117] R. Matloob, R. Loudon, S. M. Barnett, and J. Jeffers, Phys. Rev. A **53**, 4567 (1996).

[118] A. Tip, Phys. Rev. A **56**, 5022 (1997).

[119] A. Bechler, J. Mod. Opt. **46**, 901 (1999).

[120] R. Matloob, Phys. Rev. A **60**, 50 (1999).

[121] A. Di Stefano, S. Savasta, and R. Girlanda, Phys. Rev. A **60**, 1614 (1999).

[122] A. Di Stefano, S. Savasta, and R. Girlanda, Phys. Rev. A **61**, 023803 (2000).

[123] J. J. Hopfield, Phys. Rev. **112**, 1555 (1958).

[124] U. Fano, Phys. Rev. **103**, 1202 (1956).

[125] U. Fano, Phys. Rev. **124**, 1866 (1961).

[126] A. A. Abrikosov, L. P. Gorkov, and I. E. Dzyaloshinski, *Methods of Quantum Field Theory in Statistical Physics*, (Dover, New York, 1975).

[127] J. D. Jackson, *Classical Electrodynamics*, 3rd ed. (Wiley, New York,1999).

[128] L. D. Landau and E. M. Lifshitz, *Electrodynamics of Continuous Media* (2nd Edition), (Pergamon, Oxford, 2000).

[129] I. V. Bondarev and Ph. Lambin, Phys. Rev. B **70**, 035407 (2004).

[130] S. Tasaki, K. Maekawa, and T. Yamabe, Phys. Rev. B **57**, 9301 (1998).

[131] N. Hamada, S. I. Sawada, and A. Oshiyama, Phys. Rev. Lett. **68**, 1579 (1992).

[132] M.F. Lin and K.W.K. Shung, Phys. Rev. B **50**, 17744 (1994).

[133] H. Jiang, G. Wu, X. Yang, and J. Dong, Phys. Rev. B **70**, 125404 (2004).

[134] G. Y. Slepyan, S. A. Maksimenko, A. Lakhtakia, O. M. Yevtushenko, and A. V. Gusakov, Phys. Rev. B **57**, 9485 (1999).

[135] G. Y. Slepyan, S. A. Maksimenko, A. Lakhtakia, O. M. Yevtushenko, and A. V. Gusakov, Phys. Rev. B **60**, 17136 (1999).

[136] L. X. Benedict, S. G. Louie and M. L. Cohen, Phys. Rev. B **52**, 8541 (1995).

[137] Z. M. Li, Z. K. Tang, H. J. Liu, N. Wang, C. T. Chan, R. Saito, S. Okada, G. D. Li, J. S. Chen, N. Nagasawa, and S. Tsuda, Phys. Rev. Lett. **87**, 127401 (2001).

[138] A. Jorio, A. G. Souza Filho, V. W. Brar, A. K. Swan, M. S. Ünlü, B. B. Goldberg, A. Righi, J. H. Hafner, C. M. Lieber, R. Saito, G. Dresselhaus, and M. S. Dresselhaus, Phys. Rev. B, **65**, 121402(R) (2002).

[139] A. G. Marinopoulos, L. Reining, A. Rubio, and N. Vast, Phys. Rev. Lett. **91**, 046402 (2003).

[140] W. C. Chew, *Waves and Fields in inhomogeneous media* (IEEE Press, New York, 1995).

[141] L.-W. Li, M.-S. Leong, T.-S. Yeo, and P.-S. Kooi, J. Electromagn. Waves Appl. **14**, 961 (2000).

[142] Z. Yao, C.L. Kane, and C. Dekker, Phys. Rev. Lett. **84**, 2941 (2000).

[143] M. P. Gorza and M. Ducloy, Eur. Phys. J D **40**, 343 (2006).

[144] E. A. Hinds, and C. Eberlein, Phys. Rev. A **61**, 033614 (2000).

[145] J. Bill, M.-I. Trappe, I. Lesanovsky, and P. Schmelcher, Phys. Rev. A **73**, 053609 (2006).

[146] E. V. Blagov, G. L. Klimchitskaya, and V. M. Mostepanenko, Phys. Rev. B **71**, 235401 (2005).

[147] J. Denschlag, G. Umshaus, and J. Schmiedmayer, Phys. Rev. Lett. **81**, 737 (1998).

[148] L. D. Landau and E. M. Lifshitz, *Quantum Mechanics, Course of theoretical physics; 3rd edition* (Pergamon Press, Oxford, 1985).

[149] I. Deutsch, and P. S. Jessen, Phys. Rev. A **57**, 1972 (1998).

[150] D. L. Haycock, P. M. Alsing, I. H. Deutsch, J. Grondalski, and P. S. Jessen, Phys. Rev. Lett. **85**, 3365 (2000).

[151] C. Henkel, M. Nest, P. Domokos, and R. Folman, Phys. Rev. A **70**, 023810 (2004).

[152] O. Mandel, M. Greiner, A. Widera, T. Rom, T.W. Hänsch, and I. Bloch, Nature (London) **425**, 937 (2003).

[153] D. Jaksch, C. Bruder, J. I. Cirac, C. W. Gardiner, and P. Zoller, Phys. Rev. Lett. **81**, 3108 (1999).

[154] S. Scheel, J. K. Pachos, E. A. Hinds, P. L. Knight, In: W. Pötz, J. Fabian and U. Hohenester, Editors, *Quantum Coherence: From Quarks to Solids*, Lecture Notes in Physics **689**, p. 47-80, (Springer, Berlin, 2006).

[155] S. M. Barnett and P. M. Radmore, *Methods in Theoretical Quantum Optics*, (Oxford Science Publications, 1997).

[156] H. T. Dung, L. Knöll, and D.-G. Welsch, Phys. Rev. A **62**, 053804 (2000).

[157] M. S. Tomaš, Phys. Rev. A **51**, 2545 (2000).

[158] S. Casalbuoni, E. A. Knabbe, J. Kötzler, L. Lilje, L. von Sawilski, P. Schmüser, and B. Steffen, Nucl. Instrum. Methods A **538**, 45 (2005).

[159] Ö. Çakir, H. T. Dung, L. Knöll, and D.-G. Welsh, Phys. Rev. A **71**. 032326 (2005).

[160] H. T. Dung, L. Knöll, and D.-G. Welsch, Phys. Rev. A **66**, 063810 (2002).

[161] T. Nirrengarten, A. Qarry, C. Roux, A. Emmert, G. Nogues, M. Brune, J.-M. Raimond, and S. Haroche, Phys. Rev. Lett. **97**, 200405 (2006).

[162] T. Mukai, C. Hufnagel, A. Kasper, T. Meno, A. Tsukada, K. Semba, and F. Shimizu, Phys. Rev. Lett. **98**, 260407 (2007).

[163] A. C. Rose-Innes and F. H. Rhoderidick, *Introduction to Superconductivity* 2nd ed., (Pergamon, Oxford, 1978).

[164] M. Tinkham, *Introduction to Superconductivity* 2nd ed. (MacGraw-Hill, Inc., New York, 1996).

[165] C. P. Poole Jr., H. A. Farach, and R. J. Creswick, *Superconductivity*, (Academic Press, London, 1995).

[166] J. F. Annett, *Superconductivity, Superfluids, and Condensates (Oxford Master Series in Condensed Matter Physics)* (Oxford University Press, New York, 2004).

[167] G. M. Eliashberg, Soviet. Phys. JETP **11**, 696 (1960).

[168] N. D. Mermin, H. Wagner, Phys. Rev. Lett. **17**, 1133 (1966)

[169] P. C. Hohenberg, Phys. Rev. **158**, 383 (1967).

[170] M. R. Beasley, J. E. Mooij, and T. P. Orlando, Phys. Rev. Lett. **42**, 1165 (1979).

[171] D. J. Bishop, and J. D. Reppy, Phys. Rev. Lett. **40**, 1727 (1978).

[172] D. J. Resnick, J. C. Garland, J. T. Boyd, S. Shoemaker, and R. S. Newrock, Phys. Rev. Lett. **47**, 1542 (1981).

[173] Z. Hadzibabic, P. Krüger, M. Cheneau, B. Battelier, and J. Dalibard, Nature **441**, 1118 (2006).

[174] I. S. Gradsteyn and I. M. Ryshik, *Tables of Integrals, Series, and Products* (Academic Press, New York, 1965).

[175] R. Loudon, *The Quantum Theory of Light*, Oxford Science Publications (2000).

[176] L. W. Li, P. S. Kooi, M. S. Leong, and T. S. Yeo, J. Electromagn. Waves Appl. **8**, 663 (1994).